A Supersonic Jet Spectrometer
for Terahertz Applications
(SuJeSTA)

Inaugural-Dissertation
zur
Erlangung des Doktorgrades
der Mathematisch-Naturwissenschaftlichen Fakultät
der Universität zu Köln

vorgelegt von

Michael Caris

aus Köln

Köln 2005

Cover illustration: Discharge of acetylene diluted in helium
employing a pinhole nozzle

There is a theory which states
that if ever anybody discovers exactly
what the Universe is for and why it is here,
it will instantly disappear
and be replaced by something
even more bizarre and inexplicable.
There is another theory which states
that this has already happened.

Douglas Adams (11.03.1952 - 11.05.2001)

Abstract

The purpose of this work is to perform high resolution spectroscopic measurements in the terahertz region aiming at molecular parameters, derived from quantum mechanical analysis of the spectra. These parameters are the basic requirement for accurate frequency predictions and for the astronomical detections of undiscovered species. Two different spectrometers have been used for the spectral analysis in this work:

- The newly designed Supersonic Jet Spectrometer for Terahertz Applications (SuJeSTA) for the investigation of cold radicals and ions

- The Cologne Terahertz Spectrometer

The pure rotational spectra of five isotopomers of potassium chloride, i.e. $^{39}K^{35}Cl$, $^{39}K^{37}Cl$, $^{41}K^{35}Cl$, $^{41}K^{37}Cl$, and $^{40}K^{35}Cl$ have been recorded with the well established Cologne Terahertz Spectrometer (see e.g. [1], [2]). A special evaporation cell has been used to evaporate solid KCl. Within the scope of this thesis, a total of 295 new rotational lines have been measured in the frequency region between 170 and 930 GHz. For the isotopomers $^{39}K^{35}Cl$ and $^{39}K^{37}Cl$ 107 and 82, respectively, rotational transitions have been assigned to transitions belonging to vibrational levels up to the seventh excited state ($v \leq 7$) and to rotational quantum numbers as high as 127 and 129, respectively. 104 lines were measured for the less abundant isotopomers of $^{41}K^{35}Cl$ and $^{41}K^{37}Cl$ with $J \leq 128$, $v \leq 6$ and $J \leq 131$, $v \leq 5$, respectively. Two lines have been assigned to $^{40}K^{35}Cl$, which has a natural abundance of 0.01% relative to $^{39}K^{35}Cl$. The measured lines have been fitted together with previously published millimeter wave transitions to obtain an improved set of molecular parameters for these isotopomers [3]. Besides this analysis, the isotopically invariant Dunham parameters U_{ij} and the Born-Oppenheimer corrections Δ_{01} have been determined. The refined and extended parameter set allows precise predictions in the terahertz region. Structural parameters, such as the bond length and the moment of inertia, have been derived from the spectroscopic parameters.

A main task of this work was the construction and assembly of the new Cologne Supersonic Jet Spectrometer for Terahertz Applications (SuJeSTA).

It is employed to record the spectra of radicals and ions which are produced in a pulsed discharge with a subsequent supersonic jet expansion to obtain adiabatically cooled molecules.

The first application of SuJeSTA has been an intensive investigation of the linear $X\,^2\Pi$ propynylidyne radical, $l - C_3H$. It is supposed to play a decisive role in the carbon chain growth in the interstellar medium and has been subject of astronomical observations (e.g. [4], [5], [6]) and laboratory investigations (e.g. [7], [8], [9]). With SuJeSTA the ν_4 ($^2\Sigma^\mu$) CCH bending vibration of C_3H has been recorded in the submillimeter region for the first time. Due to a strong Renner-Teller effect the bending transitions lie in the submillimeter wavelength region. Eight measured lines have been assigned to ro-vibrational transitions between the vibrational ground state ($^2\Pi$) and the excited bending state $\nu_4 = 1$ ($^2\Sigma^\mu$). In addition, the pure rotational spectrum of C_3H has been investigated up to 600 GHz to extend the number of measured transitions, published in earlier works ([7], [8], [9]). A total of 43 pure rotational lines in the vibrational ground states ($^2\Pi_{1/2}$, $^2\Pi_{3/2}$) and excited state $\nu_4 = 1$ ($^2\Sigma^\mu$) have been recorded. Reliable frequency predictions up to 1 THz are available due to a new set of spectroscopic parameters, obtained from a least squares fit to a standard Hamiltonian.

Furthermore, the new spectrometer facilitates the production of ions. In the course of this thesis, transitions of CO^+ have been recorded to prove the spectrometer's ability of ion production. An isotopically invariant fit of the new data and data published previously [10] resulted in a mass independent parameter set which describes the spectrum of the CO^+ ion up to 1 THz with high accuracy. Improved structural constants have been derived from the spectroscopic parameters. Interstellar CO^+ is of crucial importance for tracing PDRs (Photon Dominated Region) and has been detected in space ([11], [12]).

All obtained data are reliable for frequency predictions up to 1 THz and are available via the Cologne Database for Molecular Spectroscopy (CDMS) [13].

Kurzzusammenfassung

Thema dieser Arbeit ist die hochauflösende Spektroskopie im Terahertzbereich, mit dem Ziel, durch eine quantenmechanische Analyse der Spektren Molekülparameter abzuleiten. Diese sind die Grundvoraussetzung für exakte Frequenzvorhersagen und damit für die astronomische Detektion noch nicht entdeckter Moleküle. Bei den hier vorgestellten Spektralanalysen wurden zwei verschiedene Spektrometer verwendet:

- Das neu entworfene Supersonic Jet Spectrometer for Terahertz Applications (SuJeSTA) zur Untersuchung von kalten Radikalen und Ionen

- Das Kölner Terahertz Spektrometer

Die reinen Rotationsspektren von fünf Isotopomeren des Kaliumchlorids, $^{39}K^{35}Cl$, $^{39}K^{37}Cl$, $^{41}K^{35}Cl$, $^{41}K^{37}Cl$ und $^{40}K^{35}Cl$, wurden mit dem etablierten Kölner Terahertz Spektrometer aufgenommen (siehe z.B. [1], [2]). Dafür wurde eine spezielle Verdampferzelle in das bereits vorhandene Spektrometer integriert, um den Feststoff KCl in die Gasphase zu bringen. Im Rahmen dieser Arbeit wurden insgesamt 295 neue Rotationslinien im Frequenzbereich von 170 bis 930 GHz gemessen. Für die Isotopomere $^{39}K^{35}Cl$ und $^{39}K^{37}Cl$ wurden 107 bzw. 82 Rotationsübergänge, beginnend im Vibrationsgrundzustand bis zum siebten angeregten Zustand, aufgenommen ($v \leq 7$). Dabei lag die höchste J-Quantenzahl bei 127 bzw. 129. Von den selteneren Isotopomeren $^{41}K^{35}Cl$ und $^{41}K^{37}Cl$ wurden 104 Linien gemessen, bei denen $J \leq 128$ und $v \leq 6$ bzw. $J \leq 131$ und $v \leq 5$ waren. Zwei Linien konnten dem $^{40}K^{35}Cl$ zugeordnet werden, dessen natürliche Häufigkeit nur 0,01% von der des $^{39}K^{35}Cl$ beträgt. Die gemessenen Linien dieser Arbeit und die Ergebnisse aus früheren Millimeter-Wellen-Untersuchungen wurden gemeinsam zu einem verbesserten Parametersatz für die untersuchten Isotopomere angepasst. Eine zusätzliche isotopeninvariante Analyse der Daten ergab die massenunabhängigen Dunham-Parameter U_{ij} und die Born-Oppenheimer-Korrektur erster Ordnung Δ_{01}. Der verbesserte und ergänzte Parametersatz ermöglicht exakte Frequenzvorhersagen im Terahertzbereich. Strukturparameter, wie der Bindungsabstand und das Trägheitsmoment, konnten aus den spektroskopischen Parametern abgeleitet werden.

Einer der Schwerpunkte dieser Arbeit war die Konstruktion und der Zusammenbau des neuen Kölner „Supersonic Jet Spectrometers for Terahertz Applications" (SuJeSTA). Es dient zur Aufnahme der Spektren von Radikalen und Ionen, die einer gepulsten Entaldungsquelle entstammen und in einer anschließenden Überschall-Expansion adiabatisch gekühlt werden.

In dieser Arbeit wurde SuJeSTA zu einer umfassenden Untersuchung des linearen $X^2\Pi$ Propynylidyne Radikales ($l-C_3H$) eingesetzt. Man vermutet, dass es eine wichtige Rolle bei der Bildung von Kohlenstoffketten im ISM spielt. Aus diesem Grund war und ist es Gegenstand astronomischer Beobachtungen (z.B. [4], [5], [6]) und Laboruntersuchungen (z.B. [7], [8], [9]). Mit SuJeSTA wurden erstmals Übergänge der ν_4 ($^2\Sigma^\mu$) CCH-Knickschwingung gemessen. Aufgrund des starken Renner-Teller-Effekts liegt die Knickschwingung im Submillimeter-Wellenlängenbereich. Acht gemessene Linien konnten Vibrationsübergängen zwischen dem Grundzustand ($^2\Pi$) und dem ersten angeregten Zustand $\nu_4=1$ ($^2\Sigma^\mu$) zugeordnet werden. Weiterhin wurde das reine Rotationsspektrum von C_3H bis 600 GHz untersucht und der Bereich der gemessenen Übergänge aus früheren Arbeiten damit erweitert ([7], [8], [9]). Insgesamt konnten 43 reine Rotationsübergänge in den Vibrationsgrundzuständen ($^2\Pi_{1/2}$, $^2\Pi_{3/2}$) und im ersten angeregten Zustand $\nu_4=1$ ($^2\Sigma^\mu$) gemessen werden. Der neue Parametersatz aus einem "Least Squares Fit" ermöglicht verlässliche Frequenzvorhersagen bis zu 1 THz.

Mit dem neuen Spektrometer war es ebenfalls möglich, Ionen in der gepulsten Entladungsquelle zu erzeugen. Im Rahmen dieser Arbeit wurden Übergänge des CO^+ verwendet, um die Ionenproduktion und Detektion des Spektrometers unter Beweis zu stellen. Ein isotopeninvarianter Fit der neuen und der früheren Daten [10] ergab einen Satz massenunabhängiger Parameter, welcher das Spektrum des CO^+-Ions bis zu 1 THz mit hoher Genauigkeit beschreibt. Im interstellaren Medium spielt CO^+ eine wichtige Rolle als PDR-Tracer (PDR = Photon Dominated Region) und wurde bereits in mehreren astronomischen Quellen entdeckt ([11], [12]).

Die erhaltenen Daten ermöglichen verlässliche Frequenzvorhersagen bis zu 1 THz und stehen in der Kölner Datenbank für Molekülspektroskopie (CDMS) zur Verfügung [13].

Contents

List of Tables

List of Figures

1

Zusammenfassung

Das interstellare Medium (ISM) enthält eine Vielzahl unterschiedlicher Moleküle. Davon sind bislang rund 130 zweifelsfrei identifiziert. Der Nachweis erfolgt mittels elektromagnetischer Strahlung, die von den gasförmigen Molekülen, Ionen oder Atomen absorbiert bzw. emittiert wird. Für die sichere Identifizierung einer Spezies ist die genaue Kenntnis ihres Spektrums unerlässlich. Diese gewinnt man aus Labormessungen der Übergangsfrequenzen und den daraus resultierenden Molekülparametern für Frequenzvorhersagen. Große Temperaturskalen im interstellaren Raum ermöglichen eine Untersuchung in weiten Bereichen des elektromagnetischen Spektrums. Dennoch wurden die meisten Entdeckungen im Bereich der Zenti-meter- und Millimeter-Wellen gemacht (10–300 GHz), da die Erdatmosphäre oberhalb von 500 GHz - aufgrund des enthaltenen Wasserdampfes - zunehmend undurchsichtiger für astronomische Beobachtungen wird. Der Laborspektroskopie stehen in diesem Wellenlängenbereich mit russischen Rückwärts-Wellen-Oszillatoren (BWOs)leistungsstarke, abstimmbare Strahlungsquellen zur Verfügung. Die in Köln verwendeten decken einen Frequenzbereich von etwa 50 bis 1200 GHz nahezu lückenlos ab.
In naher Zukunft werden Teleskope, die auf neuen Empfängertechniken beruhen, den Terahertz-Frequenzbereich erschließen. Dazu zählen Observatorien wie APEX[1], das flugzeugunterstützte SOFIA[2] oder das HIFI[3]-Instrument an Bord des Herschel-Satelliten. Im Labor stehen neue Entwicklungen, z. B. Übergitter-Strukturen (superlattice) oder Laser-Seitenband-Erzeugung, als Techniken für die Strahlungserzeugung oberhalb von 1 THz zur Verfügung.

Die zweiatomigen Verbindungen bilden eine wichtige und zahlenmäßig große Gruppe von Molekülen. Dieser Gruppe gehören knapp ein Viertel der bisher entdeckten Spezies an, die überwiegend anorganisch sind. 1987 wurden vier Metall-Halogene (*KCl*, *NaCl*, *AlF* und *AlCl*) in der circumstellaren Hülle von IRC+10216 entdeckt (Cernicharo und Guélin [14]). Die relativ hohe

---

[1]Atacama Pathfinder Experiment, 200 $\mu m - 230\ \mu m$ and 300 $\mu m - 1500\ \mu m$
[2]Stratospheric Observatory For Infrared Astronomy, 5 $\mu m - 300\ \mu m$
[3]Heterodyne Instrument for the Far Infrared, 156 $\mu m - 212\ \mu m$ and 240 $\mu m - 624\ \mu m$

interstellare Häufigkeit der beteiligten Atome - alle sind unter den zwanzig häufigsten Elementen zu finden - lässt vermuten, dass die Alkali-Halogene auch in anderen kosmischen Quellen zu finden sind. Jüngst wurde auf dem Jupitermond Io $NaCl$ nachgewiesen [15].

Da Alkali-Halogene einen sehr geringen Dampfdruck aufweisen, erweist sich ihre spektroskopische Untersuchung im Labor als schwierig. Spezielle Techniken sind nötig, um die Moleküle in die Gasphase zu bringen. Aufgrund ihres hohen ionischen Charakters und des damit verbundenen großen Dipolmomentes enthüllen sie jedoch ein Rotationsspektrum mit starken Intensitäten. Erste verlässliche Mikrowellen-Daten stammen aus dem Jahr 1964 (Clouser and Gordy [3]) und wurden 1997 durch Infrarot-Messungen ergänzt (Ram *et al.* [16]).

Im Rahmen dieser Arbeit wurden die reinen Rotationsspektren von fünf Isotopomeren des Kaliumchlorids - $^{39}K^{35}Cl$, $^{39}K^{37}Cl$, $^{41}K^{35}Cl$, $^{41}K^{37}Cl$ - mit dem Kölner-Terahertz-Spektrometer aufgenommen. Dafür wurde eine spezielle Verdampferzelle in das bereits vorhandene Spektrometer integriert, um damit den Feststoff KCl in die Gasphase zu bringen. Es wurden insgesamt 295 neue Rotationslinien im Frequenzbereich von 170 bis 930 GHz gemessen. Für die Isotopomere $^{39}K^{35}Cl$ und $^{39}K^{37}Cl$ wurden 107 bzw. 82 Rotationsübergänge, beginnend im Vibrationsgrundzustand bis zum siebten angeregten Zustand, aufgenommen ($v \leq 7$). Dabei lag die höchste J-Quantenzahl bei 127 bzw. 129. Von den selteneren Isotopomeren $^{41}K^{35}Cl$ und $^{41}K^{37}Cl$ wurden insgesamt 104 Linien bis zu einem J von 128 bzw. 131 gemessen. Dabei entstammten die Übergänge Vibrationszuständen mit $v \leq 6$ bzw. $v \leq 5$. Zwei Linien konnten dem $^{40}K^{35}Cl$ zugeordnet werden, dessen natürliche Häufigkeit nur 0,01% von der des $^{39}K^{35}Cl$ beträgt. Die gemessenen Linien dieser Arbeit und die Ergebnisse aus früheren Millimeter-Wellen-Untersuchungen wurden gemeinsam zu einem verbesserten Parametersatz für die untersuchten Isotopomere angepasst. Eine zusätzliche isotopeninvariante Analyse der Daten ergab die massenunabhängigen Dunham-Parameter U_{ij} und die Born-Oppenheimer-Korrektur erster Ordnung Δ_{01}. Der verbesserte und ergänzte Parametersatz ermöglicht exakte Frequenzvorhersagen im Terahertzbereich. Strukturparameter, wie der Bindungsabstand und das Trägheitsmoment der Moleküle, konnten aus den spektroskopischen Parametern abgeleitet werden.

75 % der interstellar entdeckten Materie sind kohlenstoffhaltige Verbindungen. Sie bilden damit eine weitere wichtige Gruppe interstellarer Moleküle. Kohlenstoff ist das vierthäufigste Element im Kosmos und besitzt ein Vielzahl möglicher Bindungszustände. Von großem Interesse sind hiebei besonders die Kettenmoleküle. Von ihnen sind viele ungesättigt und reaktiv, wie etwa C_n, C_nH, C_nN und HC_nN ($n = 1, 2, 3, ...$). Letztere bilden nur mit einer geraden Anzahl von C-Atomen Radikale. Astronomische Beobachtungen zeigten das Vorhandensein einiger Radikale, z. B in den kalten Molekülwolken TMC-1 und L183 ($l - C_3H$, C_4H, C_5H, C_6H [5]). Anders als im Labor ist das interstellare Medium, mit seinen speziellen Druck-, Dichte- und Temperaturbedingungen, ein Depot für diese Gattung von Molekülen. Viele wurden zuerst astronomisch entdeckt. Laboruntersuchungen hinkten lange Zeit hin-

terher, da technisch ausgefeilte Produktionsmethoden für Radikale fehlten. Heute existierende Spektrometer, die zur Untersuchung an Radikalen herangezogen werden, operieren überwiegend im Infrarotbereich, während der Terahertzbereich weitgehend unerforscht ist.

Einer der Schwerpunkte dieser Arbeit war daher die Konstruktion und der Zusammenbau des neuen Kölner „Supersonic Jet Spectrometers for Terahertz Applications" (SuJeSTA). Es verbindet effektive Quellen zur Erzeugung von Radikalen mit leistungsstarken Terahertz-Quellen. Die Moleküle werden in einer gepulsten Entladung hergestellt und anschließend in einer Überschall-Expansion adiabatisch gekühlt.

In dieser Arbeit wurde SuJeSTA zu einer umfassenden Untersuchungen des linearen $X^2\Pi$ Propynylidyne Radikales ($l-C_3H$) eingesetzt, das vermutlich eine wichtige Rolle bei der Bildung von interstellaren Kohlenstoffketten spielt. Aus diesem Grund war und ist es Gegenstand astronomischer Beobachtungen (z. B. Thaddeus *et al.* [4], Turner *et al.* [5], Kaifu *et al.* [6]).

C_3H ist nicht nur von astrophysikalischem Interesse, sondern auch eine Herausforderung für die Spektroskopie. Erste Informationen zum Molekül ergaben sich aus theoretischen *ab initio* Berechnungen (z.B. [17], [18], [19], [20]), die die Gleichgewichtsstruktur sowie Fein- und Hyperfeinstruktur aufklärten. Ein sehr wichtiger Effekt beim C_3H ist die sehr starke Renner-Teller-Kopplung [21]. Diese führt dazu, dass der untere Energiezustand $^2\Sigma^\mu$ der ν_4 CCH-Knickschwingung zu niedrigen Energien in den Submillimeter-Wellenlängenbereich verschoben wird.

Mit SuJeSTA konnten erstmals Vibrationsübergänge zwischen dem Grundzustand ($^2\Pi$) und dem ersten angeregten Zustand $\nu_4 = 1$ ($^2\Sigma^\mu$) gemessen werden. Weiterhin wurde das reine Rotationsspektrum von C_3H bis 600 GHz untersucht und der Bereich der gemessenen Übergänge aus früheren Arbeiten damit erweitert (Gottlieb *et al.* [7], [8], Yamamoto *et al.* [9]). Insgesamt konnten 43 reine Rotationsübergänge in den Vibrationsgrundzuständen ($^2\Pi_{1/2}$, $^2\Pi_{3/2}$) und im ersten angeregten Zustand $\nu_4 = 1$ ($^2\Sigma^\mu$) gemessen werden. Der neue Parametersatz aus einem "Least Squares Fit" ermöglicht verlässliche Frequenzvorhersagen bis zu 1 THz.

Neben den ungeladenen sind auch die geladenen Spezies von astrophysikalischer Relevanz. Viele (astro-)chemische Reaktionen basieren auf Ionen-Molekül-Reaktionen. Außerdem sind Ionen wie CO^+ und C^+ wichtige PDR-Tracer (PDR = Photon Dominated Region) und wurden bereits in mehreren astronomischen Quellen entdeckt (Störzer *et al.* [11], Erickson *et al.* [12]). Ähnlich wie die Radikale sind auch Ionen unter Laborbedingungen kurzlebig und bedürfen daher eines größeren Aufwandes bei der spektroskopischen Analyse. SuJeSTA ermöglicht, im Gegensatz zur Ionenproduktion in einer DC-Entladung, die Untersuchung von kalten Ionen. Zu Testzwecken wurden mit SuJeSTA erste Messungen am CO^+ vorgenommen und damit der Beweis erbracht, dass das neue Instrument für diesen Zweck geeignet ist. Ein isotopeninvarianter Fit der neuen und der bislang verfügbaren Daten (Klapper [10], Sastry *et al.* [22], Bogey *et al.* [23]) ergab einen Satz massenunabhängiger Parameter, welcher das Spektrum des CO^+-Ions bis zu 1 THz mit hoher

Genauigkeit beschreibt.

2

Introduction

The interstellar medium (ISM) contains a rich variety of molecular species of which more than 130 have been identified beyond doubt by means of their characteristic spectra. Organic and inorganic species with up to 13 atoms have been found in interstellar molecular clouds, circumstellar regions, gas outflows, and planetary atmospheres (see Tab. 2.1). So far, the heaviest element in any detected interstellar compound is iron which is the ninth abundant atom. The elements with masses up to that of *Fe* are produced in nuclear synthesis of active stars and amount almost 100 % of the cosmic mass. The heavier, less abundant (0.0005 %) elements are generated in super novae by proton- or neutron-accretion. The 22 most abundant elements are listed in Tab. 2.2.
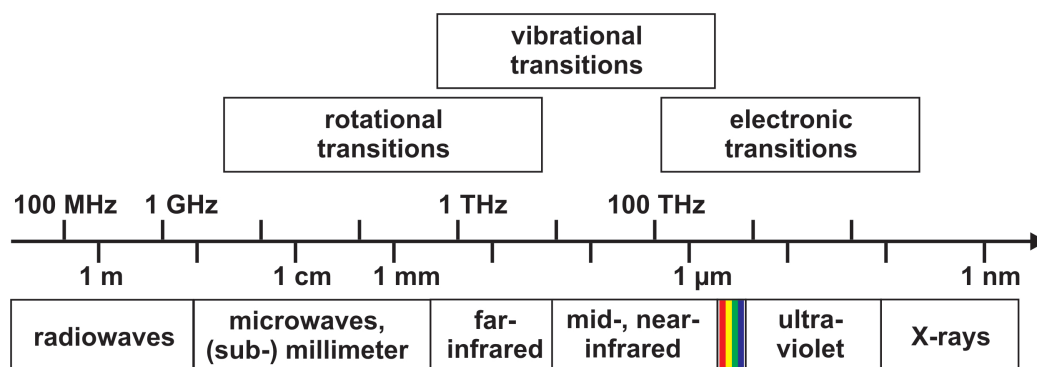
Figure 2.1: Schematic diagram of the electromagnetic spectrum and corresponding interactions of radiation with molecules.

Information about interstellar objects is mainly obtained via detecting electromagnetic radiation which is either emitted or absorbed by gas phase molecules, atoms, and ions. Due to the large temperature scale, ranging from a few Kelvin, in dense molecular clouds and star forming regions, to several hundred Kelvin, in circumstellar shells, a great part of the electromagnetic spectrum is appropriate for analyzing interstellar objects. It is the

submillimeter and millimeter wavelength region (far-infrared), where molecular rotation transitions dominate, adjacent the near- and mid-infrared regime, with vibrations, followed by the optical and ultraviolet part of the spectrum which is caused by electronic transitions (see Fig. 2.1). The unambiguous identification of an interstellar molecular species strongly depends on the precise knowledge of its spectrum which is obtained by measuring transition frequencies in the laboratory and by deriving molecular parameters for further line predictions. Powerful tunable radiation sources, for instance synthesizers and Backward Wave Oscillators (BWOs), are used in laboratory spectrometers to generate radiation in the frequency region up to 1 THz. Especially the spectra of the centimeter and millimeter wavelength region are of great importance, since most of the molecules have been detected in the frequency region between 10 and 300 GHz (see Tab. 2.1).

At frequencies above 500 GHz the earth's atmosphere starts getting opaque for electromagnetic radiation and radioastronomic observations are hampered mainly due to atmospheric water. In near future, telescopes based on new receiver techniques, such as APEX[1], the airborne observatory SOFIA[2], and the HIFI[3] instrument aboard the Herschel satellite, will extend the observable spectral range towards shorter wavelengths, opening the terahertz domain for radioastronomy. In return, new techniques, such as superlattice devices combined with BWOs [24] or laser sideband generation [25], provide electromagnetic radiation sources above 1 THz for laboratory applications (see Fig. 2.2).
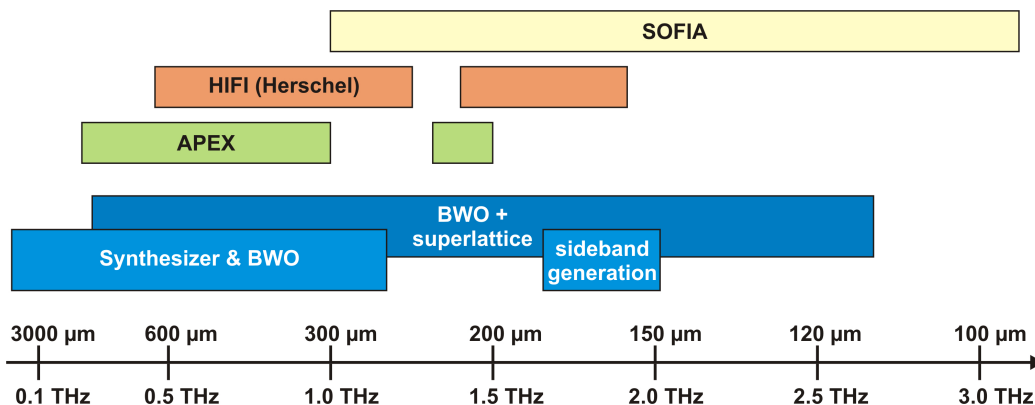
Figure 2.2: Schematic diagram of the frequency coverage of the Cologne terahertz radiation sources (two lower rows) compared to the frequency range of some telescopes (top rows).

In general, molecules split into two groups: Molecules which have a permanent dipole moment and those which do have not. The nonpolar species, for instance C_n, CO_2, C_2H_2, or CH_4, have no pure rotational spectrum. They

---

[1] Atacama Pathfinder Experiment, 200 $\mu m - 230\ \mu m$ and 300 $\mu m - 1500\ \mu m$

[2] Stratospheric Observatory For Infrared Astronomy, 5 $\mu m - 300\ \mu m$

[3] Heterodyne Instrument for the Far Infrared, 156 $\mu m - 212\ \mu m$ and 240 $\mu m - 624\ \mu m$

Table 2.1: List of interstellar molecules detected by means of their rotational spectra in the radio to far-infrared frequency region.

2 atoms	3 atoms	4 atoms	5 atoms	6 atoms
H_2	$C_3{}^*$	$c-C_3H$	$C_5{}^*$	C_5H
AlF	C_2H	$l-C_3H$	C_4H	$l-C_2H_4$
$AlCl$	C_2O	C_3N	C_4Si	$C_2H_4{}^*$
$C_2{}^{**}$	C_2S	C_3O	$l-C_3H_2$	CH_3CN
CH	CH_2	C_3S	$c-C_3H_2$	CH_3NC
CH^+	HCN	$C_2H_2{}^*$	CH_2CN	CH_3OH
CN	HCO	NH_3	$CH_4{}^*$	CH_3SH
CO	HCO^+	$HCCN$	HC_3N	HC_3NH^+
CO^+	HCS^+	$HCNH^+$	HC_2NC	HC_2CHO
CP	OHC^+	$HNCO$	$HCOOH$	NH_2CHO
SiC	H_2O	$HNCS$	H_2CNH	C_5N
HCl	H_2S	$HOCO^+$	H_2C_2O	$l-HC_4H^*$ (?)
KCl	HNC	H_2CO	H_2NCN	$l-HC_4N$
NH	HNO	H_2CN	HNC_3	
NO	$MgCN$	H_2CS	$SiH_4{}^*$	
NS	$MgNC$	H_3O^+	H_2COH^+	
$NaCl$	N_2H^+	$c-SiC_3$		
OH	N_2O	$CH_3{}^*$		
PN	$NaCN$			
SO	OCS			
SO^+	SO_2			
SiN	$c-SiC_2$			
SiO	$CO_2{}^*$			
SiS	NH_2			
CS	H_3^{+*}			
HF	H_2D^+			
SH^*	HD_2^+			
HD	$SiCN$			
FeO (?)	$AlNC$			
O_2 ?	$SiNC$			

7 atoms	8 atoms	9 atoms	10 atoms	11–13 atoms
C_6H	CH_3C_3N	CH_3C_4H	CH_3C_5N	HC_9N
CH_2CHCN	$HCOOCH_3$	CH_3CH_2CN	$(CH_3)_2CO$	$C_6H_6{}^*$ (?)
CH_3C_2H	CH_3COOH	$(CH_3)_2O$	$(CH_2OH)_2$ (?)	$CH_3OC_2H_5$
HC_5N	C_7H	CH_3CH_2OH	H_2NCH_2COOH ?	$HC_{11}N$
CH_3CHO	H_2C_6	HC_7N	CH_3CH_2CHO	
CH_3NH_2	CH_2OHCHO	C_8H		
$c-C_2H_4O$	$l-HC_6H^*$ (?)			
H_2CCHOH	CH_2CHCHO (?)			

* indicates molecules that have been detected by ro-vibrational spectroscopy.

** indicates molecules that have been detected by electronic spectroscopy.

l indicates linear molecules.

c indicates cyclic molecules.

? indicates a questionable or (probable) tentative detection

can be identified by means of infrared active transitions in the near- and mid-infrared belonging to ro-vibrational modes. The molecules with a permanent dipole moment can be traced by means of pure rotational transitions in the millimeter and submillimeter wavelength region. Additionally, many chain molecules also have low energy bending vibrations in the terahertz region.

An important class of interstellar species are diatomic compounds. The list of diatomic molecules detected currently comprises of 30 entries two third of which are inorganic species. In 1987, Cernicharo and Guélin reported the detection of four metal halides, i.e. *KCl*, *NaCl*, *AlF*, and *AlCl*, towards the circumstellar envelope of late type star IRC+10216 [14]. The relative high cosmic abundance of aluminium, sodium, potassium, and chlorine, i.e. the 13th, 14th, 20th, and 19th most abundant element (see Tab. 2.2), lend encouraging motivation to continue searching for metal halides towards hotter and even denser core regions. The recently detected rotational lines of *NaCl* on Jupiter's moon Io at frequencies of 143 and 234 *GHz* [15] demonstrate how special conditions, for instance continuous volcanic output, can produce spectroscopical measurable amounts of *KCl*, *NaCl*, etc.
Experimental studies on diatomic gas phase alkali halides in the laboratory are complicated due to the low vapor pressure of these molecules. Special vaporization conditions are necessary to provide them for gas phase spectroscopy. On the other hand, these species possess a very large dipole moment because of their highly ionic character. This means, they reveal a pure rotational spectrum with mainly large intensities. Reliable data on the alkali halides is rare. First spectroscopic data of *NaCl*, *RbCl*, and *CsCl* in the millimeter wavelength range was published already in 1964 [3]. In 1997, the infrared emission spectra of *KCl* and *NaCl* were published [16]. First high resolution measurements on sodium chloride in the *THz* region were performed with the Cologne terahertz spectrometer in 2001 (Caris *et al.* [26], [2]).

In the course of this work, high resolution measurements on five isotopomers of potassium chloride, i.e. $^{39}K^{35}Cl$, $^{39}K^{37}Cl$, $^{41}K^{35}Cl$, $^{41}K^{37}Cl$ and $^{40}K^{35}Cl$, have been performed up to 930 *GHz* with the Cologne terahertz spectrometer. A special evaporation cell has been used. The obtained data has been analyzed in an isotopically invariant form and a new set of invariant Dunham parameters has been derived including the first order Born-Oppenheimer breakdown corrections. With these molecular constants, reliable frequency predictions for the spectra of all six isotopomers are available which open the field for further astronomical detections.

A plethora of detected interstellar molecules contains one or more carbon atoms (75 %). Carbon is the fourth abundant element, after hydrogen, helium, and oxygen, and reveals a wealth of possible chemical bondings. One characteristic feature of the carbon atom is the tendency to build chain molecules, such as the stable cyano-polyynes, HC_nN (with $n = 1, 3, 5, ...$). This type of molecules has been detected in many astronomical sources, for instance towards the circumstellar envelope IRC+10216 (e.g. *HCN* [28], [29];

Table 2.2: Cosmic abundance of the elements normalized to $Si = 10^6$. Values taken from the publication of A. G. W. Cameron [27].

Element	Symbol	Abundance
Hydrogen	H	$3.18 \cdot 10^{10}$
Helium	He	$2.21 \cdot 10^9$
Oxygen	O	$2.15 \cdot 10^7$
Carbon	C	$1.18 \cdot 10^7$
Nitrogen	N	$3.74 \cdot 10^6$
Neon	Ne	$3.44 \cdot 10^6$
Magnesium	Mg	$1.061 \cdot 10^6$
Silicon	Si	$1.00 \cdot 10^6$
Iron	Fe	$8.3 \cdot 10^5$
Sulfur	S	$5.0 \cdot 10^5$
Argon	Ar	$1.172 \cdot 10^5$
Calcium	Ca	$7.21 \cdot 10^4$
Aluminium	Al	$8.5 \cdot 10^4$
Sodium	Na	$6.0 \cdot 10^4$
Nickel	Ni	$4.80 \cdot 10^4$
Chromium	Cr	$1.27 \cdot 10^4$
Phosphorus	P	9600
Manganese	Mn	9300
Chlorine	Cl	5700
Potassium	K	4200
Titanium	Ti	2775
Fluorine	F	2450
All other elements		5069

HC_3N [30]; HC_5N, HC_7N [31]).

Besides the persistent carbon chains, there are numerous unsaturated and reactive molecules, for instance C_nH, C_nN, pure carbon chains C_n (with $n = 1, 2, 3, ...$), and those cyano-polyynes with even numbers of carbon atoms. They are of significant astrophysical relevance and have been observed, for instance towards cold molecular clouds, such as TMC-1 and L183 (e.g. $l - C_3H$, C_4H, C_5H, C_6H [5]). Unlike the laboratory, the interstellar medium with ultralow pressure, density, and temperature conditions is a repository for this class of molecules. Thus, many radicals have been detected first by radio astronomers rather than in the laboratories, for example C_3N [32] and C_4H ([33], [34], and [35]) which were first observed in 1977 and 1978, respectively. The frequency predictions for theses detections had to be taken from ab inito calculations, since laboratory spectroscopy could not catch up with the interstellar detections for a long time until sophisticated production methods were developed. Nowadays, laboratory spectrometers for the investigation of radicals are available mainly in the infrared region, while the terahertz range is barely involved in the investigation of reactive species.

The Cologne Supersonic Jet Spectrometer for Terahertz Applications (SuJeSTA) has been developed within the scope of this thesis to overcome this lack of terahertz data for radicals. The new instrument combines an efficient source for radicals and a powerful terahertz radiation source to obtain high resolution spectra of the instable species and to provide the necessary laboratory data for future search for reactive, interstellar species. The molecules are formed by means of a pulsed discharge in the throat of a slit nozzle. The subsequent adiabatic, supersonic expansion into the vacuum chamber is almost collision-free and cools the rotational degree of freedom of the gas molecules to a few Kelvin. SuJeSTA is embedded in the international network of the Laboratoire Europeén Associé (LEA *HiRes*) which aims at developing a regional structure promoting the applications of high resolution spectroscopy in the field of molecular physics. Applications concern planetary science, atmospheric studies, astrophysics of the interstellar medium, time dependent chemistry, analytical chemistry, and process analysis.

The first application of SuJeSTA has been an investigation of the linear $X^2\Pi$ propynylidyne radical, $l - C_3H$. This chain molecule has been subject of many astronomical observations, since it is supposed to play a major role in the carbon chain growth in the interstellar medium. The linear C_3H radical in its vibrational ground state was first detected by Thaddeus *et al.* [4] towards IRC+10216 and the cold dark cloud TMC-1 in 1985. In 2000, Turner *et al.* [5] reported cyclic and linear C_3H in three small translucent molecular clouds (CB 17, CB 24, and CB 228), in TMC-1, and L183. The most recent detection of C_3H stems from an extensive spectral line survey towards TMC-1 (Kaifu *et al.* in 2004 [6]).

The C_3H radical is not only of astrophysical interest, but also a challenging molecule for spectroscopists. First information on C_3H came from theoretical studies. *Ab initio* calculations revealed the equilibrium geometric structure and provided vibrational frequencies ([17], [18], [19]). Effects, such as

spin-orbit coupling due to the $^2\Pi$ electronic ground state, and the hyperfine structure due to the nuclear spin of the hydrogen, were treated in many publications (e.g. [36], [37], [20]). Recently Perić *et al.* [21] investigated the Renner-Teller effect of C_3H, resulting from a coupling of the electronic angular momentum and the bending vibrational motion. Due to this strong coupling, the lower $^2\Sigma^\mu$-state of the ν_4 *CCH* bending mode is shifted towards lower energies and into the submillimeter region. This effect is typical for carbon chains and the understanding of its nature will support *ab initio* calculations of other chain molecules.

SuJeSTA has facilitated the first experimental study of this Renner-Teller shift due to the precise data of ro-vibrational transitions of the $^2\Sigma^\mu$-$^2\Pi_{3/2}$ band system, which is described in this work. A reasonable value for the Renner-Teller constant ε of C_3H has been evaluated, based on these measurements. Furthermore, the value of the excitation energy E_{ν_4} of the ν_4 ($^2\Sigma^\mu$) state has been strongly improved.

Another interesting feature of C_3H is a Coriolis coupling which causes perturbations of the rotational levels in the ground and the vibrationally excited states. First accurate values for the Coriolis interaction constant will be presented in this work. The pure rotational transitions in both $^2\Pi$ ground states and in the first excited vibrational state $\nu_4 = 1$ ($^2\Sigma^\mu$) have been recorded up to 600 *GHz* and the earlier measurements by Gottlieb *et al.* (1985 [7] and 1986 [8]) and Yamamoto *et al.* (1990 [9]) below 360 *GHz* have been substantially extended. From a least squares fit to a standard Hamiltonian a new set of molecular parameters has been obtained which is most reliable to predict transition frequencies up to 1 *THz*.

Besides uncharged molecules, ions represent another class of astrophysically important species. Like radicals, these molecules are usually instable under laboratory conditions and difficult to analyze by spectroscopical methods. However, they are abundant in the interstellar medium and play a major role in astrochemistry, since many chemical reactions involve ions.

Furthermore, ions, such as CO^+ and C^+, play a decisive role as PDR tracer (Photon Dominated Region). In the interstellar medium, the CO^+ ion is rare and normally optically thin due to its reactivity, for instance with H_2 to HCO^+. With knowledge of the column density of CO^+ chemical models of PDRs are verified [11]. The first detection of CO^+ towards OMC-1, a molecular cloud in the Orion nebula, was reported by Erickson *et al.* [12] in 1981. Twelve years later, Latter *et al.* [38] observed CO^+ in the planetary nebula NGC7027 and in the interstellar medium (M17SW).

SuJeSTA facilitates the analysis of adiabatically cooled ions in the terahertz region - in contrast to the production of ions in a DC glow discharge, where the ions usually have high rotational temperatures [10]. In this work, the carbon monoxide ion, CO^+, has been used as a test molecule. It turned out, that SuJeSTA is an expedient instrument for the spectroscopy of cold ions in the terahertz region and pure rotational transitions of CO^+ in the vibrational ground state have been observed.

CO^+, generated in glow discharges, was investigated in many laboratory mi-

crowave studies in the 1970s and 1980s ([39], [22], [40], and [23]). The latest set of isotopically invariant Dunham parameters was determined in the early 1980s. A very recent extensive investigation of the isotopomers $^{12}CO^+$ and $^{13}CO^+$ in the terahertz domain was carried out by Klapper [10] employing the Cologne Terahertz Spectrometer.
An updated isotopically invariant analysis of CO^+ including the Born-Oppenheimer breakdown corrections was not available, yet. Thus, the observed lines together with earlier data have been fitted in a mass independent least squares fit. The isotopically invariant mass-reduced Dunham parameters and the first order Born-Oppenheimer breakdown corrections for C and O have been determined. The resultant invariant parameter set of this work provides reliable frequency predictions for all isotopomers of CO^+ and encourages the astronomical search for those with low abundances.

Although the species which have been analyzed in this thesis require certain experimental setups and belong to different categories of molecules, they have all been investigated in the terahertz regime by means of laboratory spectroscopy. The rotational and, in case of C_3H, bending vibrational spectra have been analyzed with quantum mechanical methods to derive appropriate molecular parameters for their description. Upon these results the spectra are predictable in a wide range and the transition frequencies are available via the Cologne Database for Molecular Spectroscopy (CDMS) [41], [13].

3

Experimental Setup

The main aim of the present work is to combine a terahertz radiation source with a supersonic jet, to perform high resolution terahertz spectroscopy on molecular radicals and ions. For this purpose, the new Cologne Supersonic Jet Spectrometer for Terahertz Applications (SuJeSTA) has been setup which is described in Section 3.1. For the measurements on KCl the Cologne Terahertz Spectrometer has been used which has been described by Winnewisser *et al.* [1] in detail and in Section 3.2 of this work only briefly. Further details on the radiation sources are given in Section 3.3.

3.1 Supersonic Jet Spectrometer for Terahertz Applications

A main task in the course of this work was the construction and assembly of the new Cologne Supersonic Jet Spectrometer for Terahertz Applications (SuJeSTA). Extensive tests were performed to derive technical parameters, such as the amount of produced molecular transient species and lower limits for their detection. In a first scientific application SuJeSTA has been used to study pure rotational and ro-vibrational transitions of the linear C_3H radical (see Chapter 6). The new spectrometer has also been used to perform measurements on adiabatically cooled CO^+ ions (see Chapter 7).

The short absorption pathes and the low column densities of a jet spectrometer require a strong and stable radiation source besides a very sensitive detecting system. Backward wave oscillators provide enough power in the submillimeter and millimeter wavelength region to operate a terahertz jet spectrometer. SuJeSTA can be used in two different operational modes (see Section 3.3.2), either in a frequency stabilized mode or in a free-running mode: A highly precise mode for scans over small intervals, usually of 10–20 MHz width (see Fig. 3.1) and a fast scanning mode which covers a large frequency range of several hundred MHz (see Fig. 3.2). The less accurate
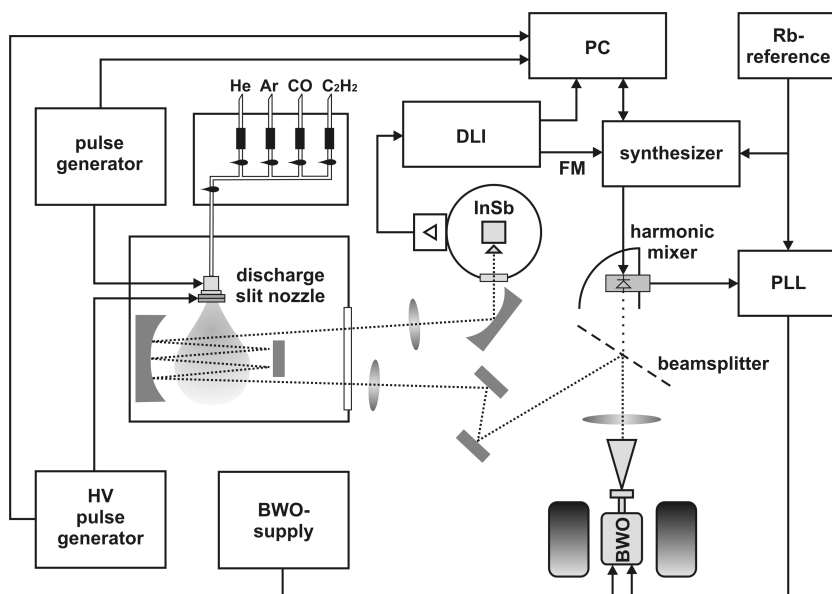
Figure 3.1: Experimental setup of the Cologne Supersonic Jet Spectrometer for Terahertz Applications (SuJeSTA). Frequency stabilized Backward Wave Oscillators (BWOs) are used as radiation sources. The signal is detected on a liquid helium cooled *InSb* Hot Electron Bolometer. A pulsed discharge slit nozzle produces radicals, e.g. C_3H from a C_2H_2 / CO gas mixture diluted in *He* or *Ar* at 1–6 *bar* backing pressure. In a subsequent supersonic expansion the molecules are adiabatically cooled. The probing microwave beam intersects the molecular jet six times in a multipath optics which leads to an overall absorption path length of approximately 30 *cm*. This operational mode of SuJeSTA is used to record spectra of 10–20 *MHz* band width.

fast mode using a free-running BWO is applied when searching for absorption lines of less known, or completely unknown species. In this work the frequency stabilized mode with high spectral resolution and 10 *kHz* of accuracy is presented. In this context also superlattice devices have been used as radiation source. In addition, a 16 path Herriott-type cell particular constructed for the use with terahertz applications increases the sensitivity of the spectrometer significantly (see Fig. 3.3 and Section 3.1.2).

All optical devices (see Figs. 3.1–3.3), such as lenses, windows, and mirrors, are made of aluminium or brass with smoothly polished surfaces for high reflectivity. Lenses with different focal lengths and all windows were made of Teflon or HDPE, both offering high transmittance for millimeter and submillimeter waves. The absorption coefficient α of HDPE at room temperature is equal to ~ 0.077 cm^{-1} at frequencies around 600 *GHz* ([42], [43], [44], [45]). The thickness of lenses and windows is in the order of 0.5–3 *cm* which gives sufficient transmission.

Figure 3.2: Experimental setup of the Supersonic Jet Spectrometer for Terahertz Applications in the free-running operational mode. In this setup of SuJeSTA, the Backward Wave Oscillators (BWOs) are not frequency stabilized by a phase lock loop (free-running mode). The frequency is tuned by a function generator which applies a voltage ramp to the BWO. In the fast scanning mode, a spectrum of several hundred MHz is taken during a single pulse of the discharge source. The frequency accuracy is lower than it is with frequency stabilization.

3.1.1 Discharge and Supersonic Jet

Several methods, such as laser ablation, glow discharge, and pulsed discharge with subsequent supersonic expansion, are applicable for the production of cold radicals and ions [46]. The supersonic jet spectrometer, SuJeSTA, has been used with two different types of discharge nozzles:

- pulsed discharge pinhole nozzle

- pulsed discharge slit nozzle

In the present work both nozzles have been fed with a mixture of the appropriate precursor gasses at a backing pressure of 1–10 bar, whereas the constant flow of the gas has been controlled by flow regulators. To achieve a certain type of product molecules particular mixtures had to be used which are listed in Tab. 3.1. The precursors have been diluted in inert gases, such as He and Ar, to advance the cooling process. The C_3H radical, the CO^+ ion, as well as the stable molecules, HCN and HNC, have been produced by means of this technique. Furthermore, energetically low lying rotational transitions of stable molecules, for instance CO and its isotopomers, have been analyzed, taking advantage of low rotational temperatures due to adiabatic expansion of the gas.

Figure 3.3: Experimental setup of the Supersonic Jet Spectrometer for Terahertz Applications with a superlattice device (SLED) pumped by a synthesizer. The power emitted by the SLED at higher harmonics is much lower than that of a BWO. The Herriott type multi pass optics was installed to increase the sensitivity due to 16 passes.

Radical and ions are produced in the plasma of an electrical discharge. This can be done either in a static glow discharge or in a pulsed mode, where a short gas pulse of up to a few hundred microseconds goes along with a discharge pulse of several hundred Volts and similar duration. The timing of the pulses is very decisive and has to be adjusted in each individual case.

Adiabatic Expansion

All gases cool when they expand adiabatically. The rapid expansion of a system in a supersonic jet with high pressure differences prevents the transfer of energy. In this work, the factor between high and low pressure was usually larger than 10^5. A gas expansion from a region with pressure p_0 into a vacuum chamber with background pressure p_b is regarded as supersonic if the following equation is satisfied:

$$\frac{p_0}{p_b} > G = \left(\frac{\gamma+1}{2}\right)^{\frac{\gamma}{\gamma-1}} \quad with \quad \gamma = \frac{c_p}{c_V} = \frac{f+2}{f} \tag{3.1}$$

Here γ is the adiabatic exponent and f is the degree of freedom of the molecules. G is always smaller than 2.1 for all gases. In an idealized adiabatic process the temperature and pressure of the molecules are correlated by the following expression:

$$\frac{T}{T_0} = \left(\frac{p_b}{p_0}\right)^{\frac{\gamma-1}{\gamma}} \tag{3.2}$$

Table 3.1: Precursor gas mixture for production of particular molecule.

Product	Precursor	Nozzle	Back. press.	Dis. voltage	Rep. rate
HCN	1–2 % C_2H_2 15 % N_2 He	pinhole	5–10 bar	800–1200 V	50 Hz
HNC	1–2 % C_2H_2 15 % N_2 He	pinhole	5–10 bar	800–1200 V	50 Hz
C_3H	1.5–2.3 % C_2H_2 63–44 % CO He	slit	2–6 bar	800–1100 V	50 Hz
CO^+	30–50 % CO Ar	slit	1–4 bar	800–1100 V	50 Hz

Here T_0 and p_0 are the stagnation temperature and pressure, respectively, and p_b is the background pressure in the vacuum chamber during the expansion. A temperature of $T_{He} = 2.3\ K$ is calculated from this expression for the adiabatic expansion of helium atoms (with $\gamma_{atoms} = \frac{5}{3}$, $T_0 = 300\ K$, $p_0 = 4\ bar$, $p_b = 2 \cdot 10^{-5}\ bar$).

A gauge for the velocity of a flow is its Mach number, which is defined as $M = \frac{v}{v_s}$ where v_s is the speed of sound in the medium. The molecular beam is supersonic if $M \geq 1$. The expansion accelerates the particles to large Mach numbers. Thus, for a certain area of the jet, called Zone Of Silence (ZOS), the molecules in the flow are not influenced, for instance by the background pressure. The following expression for the isentropic temperature is derived for the ZOS from further assumptions (see e.g. Scoles [47] for more details):

$$T_{isentropic} = \frac{T_0}{1 + \frac{\gamma-1}{2}M^2} \qquad (3.3)$$

The low rotational temperature of molecules in an adiabatically expanded molecular beam allows spectroscopical investigation of their lowest energy states. A way to calculate the rotational temperature of the molecular jet is the comparison of the intensity of two adjacent rotational transitions (($J_i + 1) \leftarrow J_i$ and $(J_j + 1) \leftarrow J_j$) by means of the formula:

$$T_{rot} = \frac{-2 \cdot 10^6 \cdot B \cdot h \cdot (J_i + 1)}{k_B \cdot ln\left(\frac{N_i \cdot (2J_i + 3)}{N_j \cdot (2J_i + 1)}\right)} \qquad with \qquad J_j = J_i + 1 \qquad (3.4)$$

where B is the rotational constant in MHz, N_i and N_j are the intensities of the lower and upper transition, respectively. From the intensities of the two transitions of $^{13}C^{16}O$, $3 \leftarrow 2$ and $4 \leftarrow 3$ at 330587.9 MHz and 440765.1 MHz, respectively, a temperature of approximately 40 K was derived. From Eq.

3.3 the Mach number for helium at 40 K ($v_s(He) \simeq 370\frac{m}{s}$) is calculated to $M \simeq 4$. This is in full agreement with the experimental results (see Fig. 3.6 in the next Section), since the transitions probed parallel to the direction of jet propagation show a Doppler-shift of approximately 1400 $\frac{m}{s}$.

The adiabatic expansion of particles has been discussed in detail elsewhere, e.g. in the textbook of Scoles [47]. The process in connection with spectroscopical applications is treated for example in the works of Balle *et al.* [48] and Fuchs [49].

Discharge Pinhole Nozzle
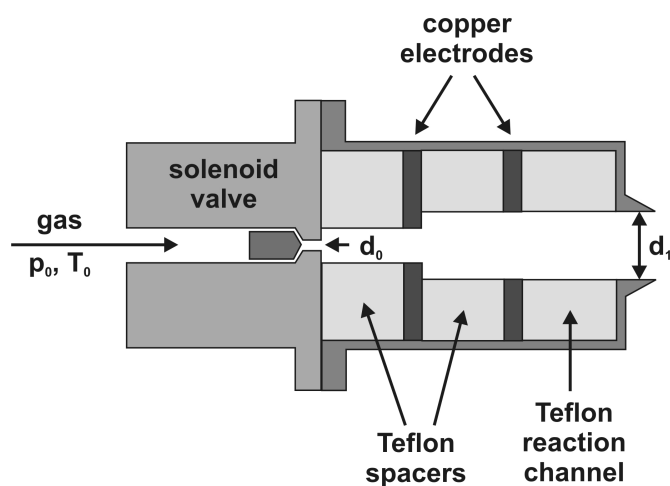
Figure 3.4: Discharge nozzle consisting of solenoid valve (orifice $d_0 = 1$ mm) and the subsequent discharge tube with teflon spacers (5–10 mm), copper electrodes (thickness 1 mm), and reaction channel (20 mm, $d_1 = 5$ mm). A voltage of 800–1200 V is applied to the electrodes. The discharge tube was designed by Thaddeus and co-workers at the Harvard University.
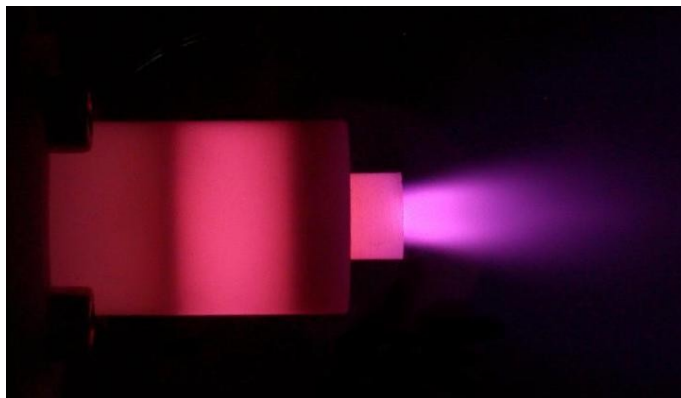
Figure 3.5: Discharge of C_2H_2, N_2, and He at a backing pressure of 4 bar for HCN production in a discharge pinhole nozzle.

One kind of discharge nozzle (Harvard source) is schematically shown in Fig. 3.4. The discharge tube was designed by Thaddeus and co-workers at the Harvard University. Nozzles similar to the ones used in this thesis were first described by Schlachta *et al.* [50]. Another comprehensive study on the source was performed by Fuchs [49].
The sample gas enters the nozzle via a solenoid valve (General Valve pulsed 9 series) which is mounted on a Teflon casing. The casing contains a Teflon spacer with 5–10 *mm* of length and two oxygen-free high conductivity copper electrodes with 1 *mm* of thickness which are separated by a second Teflon spacer (5–10 *mm*). A short discharge pulse is applied to the electrodes where the pressure of the flow gas is still high. Downstream a third spacer of up to 20 *mm* of length acts as reaction channel, where the transient species are formed. The transient species are formed in the downstream reaction channel. In the generated plasma the molecules of the carrier gas are electronically excited. The emission of light from the adiabatically expanding gas into the vacuum chamber can be seen by the naked eye (see Fig. 3.5). Subsequently the gas is adiabatically cooled in a supersonic jet expansion. The jet is intersected by the probing radiation beam in the zone of silence.
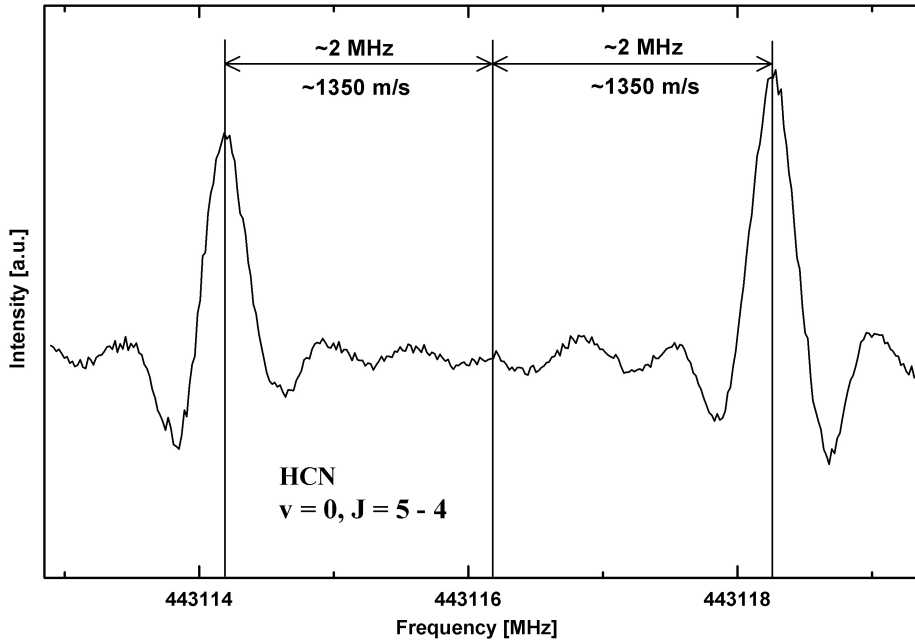
Figure 3.6: Absorption signal of *HCN*, produced in a pulsed discharge in the throat of a pinhole nozzle. The two lines are Doppler components of the $J = 5 \leftarrow 4$ transition in the vibrational ground state at originally 443116.1493 *MHz*. The line shift from the center position is approximately 2 *MHz* in each direction which corresponds to $v_{rel} \cong \pm 1350 \frac{m}{s}$. It arises from the parallel alignment of the jet and the probing microwave beam.

The discharge pinhole nozzle was very efficient in producing *HCN* and *HNC*. These molecules have been used as test molecules to derive timing values for this molecular source. A constant gas mixture (1–2 % C_2H_2, 15 % N_2, and *He*) at a backing pressure of 5–10 *bar* was applied to the nozzle. A 150–200 μs discharge pulse of 800–1200 *V* was synchronized with a 300–350 μs gas pulse. The discharge current was typically between 400 and 800 *mA*. The first electrode (the one next to the valve) was always grounded while the second electrode served as cathode. In the first setup, the optical path of SuJeSTA was aligned in a way that the direction of propagation of the molecular jet and the probing microwave beam were parallel (see Section 3.1.2), which resulted in two Doppler-shifted absorption lines. Fig. 3.6 shows a spectrum of the two Doppler components of the $J = 5 \leftarrow 4$ transition of *HCN* in the vibrationally ground state. Each is shifted about 2 *MHz* from the center position which is originally located at 443116.1493 *MHz*. This shift corresponds to a relative velocity of approximately $\pm 1350 \frac{m}{s}$. From the intensity weighted mean frequency of the two Doppler lines the transition frequency is determined. The width of each line is about 500 *kHz*.

This type of molecular source was also used in the perpendicular setup of SuJeSTA together with a multipath optics (see Section 3.1.2). Unfortunately, this source proved not to be appropriate to produce measurable amounts of C_3H.

Discharge Slit Nozzle
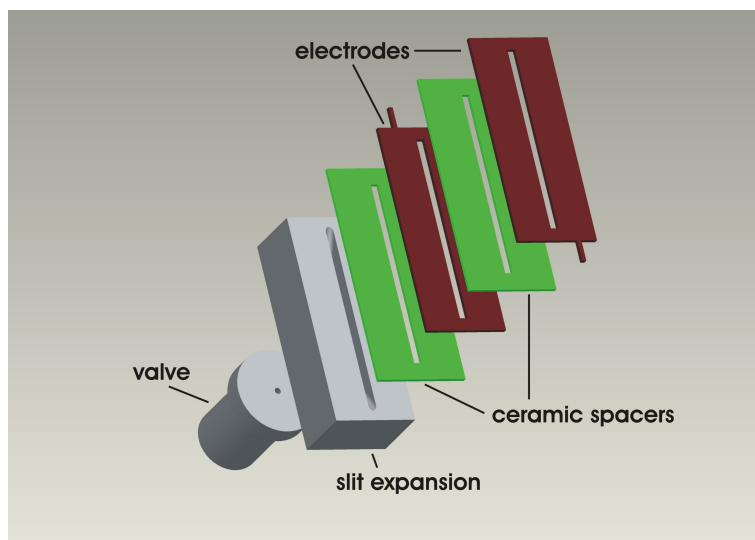
Figure 3.7: Discharge slit nozzle consisting of the valve, the slit pre-expansion (width = 1–2 *mm*, length = 3 *cm*), and the discharge unit with two electrodes separated 1 *mm* by ceramic spacers and mounted in front of the valve. [51].

Another effective source for radical and ion production is a discharge slit nozzle (Basel source). The setup of this source is shown in Fig. 3.7. A

detailed description of this source is given by Linnartz et al. [51] who was significantly involved in its development.
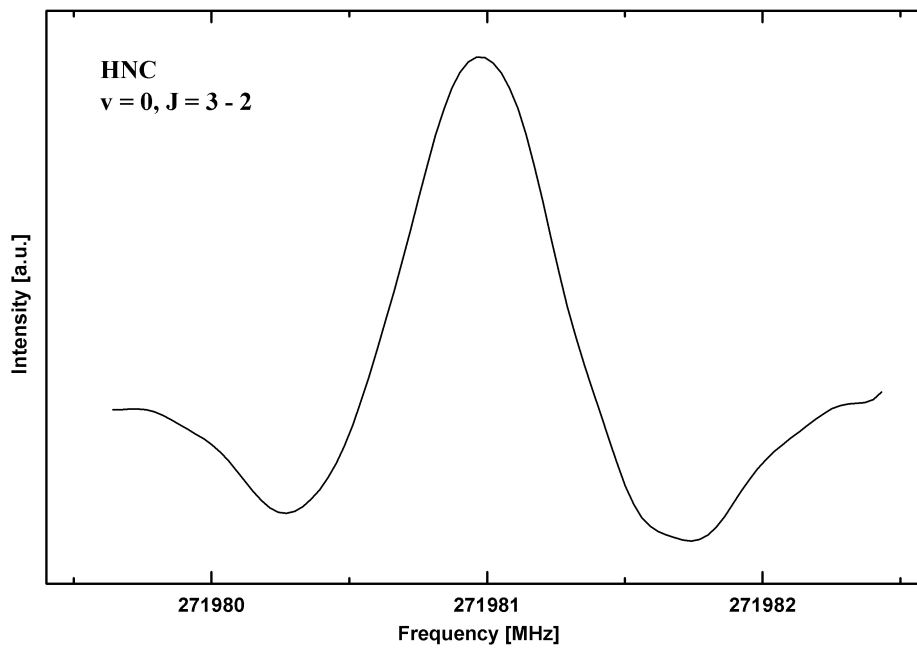
Figure 3.8: Spectrum of *HNC*, produced in a pulsed discharge in the throat of a slit nozzle. The $J = 3 \leftarrow 2$ transition belongs to the vibrational ground state and is located at 271981.142 *MHz*. In this case, the radiation was provided by a superlattice device pumped by a synthesizer at a frequency of 90660.3807 *MHz*.

A pinhole nozzle injects the gas mixture into a slit of 3 *cm* length and 1–2 *mm* width, where a pre-expansion takes place. Two metal blades are used as electrodes separated 1 *mm* by ceramic spacers and mounted in front of the valve. A discharge voltage of 500 to 1200 *V* was typically applied to the electrodes. The microwave radiation probes the jet approximately 5 *cm* downstream and perpendicular to the direction of jet propagation (see Section 3.1.2).

The discharge slit source facilitated the formation of C_3H (discharge of C_2H_2 and *CO* diluted in *He*), CO^+ (discharge of *CO* diluted in *Ar*), and several stabile molecules, such as *HCN* and *HNC* (discharge of C_2H_2 and N_2 diluted in *He*). Fig. 3.8 shows an *HNC* transition at 271981.142 *MHz* in the vibrational ground state. Due to the perpendicular alignment of jet and probing beam (see Section 3.1.2) no Doppler shifts occur. In this case the radiation was provided by a superlattice device pumped by a synthesizer at a frequency of 90660.3807 *MHz*.

The production details for C_3H and CO^+ will follow in the Chapters 6 and
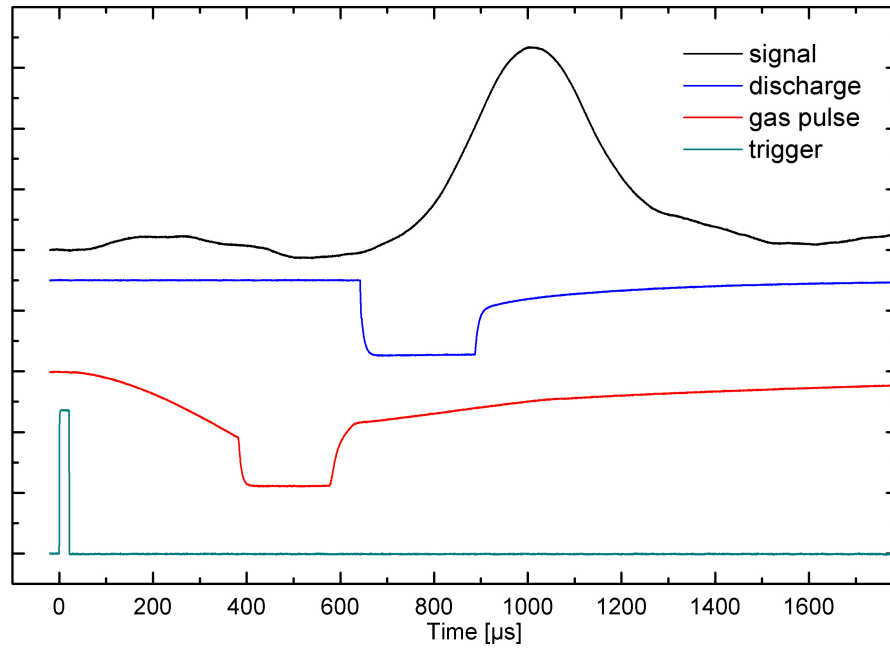
Figure 3.9: Exemplary Timing with the pulsed discharge slit nozzle: In black the detected signal is displayed; the blue and red curve show the discharge and gas pulse, respectively; the turquoise curve represents the system-trigger.

7. Fig. 3.9 exemplarily shows the timing of the pulsed discharge slit nozzle for C_3H formation. The black curve is the online signal from the detector. Its trend is proportional to the absorbed radiation. In red the gas pulse with a length of about 200 μs is shown followed by a 280 μs discharge pulse in blue. The turquoise curve is the system-trigger which was synchronized to the AC-line frequency which resulted in a repetition rate of 50 Hz. In this example the maximum of the absorption signal (black curve) occurs within a 160 μs time window, 930 μs after the trigger.

3.1.2   Vacuum Chamber and Multipath Optics

The environment, where the molecules expand adiabatically, plays a decisive role for the production of radicals and ions. Besides a steady flow of gas and defined discharge parameters, stable pressure conditions are necessary, either with the jet on or off. These surroundings are provided by the vacuum chamber which also holds some of the optical arrangements to guide the probing beam. The one designed for the Supersonic Jet Spectrometer has been built in shape of a cube with dimension of $60\ cm\ \times\ 60\ cm\ \times\ 50\ cm$ (length × width × height). It has been constructed of six aluminum plates, mounted on an aluminum frame. Each plate is detachable, so that the setup within the chamber is accessible from all sides. The chamber is attached to a vibration-free supported table which also carries the radiation source, microwave mirrors, lenses, and detector. The chamber's top plate is connected to the pumping system, consisting of a two stage roots blower and a booster pump with a total pumping speed of $\sim 4600\ m^3/h$. The chamber pressure has not exceeded $5 \cdot 10^{-2}\ mbar$ during the measurements, where the molecular jet has been pulsed with a repetition rate of usually $50\ Hz$. Without jet the pressure is below $10^{-3}\ mbar$. The front plate is equipped with a Teflon microwave window which serves as entrance and as exit for the radiation beam. Its dimension is $125\ mm\ \times\ 75\ mm$ (width × height) and a thickness of $8\ mm$. The angle between the window's plane and the direction of propagation of the microwave beam is less than 90° to minimize standing wave etalon effects.
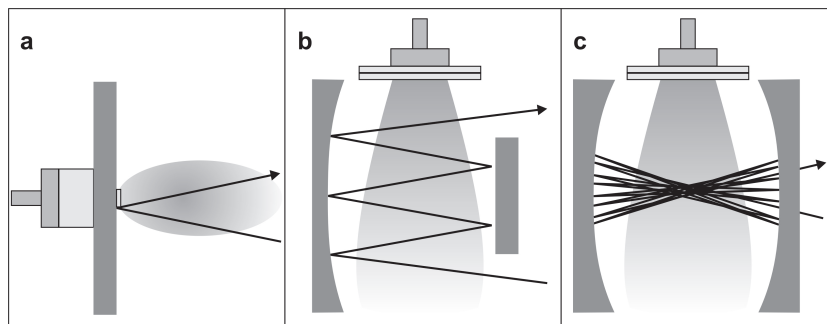
Figure 3.10: Optical pathes for probing the molecular jet: a) 2 passes parallel to the direction of jet propagation b) 6 passes perpendicular to the direction of jet propagation c) 16 passes through a Herriott type optics.

Three different geometrical setups are possible to probe the molecular jet with the radiation of a BWO or a SLED (see Fig. 3.10):

a) 2 passes parallel to the direction of jet propagation

b) 6 passes perpendicular to the direction of jet propagation

c) 16 passes through a Herriott type optics

In the parallel setup (a) the microwave radiation beam has an almost parallel alignment with the molecular beam. Thus, the incident (opposite to the direction of jet propagation) and the reflected beam (parallel to the direction of jet propagation) lead to two Doppler-shifted components of the transitions. The total absorption of the transition is distributed to two peaks in the spectrum which neither necessarily have the same intensity nor the same shift relative to the center frequency. The frequency positions of the two components strongly depend on the relative alignment and frequency calibration is always required. The absorption path length is approximately 15 *cm* for each pass due to the length of the cone-shaped jet produced by a pinhole nozzle. The molecules *HCN* and *HNC* have been observed with SuJeSTA using this optical setup. A typical spectrum is shown in Fig. 3.6. Unfortunately, this layout has proven not to be applicable for the investigation of C_3H. An explanation for this might be the short absorption path of only 15 *cm* which has been improved in the course of this work. But it seems more likely that the pinhole discharge nozzle is not an effective source for the production of C_3H (see Section 3.1.1).

In setup (b) the microwave beam probes the molecular jet approximately 5 *cm* downstream and almost perpendicular to the direction of jet propagation. By this means, line shifts due to the Doppler effect are minimized. Nevertheless, periodical frequency calibrations are useful. The absorption path length of this setup is given by the width of the molecular beam (slit nozzle: $\sim$5 *cm*, pinhole nozzle: $\sim$3 *cm* each pass) times the number of passes. Employing a 6 passes optics, the absorption path is enlarged to 30 *cm* with the slit nozzle and to 18 *cm* with the pinhole nozzle. The optics (see Fig. 3.10) consist of a concave mirror (focal length 7.5 *cm*) and of a plain mirror at a distance of 7.5 *cm*. This enhancement leads to a significant improvement of the signal to noise ratio compared to two passes. Setup (b) in combination with a slit discharge nozzle has been used for the detection of C_3H and CO^+, using high power BWOs as radiation source.

Using a low power superlattice device as source for the probing radiation, the number of passes has to be increased. This is realized by a Herriott type multipath optics [52] (setup (c)) consisting of two concave mirrors of which one has a recess for the incoming and outgoing beam (see Fig. 3.10). An elliptical pattern of *n* spots arises on each mirror. The number of reflections *n* depends on the distance *d* between the mirrors and the their focal lengths *f*:

$$\frac{d}{f} = 2\left[1 - cos\left(\frac{\varphi}{2}\right)\right] \tag{3.5}$$

where φ is the angle between two consecutive reflections on each mirror with the following relation [53]:

$$n\varphi = 2\pi k \quad with \quad k = 1,2,...,n \tag{3.6}$$

Here *k* is equal to the number of circulations on the mirrors. An important feature of a Herriott type optics is that the reflected beam has the same Gausian and geometric parameters as the incident beam.

The two concave mirrors with a focal length of 15 *cm* at a distance of less than **30** *cm* were aligned to produce 8 reflections on each mirror which results in a total of 16 passes. Thus, the absorption path length is increased to approximately 80 *cm* with the slit nozzle and 48 *cm* with the pinhole nozzle. The mirrors are polished to optical quality to allow He-Ne-laser adjustment of the optical system. The microwave beam waist is focused to the center between the two mirrors where it coincides with the zone of silence of the supersonic molecular jet.

In the configurations (b) and (c) the horizontal position of the supersonic jet is adjustable by means of a motor to optimize the alignment of the molecular jet relative to that of the microwave beam from outside the vacuum chamber.

3.1.3   Detector
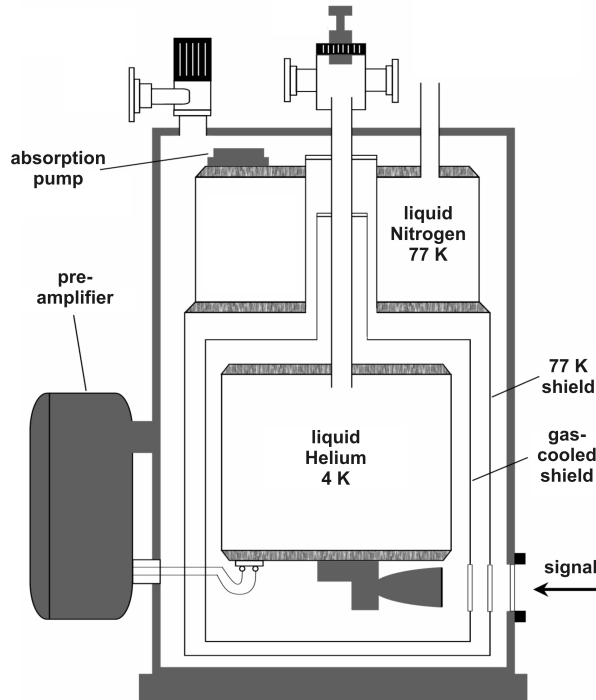
Figure 3.11: Schematic diagram of the *InSb* Hot Electron Bolometer (HEB): The *InSb*-chip is cooled by liquid helium to a temperature of 4.2 *K*. The 4 *K* stage is protected by a helium gas-cooled shield and a liquid nitrogen cooled shield (77 *K*) against thermal radiation. High vacuum of less than 10^{-5} *mbar* is needed for thermal isolation of the system.

A broadband helium cooled *InSb* Hot Electron Bolometer (HEB), with a maximum of sensitivity at a frequency around 600 *GHz*, has been used to record all spectra in the course of this work. A schematic drawing of the

detector system is shown in Fig. 3.11. The key part is the *InSb*-chip where the incedent microwave radiation is absorbed by electrons, at which their average temperature is increased compared to that of the chip. The resulting change in conductivity is commensurate to the intensity of the radiation. The relaxation time is approximately 1 *μs* which is sufficiently short to allow a frequency modulation of the radiation source with up to 500 *kHz* (see Section 3.1.4). The signal is processed in a pre-amplifier for data acquisition. The incident radiation enters the detector via a Teflon window.

To keep the noise level low it is necessary to hold the *InSb*-chip on a temperature of 4 *K*. Therefore, the chip is connected to a liquid helium cooled plate. The 4 *K* stage is protected by a helium gas-cooled shield and a liquid nitrogen cooled shield (77 *K*) against thermal radiation. High vacuum of less than 10^{-5} *mbar* is needed for thermal isolation of the system.

3.1.4   Signal Processing

Measurements at the Supersonic Jet Spectrometer for Terahertz Applications as well as at the Cologne Terahertz Spectrometer (see Section 3.2) are performed in a $2f$-modulation mode which increases the signal to noise ratio significantly at cost of the line width. The radiation source of SuJeSTA is usually operated with a modulation frequency between 35 and 45 *kHz* to achieve an effective modulation during the short gas pulse of approximately 200 *μs*. Thus, 8 cycles per gas pulse are obtained. The total amplitude of the modulation ranges between 400 and 2000 *kHz*, depending on the expected intensity and line width of a transition. The optimal value of the modulation amplitude is in the range of the half width at half maximum of a transition line. Subsequently, a digital lock-in amplifier (DLI) demodulates the signal and relays it to a computer. The recorded line shows the second derivative of the original signal due to the $2f$-modulation.

In case of SuJeSTA, a second on-off modulation is possible due to the pulsed molecular jet. In fact, microwave radiation is absorbed only for short time by the molecules contained in the 200–250 *μs* gas pulse. Since the repetition rate is 50 *Hz* there remains a time span of almost 20 *ms* where the radiation passes the absorption cell unimpeded. This time or part of it can be used to integrate the background signal to be subtracted from the "on"-signal. SuJeSTA is principally baseline limited due to standing wave etalon effects which are eliminated by the on-off modulation.

In the course of this thesis a special software was developed for the requirements of a pulsed experiment. It enables the recording of the spectra and allows full control of the external devices, i.e. synthesizer and digital lock-in amplifier. By means of the program "SuJeSTA-Control" the most important parameters of the spectrometer are accessible via a graphical user interface:

- center frequency

- frequency span and increment

- modulation amplitude and frequency

- time frame for signal integration and background subtraction

- number of scans and averages

Additional settings are accessible in submenus. A screen shot of the graphical user interface of the "SuJeSTA-Control" program is shown at the top part of Fig. 3.12.

The external devices are controlled via GPIB-bus. For data acquisition a fast eight channel AD-converter card with a sampling rate of up to 100 kHz is used. In the following the method of recording a spectrum is described:

Starting a measurement the modulation parameters are sent to the lock-in amplifier and the synthesizer is set to the start frequency which is calculated by:

$$f_{synthesizer} = \frac{f_{center} - \frac{f_{span}}{2} \pm 350 \; MHz}{N_{harmonic}}$$

$$\Rightarrow f_{start} = f_{center} - \frac{f_{span}}{2} \tag{3.7}$$

Here $N_{harmonic}$ is the appropriate integer harmonic for the frequency of the synthesizer to be mixed with the BWO radiation to an intermediate frequency of 350 MHz, where $\pm$ stands for the upper or lower sideband (see Section 3.3.2). f_{center} is the desired center frequency and f_{span} is the width of a scan. An external pulse generator, synchronized to the AC-line frequency, generates a trigger to start the data acquisition. With the same trigger the valve is forced to open. An optional second trigger some hundred microseconds later lights the discharge (see Section 3.1.1). The data acquisition stops when both intervals, i.e. signal integration and background subtraction, are completed. The mean background level is subtracted from the mean signal level. This procedure is repeated m times as specified by the user in the "Averages each frequency"-field and the m values are averaged. Subsequently, the synthesizer is set to the next frequency by adding or subtracting:

$$f_{step} = \frac{f_{increment}}{N_{harmonic}} \tag{3.8}$$

After a time of 100 ms to allow the synthesizer to lock on the new frequency, the data acquisition starts afresh. When the frequency span is completely covered a subsequent scan in the opposite direction follows until the maximum number of scans is reached or the user aborts the process. During the scanning process, an online visualization of the spectrum shows the recorded signal. This facilitates the decision wether the experimental parameters have to be changed in order to yield optimal results. An exemplary spectrum of the first of four scans of a C_3H transition is shown at the lower part of Fig. 3.12.

The additional scans result in an averaged spectrum which is saved in ASCII code as a list of intensities versus frequencies. In addition, a parameter file provides all information on the measurement, consisting of center frequency, span, modulation parameters, time windows, and user defined comments.
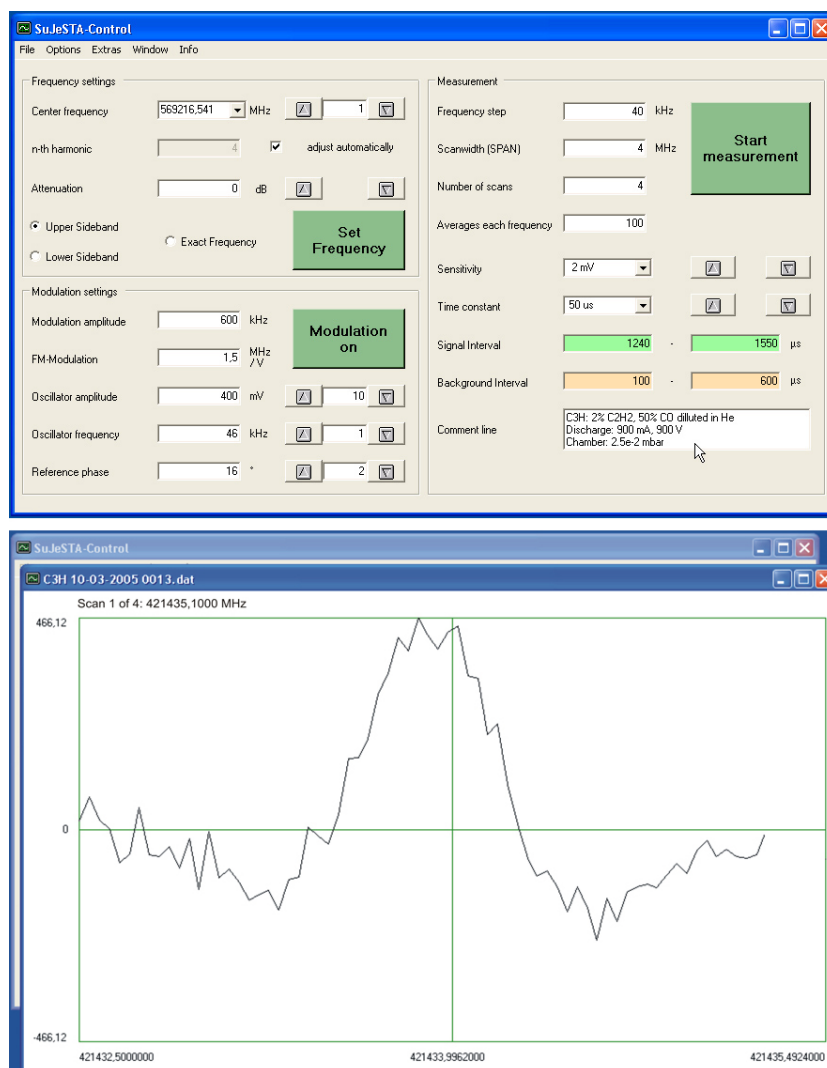
Figure 3.12: Top: Screen shot of the graphical user interface of the software, controlling the SuJeSTA spectrometer. The spectra are recorded by means of a fast eight channel AD-converter card. The synthesizer and lock-in amplifier are controlled via GPIB-bus. All parameters necessary for measurements are accessible at the graphical user interface. Additional settings are accessible in submenus. Lower: Screen shot of a C_3H measurement with SuJeSTA-Control. The first of four scans is shown which is going to be improved by further scans. The current frequency position and the number of scans are displayed at the top of the window.

3.1.5   Sensitivity of SuJeSTA

The sensitivity of the new spectrometer has been analyzed in this work by means of the $J = 3 \leftarrow 2$ pure rotational transitions of $^{13}C^{16}O$ and $^{12}C^{18}O$ at approximately 330 *GHz*. The signal to noise ratio (SNR) of the lines shown in Fig. 3.13 has been estimated to be 175 for $^{13}C^{16}O$ and 35 for $^{12}C^{18}O$. The ratio of both SNRs is 5 which is about the same as the ratio of the relative abundances of the two isotopomers (1.07 % and 0.205 %). A superlattice device, pumped by a 3 *mm* KVARZ-synthesizer and operated at the third harmonic, served as radiation source.
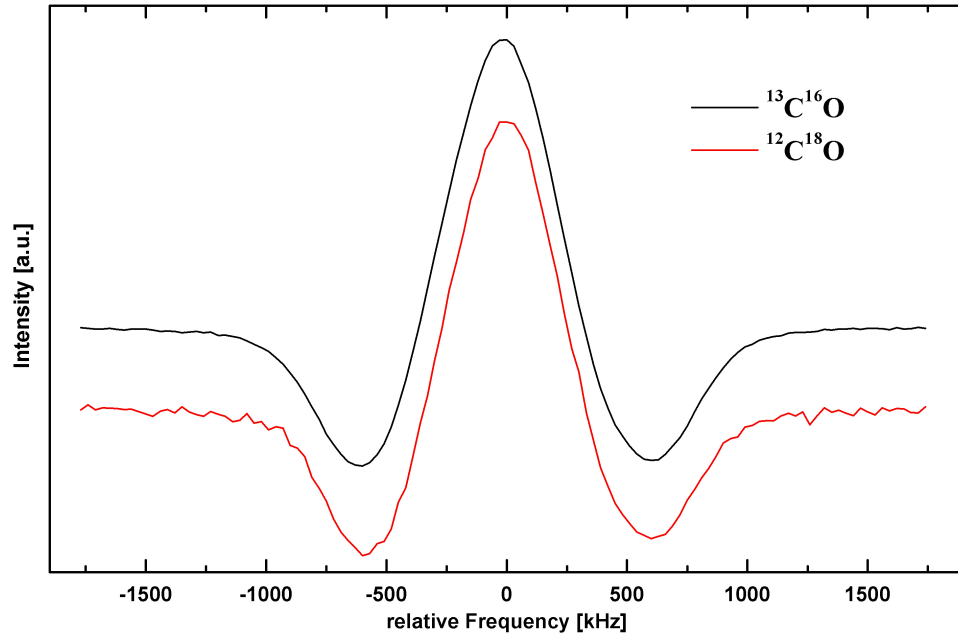
Figure 3.13: $J = 3 \leftarrow 2$ pure rotational transitions of $^{13}C^{16}O$ (black) and $^{12}C^{18}O$ (red). The maximum intensity of both lines is scaled to 1. The center position of $^{13}C^{16}O$ line is located at 330587.9 *MHz* and shows signal-to-noise ratio (SNR) of 175. The $^{12}C^{18}O$ line is located at 329330.6 *MHz* and has a SNR of 35. The ratio of both SNRs is approximately 5 which is equivalent to the ratio of the relative abundances of the two isotopomers. Both lines have been recorded with the following parameters: 100 averages each frequency-position, 30 *kHz* frequency steps, $2f$-modulation with a frequency of 36.13371 *kHz* and amplitude of 1350 *kHz*, $1.7 \cdot 10^{-2}$ *mbar* background pressure, 1:5 CO-Ar-mixture at 1.5 *bar*, 50 *Hz* repetition rate. The spectra have been recorded with the Herriott type setup using a superlattice device operated at the third harmonic as radiation source.

Assuming approximately $7 \cdot 10^{18}$ particles per gas pulse [49] of a $1 : 5$ *CO–Ar* mixture the total amount of $^{13}C^{16}O$ and $^{12}C^{18}O$ molecules can be

estimated to be $\sim 1.5 \cdot 10^{16}$ and $\sim 2.9 \cdot 10^{15}$, respectively. Defining 3 as the lower limit of the SNR for a detectable line one calculates a minimum of $\sim 2.5 \cdot 10^{14}$ molecules in the whole volume probed by the radiation beam. The above mentioned transitions have been recorded with the Herriott type optics and the slit nozzle which results in a total absorption path length of 80 *cm*. Thus, one derives a total absorption volume of approximately 250 *cm*^{3}, assuming that the radiation beam has a mean diameter of 2 *cm* in the observed region. From this a lower limit for the column density of *CO* molecules ($\mu = 0.1105$ *D*) of 10^{12} $\frac{molecules}{cm^2}$ is determined to detect the $J = 3 \leftarrow 2$ transition.

These results can be compared to a common "cell-experiment": The Cologne terahertz spectrometer (see next Section) has been used with an absorption cell of 3 *m* in length containing *CO* at partial pressure of $2 \cdot 10^{-2}$ *mbar* to record the above mentioned transition. As with SuJeSTA a $2f$-modulated superlattice device has been used as radiation source. To compare the signal to noise ratio of this setup with the supersonic expansion setup, one has to take into account that the *CO* gas in the cell is at ambient temperature. Thus, the $J = 3 \leftarrow 2$ transition is 36 times weaker compared to the 40 *K* gas (value taken from the CDMS [13]). Under this assumption a lower limit for the column density of approximately $4 \cdot 10^{12}$ $\frac{molecules}{cm^2}$ has been determined to achieve a signal to noise ratio of 3. This result is of the same order of magnitude as the column density obtained for SuJeSTA and both spectrometers have comparable sensitivities.
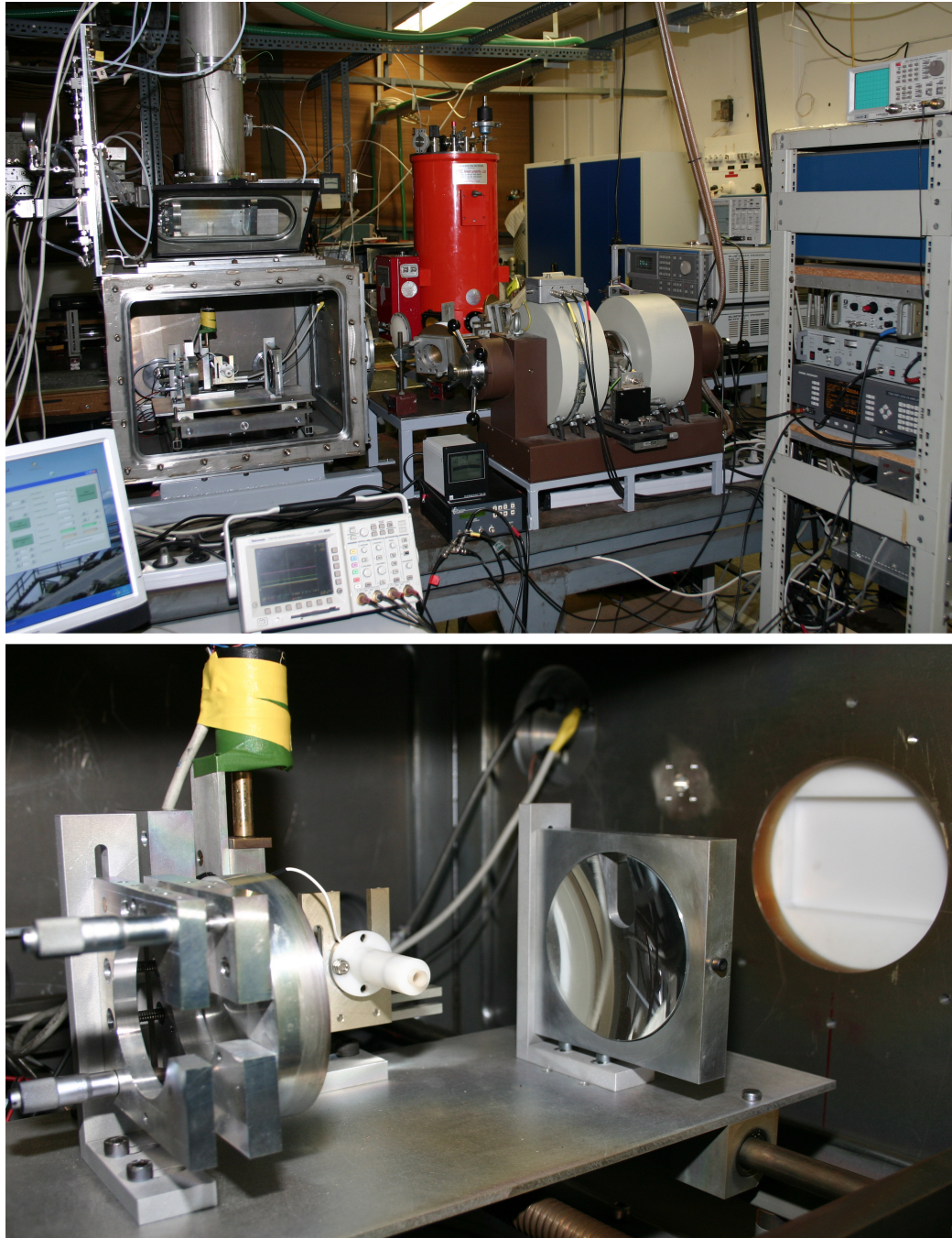
Figure 3.14: Pictures of the SuJeSTA-Experiment: Top (from the left to the right): The vacuum chamber, the detector, the magnets with BWO, the KVARZ synthesizer, and further electronic devices. Lower: Heriott type optics with pinhole discharge nozzle; the radiation beam enters from the right hand side - through the HDPE-window.

3.2   Cologne Terahertz Spectrometer with Evaporation Cell
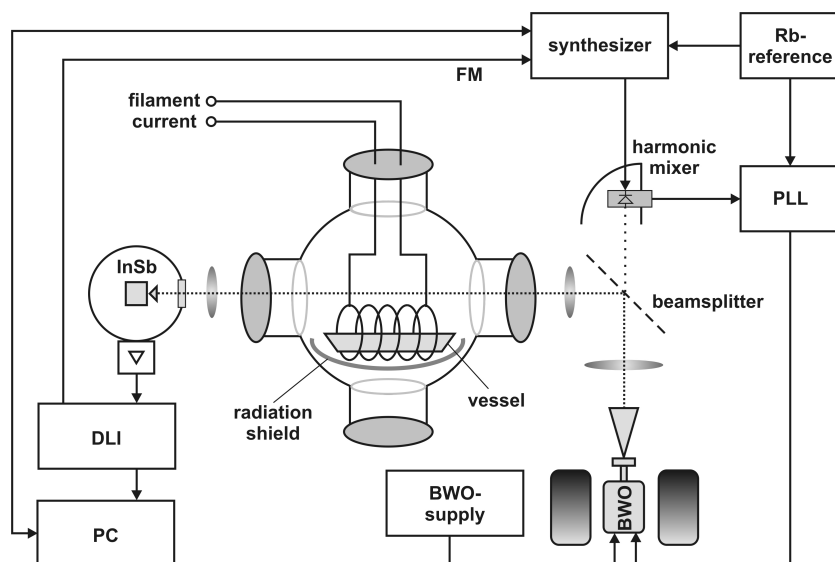
Figure 3.15: Experimental setup of the Cologne Terahertz Spectrometer. Backward Wave Oscillators (BWOs) are used as radiation sources. The signal is detected on a liquid helium cooled *InSb*-Hot Electron Bolometer. The *KCl* molecules are evaporated inside the absorption cell.

The Cologne Terahertz Spectrometer has been thoroughly described in many publications, for example Winnewisser *et al.* [1], Caris *et al.* [2], [26], and Klapper [10]. Fig. 3.15 shows a schematic diagram of the Cologne Terahertz Spectrometer with evaporation cell. The key elements are the BWO, the Phase Lock Loop (PLL), the absorption cell, and the detector. The phase stabilized radiation from the BWO intersects the *KCl*-vapor very close to the ceramic vessel inside the absorption cell (see Section 3.2.1). The *InSb* Hot Electron Bolometer detects the signal. A Digital Lock-In amplifier (DLI) demodulates the $2f$-modulated signal (see Section 3.1.4) and relays it to a PC for recording. Typical values for the $2f$-modulation are 10–20 *kHz* of modulation frequency and 600–1000 *kHz* of modulation amplitude.

3.2.1   Evaporation Cell

It is a challenging problem to evaporate a solid substance, which has a low affinity to change to the gas phase, and to provide it for spectroscopy. It has to be guaranteed that a consistent flow of molecules within the absorption path is produced, while the amount of particles is essential for reasonable spectroscopic results. Therefore, a special cell [26] was designed, used for measurements on *KCl* in the course of this thesis and on *NaCl* in a previous work [2]. A schematic diagram is shown in Fig. 3.16.
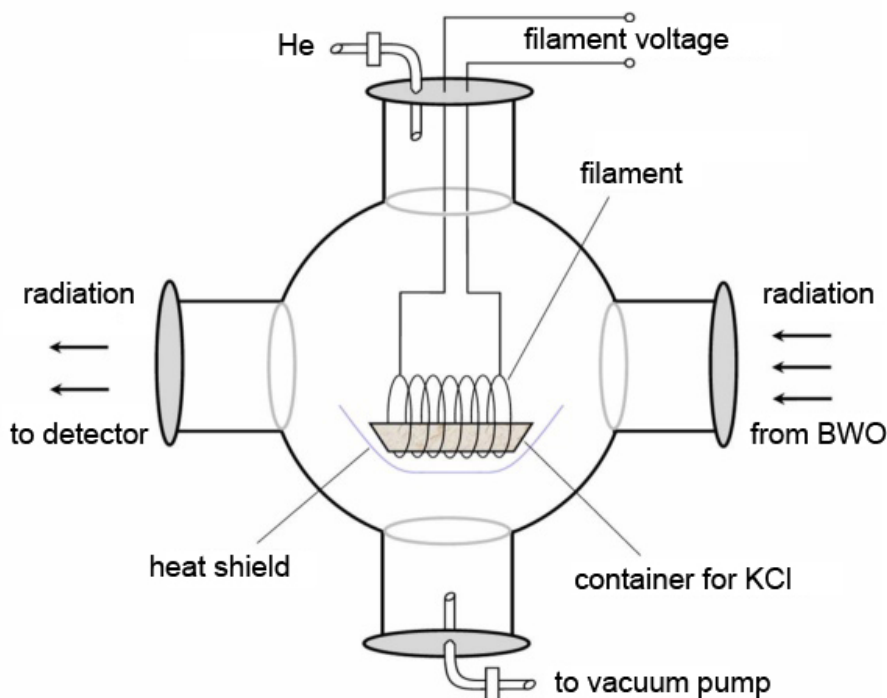
Figure 3.16: Schematic diagram of the Evaporation Cell.

The boiling temperature of the substances analyzed with this setup ranges between 1407 °C (*KCl*) and 1465 °C (*NaCl*). Thus, a special heating system had to be applied to the absorption cell. It consists of a filament encircling a ceramic vessel, an approximately 5 *cm* long, hollow container used to hold the substance. By this means, the vessel could be heated up to the required temperature. In addition, a radiation shield, consisting of a steel plate, was installed which surrounds the filament to protect the glass cell against the thermal radiation and to reflect it back into the vessel. A small slit at the upper side of this cylindrical shield allowed the evaporated substance to enter the region of the probing microwave beam. This construction was positioned in the center of a spherical cell which offered the advantage of easily positioning the heater very tightly beneath the microwave beam but with sufficient distance to the walls of the glass sphere.

The operational conditions of the sample cell were provided by applying helium as buffer gas, in order to reduce the deposition of *KCl* molecules on the cell walls. The partial pressure of *He* in the cell was held at 100 *μbar* to maintain a maximum of absorption signal and to keep the line shape as narrow as possible. The substance content of a few gram in the vessel allowed 3–4 hours of continuous measurements.

3.3   Terahertz Radiation Sources

The measurements within the scope of this thesis have been carried out in the terahertz domain. This part of the electromagnetic spectrum still is a technically challenging area and sources for terahertz radiation are not very prevalent (see Fig 3.17). This has to be ascertained particularly with regard to the region between 1 and 5 THz (terahertz-gap). Existing commercial devices, such as microwave synthesizers or Gunn oscillators are limited to approximately 0.15 THz. The efficiency of frequency multiplying decreases rapidly with higher harmonics and frequencies, respectively. Cascading multiplier chains are not suited to provide sufficient output power for spectroscopic applications. Therefore, monochromatic radiation with frequencies beyond 1 THz was obtained rarely until very recently.
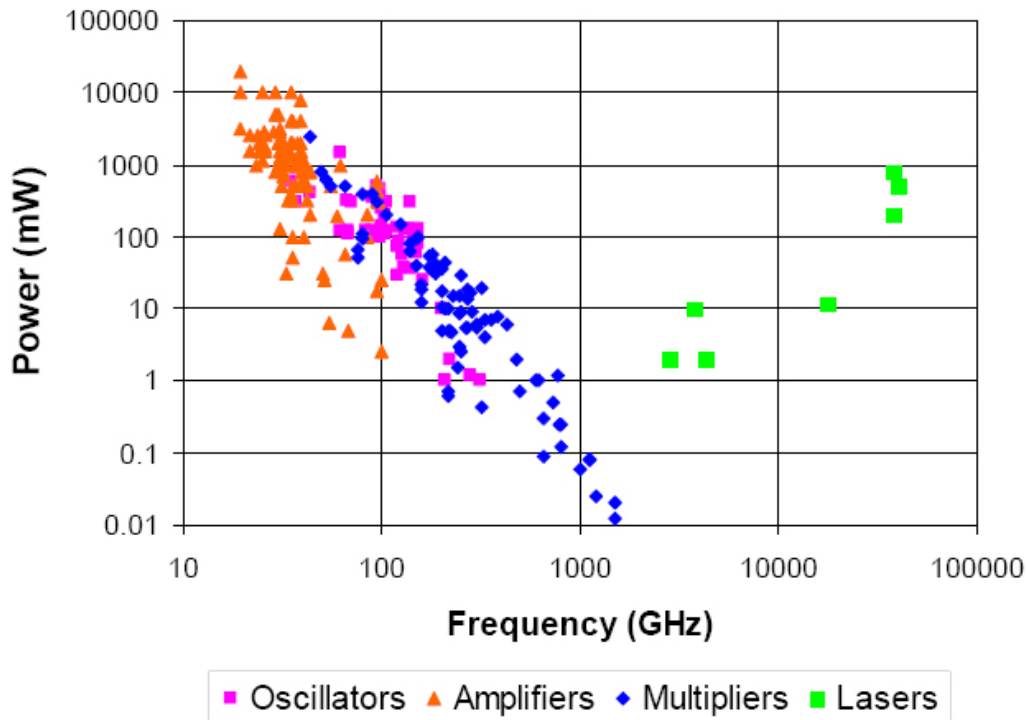
Figure 3.17: Terahertz sources and their output power [54].

In the following a backward wave oscillator and a superlattice device which have been employed in this work are described. For both types of radiation sources the technique of phase stabilization has been applied to achieve highest frequency accuracy.

3.3.1 Backward Wave Oscillator (BWO) and Superlattice Electronic Device (SLED)

The terahertz regime has disclosed some of its secrets due to Russian Backward Wave Oscillators (BWOs), fabricated by the ISTOK company. They are a well established monochromatic source for millimeter and submillimeter radiation at the Cologne laboratories. The available BWOs cover in bands a frequency range of 53 to 1250 *GHz* nearly without interruption. Its output power ranges between several tens of *mW* and a few *mW* at highest frequencies which is sufficient for absorption spectroscopy. In combination with phase stabilization BWOs are a sophisticated terahertz source with high frequency accuracy and large tunability. The measurements in this work have been carried out with a single BWO-tube in the region from 430 to 625 *GHz* (C_3H, CO^+) and with several tubes ranging from 170 to 930 *GHz* (*KCl*). The principle of BWOs is briefly explained in the following; detailed information is given elsewhere (e.g. in the textbook of Gewartowski and Watson [55] or in [56], [57], [58]).

A bundled electron beam is guided along a slow wave structure (see fig. 3.18). Thereby, the electrons are accelerated and decelerated periodically. Thus, an electromagnetic beam is produced, which travels in opposite direction to the propagation of the electrons ($\Rightarrow$ *Backward* Wave Oscillator). The radiation exits the tube by a waveguide and can be used for spectroscopic applications.
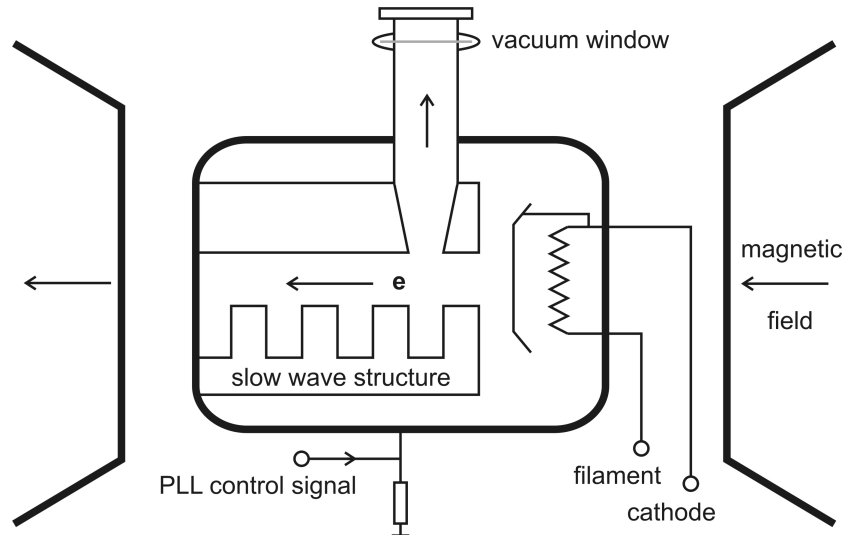
Figure 3.18: Schematic diagram of Backward Wave Oscillator: Electrons with a speed up to $3 \cdot 10^7 \frac{m}{s}$ are accelerated and decelerated by a slow wave structure. The generated electromagnetic radiation (53 to 1250 *GHz*) travels in the opposite direction and is coupled out into a waveguide. The electron beam is bundled by a magnetic field of 1.2 *T*.

The frequency of the produced radiation depends on the parameters of

the slow wave structure, which is predetermined by the design of the BWO - each is constructed for a special center frequency. By varying the the speed of the electrons via the accelerating voltage the frequency of the output radiation is tuned. An adjustment of approximately ± 20 % of the center frequency is typical for BWO tubes. The cathode voltage ranges between 1.5 and 6 *kV* leading to an electron current of 10–20 *mA*. The filament current equals values of 1.2–1.5 *A*. Electromagnets surrounding the BWO generate a magnetic field of up to 1.2 *T*, to bundle the electron beam. The output power usually ranges between 0.5 and 10 *mW* and can equal up to 100 *mW* at special high power tubes.

While common frequency multipliers, such as Schottky diodes, have been used in the past to generate terahertz radiation, the Superlattice Electronic Devices (SLEDs) are a very recent Russian development. Pumped by an appropriate frequency stabilized radiation in the millimeter and submillimeter domain, they emit odd harmonics of the input frequency. In combination with BWOs or synthesizers, it has successfully been introduced as radiation source for spectroscopical applications beyond 1 *THz* (see e.g. Endres [24]). The superlattice electronic devices consist of a periodic sequence of semiconductor layers of a few monolayers. The crucial factor for frequency multiplication is the high non-linearity in their current-voltage characteristic. The superlattice produces only the odd harmonics of the input frequency $v_e = (2n+1)v_i$ with $n = 1, 2,...$ due to the antisymmetry of the IV-curve. Further details on superlattice devices are given in the works of Scheuerer *etal.* [59], Wacker *etal.* [60], Tsu *etal.* [61], and Kazarino *etal.* [62].

3.3.2 Phase Stabilizing System

The frequency of a free-running BWO can deviate from the desired frequency by several *MHz* on a timescale of minutes. This is by far more than the precision of a high resolution spectrometer can cope with. Thus, a phase stabilization has to be applied to all BWO-based experiments if high resolution is required. The free running mode is reasonable if precision plays a minor role, for instance in large overview scans (see Fig. 3.2).

For phase stabilization, one part of the microwave radiation, usually 10–20 %, is coupled onto a harmonic mixer device via a beamsplitter (see Fig. 3.1). The BWO radiation is mixed with the signal of a Local Oscillator (LO) on a Schottky diode. The LO-signal emanates from a synthesizer (KVARZ, Russia) which is available in a 2 *mm* (118–178 *GHz*), a 3 *mm* (78–118 *GHz*), and a 4 *mm* (58–78 *GHz*) version. The harmonic mixer generates the frequency harmonics of the two input frequencies, resulting in several Intermediate Frequencies (IFs):

$$f_{IF} = \pm m \cdot f_{BWO} \pm n \cdot f_{Synth} \qquad (3.9)$$

If *n* is chosen properly an intermediate frequency of 350 *MHz* is generated which is subsequently relayed to the Phase Lock Loop (PLL). The PLL provides a control voltage which is proportional to the phase difference between

the IF and the frequency multiplied signal of a *Rb*-reference (10 *MHz*). The synthesizer is also connected to the same frequency standard. The control voltage is applied to the BWO which is thereby stabilized in frequency to approximately 1 *Hz* for a sufficient time.

4

Theoretical Considerations

In the experimental part of this work the spectra of three classes of linear molecules have been investigated: diatomic neutrals, ions, and polyatomic radicals. The spectroscopic data is used to derive molecular parameters in the framework of a quantum mechanical model. In this chapter the theoretical fundamentals for the analysis of rotational and ro-vibrational spectra will be presented. Furthermore, Dunham's isotopically invariant approach for diatomic molecules will be introduced [63], [64]. Concerning radicals, the ro-vibrational motion of a molecule is not the only interaction but also electronic and magnetic effects appear, such as fine and hyperfine structure. Other interesting features, such as Renner-Teller and Coriolis coupling, can also affect the energy levels. The aim is to derive an effective Hamiltonian which describes the spectra of the molecules investigated in this work. The Hamiltonian provides the energy in form of the eigenvalues by solving the time independent Schrödinger equation.

The Hamiltonian presented in Equation 4.1 consists of seven terms: $\hat{H}_{rot}$ (rotational motion), $\hat{H}_{vib}$ (vibrational motion), $\hat{H}_{FS}$ (fine structure), $\hat{H}_{HFS}$ (hyperfine structure), $\hat{H}_{l-doub}$ (l-type doubling), $\hat{H}_{\Lambda-doub}$ (Λ-type doubling), and $\hat{H}_{RT}$ (Renner-Teller effect). The effects leading to these terms are described in detail in the following sections.

$$\hat{H}_{eff} = \hat{H}_{vib} + \hat{H}_{rot} + \hat{H}_{FS} + \hat{H}_{HFS} + \hat{H}_{l-doub} + \hat{H}_{\Lambda-doub} + \hat{H}_{RT} \qquad (4.1)$$

Continuative literature concerning the spectra of molecules are the standard text books of G. Herzberg [65], [66], C. H. Townes and A. L. Schawlow [67], W. Gordy and R. L. Cook [68], and P. F. Bernath [69].

4.1   Pure Rotational Spectra of Linear Molecules

The rigid rotor is the simplest approach to describe the pure rotational motion of a linear molecule. In this connection "rigid" means that the distance

of the nuclei is independent of the molecule's motion. The spectrum of such rigid rotors consist of several equidistant lines with characteristic temperature dependent intensity distribution. The Hamiltonian for this motion is provided by quantum mechanics as follows:

$$\hat{H}_{rot} = \frac{\hat{J}^2}{2\Theta} = \frac{\hbar^2}{2\Theta}J(J+1) \tag{4.2}$$

Where $\hat{J}$ is the operator of the angular momentum, J is the rotational quantum number, and Θ is the moment of inertia. The energy of a rotational state with quantum number J in units of Joule can be expressed by means of the rotational constant B:

$$E_J = \frac{\hbar c}{2\pi}B \cdot J(J+1) \qquad [Joule] \tag{4.3}$$

Where B in units of wavenumbers is defined as:

$$B = \frac{\hbar}{4\pi c\Theta} \cdot 10^{-2} \qquad [cm^{-1}] \tag{4.4}$$

It is also customary to express the energy and B in units of MHz. In this case, B can be written as:

$$B = \frac{\hbar}{4\pi\Theta} \cdot 10^{-6} \qquad [MHz] \tag{4.5}$$

and the energy is simply:

$$E_J = B \cdot J(J+1) \qquad [MHz] \tag{4.6}$$

In the following, all parameters and energies will be given in MHz, if not denoted otherwise.

The energy of a rotational transition from the level designated by $J+1$ to the next lower level J ($\nu_{(J+1)\leftarrow J}$) is calculated by subtracting E_J from E_{J+1} and results in $2B(J+1)$. Since the selection rules for linear molecules (disregarding the effects of nuclear spin) only allow transitions with $\Delta J = \pm 1$, lines of a linear rigid rotor are equally spaced with $2B$.

A closer look at the spectra shows that the lines are not equidistant but rather the spacing decreases with increasing J. This is due to an effect called centrifugal distortion. That means, with the molecule rotating faster, the distance of the nuclei is enlarged and so is the moment of inertia. This results in higher order terms for the rotational energy of a level J (see e.g. [65], [69]):

$$E_J = B \cdot J(J+1) - D \cdot J^2(J+1)^2 + H \cdot J^3(J+1)^3 + ... \tag{4.7}$$

For determination of the centrifugal distortion constants D and H it might be necessary to observe transitions with very high J values. The spacing of the lines of the non-rigid rotor are calculated to be:

$$\Delta\nu_{(J+1)\leftarrow J} = 2B(J+1) - 4D(J+1)^3 + ... \tag{4.8}$$

The Hamiltonian for the rotational motion can be expressed as:

$$\hat{H}_{rot} = B\hat{J}^2 - D\hat{J}^2 \cdot \hat{J}^2 \qquad (4.9)$$

where $\hat{J}$ is the operator of the angular momentum with eigenvalues J. From this follows: $\hat{J}^2 \propto J(J+1)$.

4.2 Rotational-Vibrational Spectra of Diatomic Molecules

The low resolution vibrational spectrum of a diatomic molecule consists only of one line at the frequency ν and its overtones at 2ν, 3ν, etc., since a diatomic molecule has only one degree of freedom for vibrational motion along the axis of symmetry. A characteristic substructure due to rotational-vibrational coupling becomes visible with sufficient spectral resolution.

4.2.1 Classical Approach

The pure vibrational spectral lines of a diatomic molecule arise from the energy levels of an inharmonic oscillator. The potential of such oscillator is called Morse potential and is given by the equation:

$$V = E_{dis}\left(1 - e^{-a(R-R_e)}\right)^2 \qquad with \qquad a = \hat{\omega}_e\sqrt{\frac{m_r}{2E_{dis}}} \qquad (4.10)$$

where E_{dis} is the dissociation energy, m_r is the reduced mass of the molecule and $\hat{\omega}_e$ is the frequency of the harmonic oscillator. The quantum mechanical treatment results in the following expression for the vibrational energy levels depending on the vibrational quantum number v:

$$E_v = \hbar\hat{\omega}_e\left(v + \frac{1}{2}\right) - \hbar x_e\hat{\omega}_e\left(v + \frac{1}{2}\right)^2 + ... \qquad [Joule] \qquad (4.11)$$

Also the vibrational energy can be expressed in MHz:

$$E_v = \omega_e\left(v + \frac{1}{2}\right) - x_e\omega_e\left(v + \frac{1}{2}\right)^2 + ... \qquad with \qquad \omega_e = \frac{\hat{\omega}_e}{\hbar} \cdot 10^{-6} \qquad (4.12)$$

$x_e = \frac{\hbar\omega_e}{4E_{diss}}$ is the inharmonic parameter which is usually of the order 10^{-2}.

Since the vibrational motion is about a factor of thousand faster than the rotational one, the average distance of the nuclei is sufficient for determination of the moment of inertia Θ. Within an inharmonic oscillator model, the averaged distance and consequently Θ increase with the vibrational quantum number v. The result is a change of the rotational energy levels and the rotational parameters (B, D, etc.), respectively. Thus the coupling between rotational and vibrational motion has to be included by vibrational distortion

terms. The vibrational dependent rotational parameters B_v and D_v usually decrease with increasing v. The following equations allow for this fact:

$$B_v = B_e - \alpha \left(v + \frac{1}{2} \right) + \gamma \left(v + \frac{1}{2} \right)^2 - \dots \tag{4.13}$$

$$D_v = D_e + \beta \left(v + \frac{1}{2} \right) - \delta \left(v + \frac{1}{2} \right)^2 + \dots \tag{4.14}$$

with B_e and D_e being the rotational constants in a hypothetical vibration-free state. α, γ, β, and δ are the vibrational distortion parameters. Typically the aforementioned constants are ordered as follows: $|\delta| \ll |\beta| \ll |D_e| \ll |\gamma| \ll |\alpha| \ll |B_e|$

The rotational vibrational energy levels of a diatomic molecule are calculated with the following expression:

$$\begin{aligned}
E_{v,J} = {} & \omega_e \left(v + \frac{1}{2} \right) - x_e \omega_e \left(v + \frac{1}{2} \right)^2 \\
& + \left[B_e - \alpha \left(v + \frac{1}{2} \right) + \gamma \left(v + \frac{1}{2} \right)^2 \right] J(J+1) \\
& - \left[D_e - \beta \left(v + \frac{1}{2} \right) + \delta \left(v + \frac{1}{2} \right)^2 \right] J^2(J+1)^2
\end{aligned} \tag{4.15}$$

The rovibrational spectrum generally consist of three branches (P, Q, R). The P-branch contains the lines of transitions with $\Delta v = 1$ and $\Delta J = -1$, the R-branch designates the lines with $\Delta v = 1$ and $\Delta J = +1$, and the lines of the Q-branch stem from transitions with $\Delta J = 0$. The spacing of the lines in the P-branch increases with J and the lines of the R-branch converge with increasing J due to the correction terms of eq. 4.15.
For pure rotational transition from a level J to $(J+1)$ one derives from eq. 4.15 the energy:

$$\begin{aligned}
\nu_{(J+1) \leftarrow J} = {} & \left[2B_e - 2\alpha \left(v + \frac{1}{2} \right) + 2\gamma \left(v + \frac{1}{2} \right)^2 \right] (J+1) \\
& - \left[4D_e - 4\beta \left(v + \frac{1}{2} \right) + 4\delta \left(v + \frac{1}{2} \right)^2 \right] (J+1)^3
\end{aligned} \tag{4.16}$$

4.2.2   Dunham's Approach

Within the scope of this work the diatomic species (KCl, CO^+) have been analyzed in an isotopically invariant way. The derived set of mass independent molecular parameters is valid for all isotopomers of a molecule. Two points simplify the analysis of a diatomic molecule: The potential is a simple function of the bond length and only one vibrational mode (stretching

vibration) occurs. The best approach to this problem is a theoretical model which was introduced by Dunham in 1932 [63], [64]. He made use of the Born-Oppenheimer approximation which was first introduced by M. Born and R. Oppenheimer in 1927 [70]. In this assumption, the electronic motion and the nuclear motion in molecules can be separated:

$$\Psi_{mol}\left(\vec{r}_i, \vec{R}_j\right) = \Psi_{el}\left(\vec{r}_i, \vec{R}_j\right) \cdot \Psi_{nuc}\left(\vec{R}_j\right) \tag{4.17}$$

The electronic wavefunction depends only on the nuclear positions rather than on their velocities, because nuclear motion is much slower than electron motion. Thus, the electrons move in a quasi static nuclear potential. Contrariwise, the nuclei move in an average electronic potential. In particular, the electronic potential is assumed to be independent of the nuclei's masses and their motion and thus is the same for each isotopomer [71]. The strict validity of the Born-Oppenheimer approximation reveals an independency of bond length and isotopomeric composition for diatomic molecules. Thus the moment of inertia changes for different isotopomers, while electronic potential and bond length are not affected.

Dunham calculated the energy levels of a vibrating rotor by expanding the potential V in a power series, under the assumption of the validity of the Born-Oppenheimer approximation:

$$\begin{aligned} V(\rho) =& a_0\rho^2\left(1 + a_1\rho + a_2\rho^2 + a_3\rho^3 + ...\right) \\ &+ B_e J(J+1)\left(1 - 2\rho + 3\rho^2 - 4\rho^3 + ...\right) \end{aligned} \tag{4.18}$$

where $\rho = \frac{r - r_e}{r_e}$ and r_e is the distance of the two nuclei in the minimum of the potential. The second summand mentions the rotational influence on the effective potential. The constants a_i are potential coefficients, B_e is the rotational constant, and J the rotational quantum number. For the energy levels one derives the following expression:

$$E_{v,J} = \sum_{i,j} Y_{ij} \left(v + \frac{1}{2}\right)^i J^j(J+1)^j \tag{4.19}$$

Y_{ij} are the Dunham-Coefficients, v and J are the quantum numbers of vibration and rotation, respectively. The Dunham constants can be approximated by the conventional rovibrational quantum numbers as follows:

$$\begin{array}{lll} Y_{10} \cong \omega_e & Y_{20} \cong -x_e\omega_e & Y_{30} \cong y_e\omega_e \\ Y_{01} \cong B_e & Y_{11} \cong -\alpha_e & Y_{21} \cong \gamma_e \\ Y_{02} \cong -D_e & Y_{12} \cong -\beta_e & \\ Y_{03} \cong H_e & & \end{array}$$

With a set of Y_{ij} the ro-vibrational spectrum of one isotopomer can be derived, since the Dunham parameters still depend on the reduced mass μ of the nuclei A and B:

$$Y_{ij} \propto \mu^{-\left(\frac{i}{2}+j\right)} \quad with \quad \mu = \frac{M_A \cdot M_B}{M_A + M_B} \tag{4.20}$$

With expression 4.20 it is possible to define a set of isotopically invariant parameters U_{ij} which describe all isotopomers of a molecule:

$$U_{ij} = \mu^{\left(\frac{i}{2}+j\right)} Y_{ij} \tag{4.21}$$

In most cases the strict validity of then Born-Oppenheimer approximation is an idealization of the real conditions in a diatomic molecule. Therefore equation 4.21 has to be modified to a more general expression:

$$Y_{ij} = \mu^{-\left(\frac{i}{2}+j\right)} U_{ij}^{BO} \left[1 + \frac{m_e \Delta_{ij}^A}{M_A} + \frac{m_e \Delta_{ij}^B}{M_B} + O\left(\frac{m_e^2}{M_k^2} \right) \right] \tag{4.22}$$

where m_e is the mass of an electron and U_{ij}^{BO} the isotopically invariant parameter in case of the Born-Oppenheimer approximation. Δ_{ij}^A and Δ_{ij}^B are the Born-Oppenheimer breakdown corrections for the nuclei A and B, respectively. Higher order terms ($O\left(\frac{m_e^2}{M_k^2} \right)$) can usually be neglected. In most cases, the deviations from the Born-Oppenheimer approximation for higher order mass independent Dunham parameters U_{ij}^{BO} are very small. Thus, only the breakdown corrections for $U_{01}^{BO} = \frac{\hbar}{4\pi r_e^2}$ are significant.

4.3   Spectra of Radicals and Ions

Radicals and ions reveal much more complicated spectra, because of the not vanishing electronic orbital angular momentum and/or electronic spin. This is caused by one or more unpaired electrons. In this section the Hamiltonian for rotational spectra of linear radicals in a $^2\Sigma$ (CO^+) or $^2\Pi$ (C_3H) ground electronic state will be derived. An energy level diagram of a radical in a $^2\Pi$ ground state is given in Fig. 4.1 to illustrate the occurring effects.
Radicals are classified in the following way:

$$^{2S+1}|\Lambda|_\Omega \tag{4.23}$$

Here $(2S+1)$ is the electronic multiplicity, S is the total electron spin, and Λ is the total electronic orbital angular momentum. It is common to designate states with $\Lambda = 0$, 1, 2,... with capital Greek letters Σ, Π, Δ, etc. In case $S \neq 0$ and/or $\Lambda \neq 0$, the electronic spin and/or the electronic orbital momentum couple to the rotational motion of the molecule to a total angular momentum J. Hund [72] described five possibilities for this coupling two of which will be discussed in the following. The occurring angular momenta and their projections are summarized in Tab. 4.1.

4.3.1   Hund's Case a) and b)

In Hund's case a) ($\Lambda \neq 0$) the resultant electronic angular momentum L is strongly coupled to the molecular axis. The electronic spin S couples to L
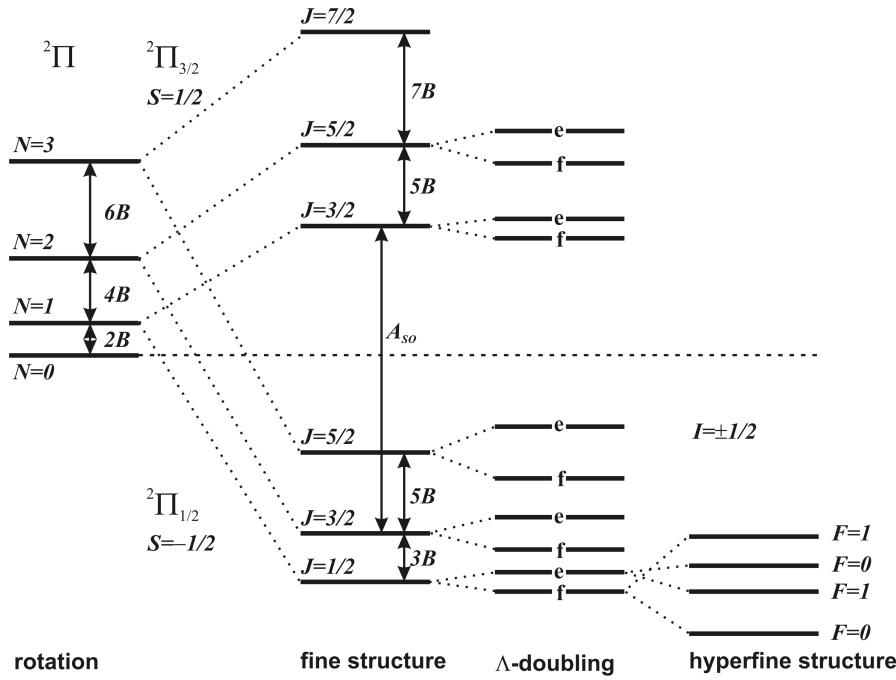
Figure 4.1: Schematic energy level diagram of a $^2\Pi$ radical with a total nuclear spin of $I = \frac{1}{2}$. The magnitudes of the effects usually decrease from the left to the right side (rotation, fine structure, Λ-doubling, and hyperfine structure).

and thus to the molecular axis as well. $(L+S)$ are weakly coupled to the rotational motion R. Here Ω is a good quantum number (see Fig. 4.2 a)):

$$\Omega = \Lambda + \Sigma \tag{4.24}$$

Ω and R result in the total angular momentum J. A characteristic for molecules within Hund's case a) approximation is the expression [68]:

$$2JB \ll |\Lambda A_{SO}| \tag{4.25}$$

In Hund's case b) the orbital angular momentum L couples with the rotation R to the total angular momentum N without spin of the rotational motion R. Here Ω is not a good quantum number (see Fig. 4.2 b)).

$$N = R + L \tag{4.26}$$

The electronic spin S then couples to N and thus to the end-over-end rotation of the molecule.

$$J = N + S \tag{4.27}$$

4.3.2   Fine Structure

The effects assigned to the fine structure are mainly the electronic spin-rotational, spin-orbital, and spin-spin interaction which appear due to unpaired electrons. They outcrop as substructure of the rotational spectrum

Table 4.1: Angular momenta and their projections.

R	angular momentum of the end-over-end rotation of the molecule
L	resultant electronic orbital angular momentum
Λ	projection of L along the molecular axis
S	resultant electronic spin
Σ	projection of S along the molecular axis
N	angular momentum ignoring the electronic spin
J	total angular momentum ignoring nuclear spin
Ω	resultant angular momentum along the molecular axis
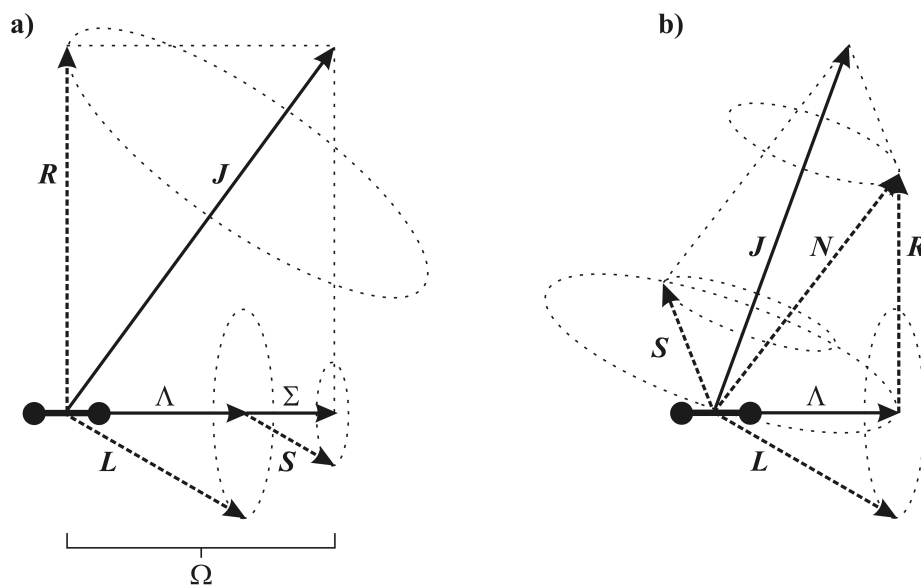
Figure 4.2: Vector diagram of the coupling according to Hund's case a) and b), taken from the textbook of Gordy and Cook [68].

and sometimes appear to be the dominating effect for low rotational transitions. Thus, the Hamiltonian describing the fine structure is the sum of three terms:

$$\hat{H}_{FS} = \hat{H}_{NS} + \hat{H}_{SO} + \hat{H}_{SS} \tag{4.28}$$

The first term in the sum of equation 4.28 considers the electronic spin-rotational interaction. The electrons of a rotating radical generate a weak magnetic field which interacts with the electronic spin. The Hamiltonian of the spin-rotational interaction can be written as:

$$\hat{H}_{NS} = \gamma \hat{N} \cdot \hat{S} + \gamma_D \left(\hat{N} \cdot \hat{S} \right) \cdot \hat{N}^2 \tag{4.29}$$

This effect always appears for radicals with a multiplicity of $2S + 1 \geq 2$ and is the only fine structure component of a molecule in the $^2\Sigma$ state. γ is the associated parameter and γ_D its distortion constant.

There is an isotopically invariant notation for the spin-rotational interaction parameter γ analog to the rotational motion (see Chapter 4.2.2):

$$\gamma_{v,N} = \sum_{i,j=0}^{\infty} \mu^{-\left(\frac{i}{2}+j+1\right)} G_{ij} \left(v + \frac{1}{2}\right)^i N^j (N+1)^j \qquad (4.30)$$

G_{ij} is the isotopically invariant parameter of the spin-rotational interaction.

In case a molecule has an electronic orbital angular momentum, this can interact with a non-vanishing electronic spin to generate a strong effect. The Hamiltonian of the spin-orbit interaction is given by:

$$\hat{H}_{SO} = A_{SO}\hat{S} \cdot \hat{L} \qquad (4.31)$$

A_{SO} is the spin-orbital parameter. It is common to introduce $A_{eff} = A_{SO} + \gamma$ due to a strong correlation between A_{SO} and γ in a strong Hund's case a).

The third fine structure component of equation 4.28 occurs in case a molecule has more than one unpaired electron, e.g. O_2 and C_4. The spin-spin interaction is expressed by:

$$\hat{H}_{SS} = \frac{2}{3}\lambda \left(3\hat{S}_z^2 - \hat{S}^2\right) \qquad (4.32)$$

4.3.3 Hyperfine Structure

Any atomic nucleus, which possesses either an odd mass number, an odd atomic number, or both, has a spin angular momentum and a magnetic moment. The spectra of molecules, which have at least one atom with a nuclear spin, display hyperfine structure. Due to interaction of the nuclear spin(s) with the angular momenta of the molecule the energy levels are split into further levels with usually smaller spacings than those of the fine structure. However, there are exceptions from this rule, for example the molecule $^{13}CCCN$ has a large Fermi-contact interaction which exceeds that of the spin-rotation interaction. The rotational angular momentum $\hat{J}$ and the nuclear spin $\hat{I}$ couple to the resultant angular momentum $\hat{F} = \hat{J} + \hat{I}$. Thus, for example the rotational levels of molecules containing a nucleus with $I = \frac{1}{2}$, like C_3H, are split into doublets according to $F = J - \frac{1}{2}$, $J + \frac{1}{2}$. Tab. 4.2 specifies the nuclear spins of some elements which are mentioned in this work.

The hyperfine structure consists of several effects summarized in the following expression for the Hamiltonian:

$$\hat{H}_{HFS} = \hat{H}_{IL} + \hat{H}_F + \hat{H}_{IS} + \hat{H}_{IN} + \hat{H}_d + \hat{H}_Q \qquad (4.33)$$

The first term in equation 4.33, $\hat{H}_{IL}$, describes the nuclear spin - electronic orbital interaction. It is the analog to the electronic spin-rotational interaction of the fine structure. The operator can be written as:

$$\hat{H}_{IL} = a\hat{I} \cdot \hat{L} \quad with \quad a = \frac{2\mu_B \mu_I}{I} \left(\frac{1}{r^3}\right) \qquad (4.34)$$

Table 4.2: Atomic weights, relative abundances, and nuclear spins of some elements, mentioned in this work. The values are taken from [73], [74], [75], [76], and [77]. The number in parentheses following the mass and the abundance value are the uncertainties in the last digit(s) given.

Element	Relative abundance	Atomic weight [amu]	Nuclear spin
^1H	99.98850(70)	1.0078250321(4)	1/2
^2H	0.0115(70)	2.014101778(4)	1
^3H	0.0	3.0160492675(11)	1/2
^6Li	7.59(4)	6.0151223(5)	1
^7Li	92.41(4)	7.0160040(5)	3/2
^{12}C	98.93(8)	12.0(0)	0
^{13}C	1.07(8)	13.0033548378(10)	1/2
^{14}C	0.0	14.003241988(10)	0
^{14}N	99.632(7)	14.0030740052(9)	1
^{15}N	0.368(7)	15.0001088984(9)	1/2
^{16}O	99.757(16)	15.9949146221(15)	0
^{17}O	0.038(1)	16.99913150(22)	5/2
^{18}O	0.205(14)	17.9991604(9)	0
^{23}Na	100.0	22.98976967(23)	3/2
^{32}S	94.93(31)	31.97207069(12)	0
^{33}S	0.76(2)	32.9714585(12)	3/2
^{34}S	4.29(28)	33.96786683(11)	0
^{36}S	0.02(1)	35.96708088(25)	0
^{35}Cl	75.78(4)	34.96885271(4)	3/2
^{37}Cl	24.22(4)	36.96590260(5)	3/2
^{39}K	93.2581(44)	38.9637069(3)	3/2
^{40}K	0.0117(1)	39.96399867(29)	4
^{41}K	6.7302(44)	40.96182597(28)	3/2

where μ_B is the Bohr magneton, μ_I is the nuclear magneton, and I is the nuclear spin.

The Fermi contact term $\hat{H}_F$ arises from the non vanishing probability density of the electron at the nucleus' location. It is given by:

$$\hat{H}_F = b\hat{I} \cdot \hat{S} \quad with \quad b = \frac{g\mu_B\mu_I}{I}\left(\frac{8\pi}{3}\Psi^2(0) - \frac{3\cos^2(\Theta) - 1}{2r^3}\right) \qquad (4.35)$$

where g is the Landé-Factor, Θ designates the angle between the molecular axis and the radius r from the nucleus to the electron. $\Psi(0)$ is the wave-function of the electron at the location of the interacting nucleus. $\hat{H}_{IS}$ is the nuclear spin - electronic spin interaction term (dipole-dipole interaction). It can be expressed by:

$$\hat{H}_{IS} = c\left(\hat{I} \cdot \hat{k}\right)\left(\hat{S} \cdot \hat{k}\right) \quad with \quad c = \frac{3g\mu_B\mu_I}{I}\left(\frac{3\cos^2(\Theta) - 1}{r^3}\right) \qquad (4.36)$$

where $\hat{k}$ is the unit vector along the molecular axis. c is also available in an isotopically invariant form:

$$c = \frac{\mu_I}{\mu_N}\frac{ge^2\hbar}{16\pi m_e m_p c^2 I}\sum_{i,j=0}^{\infty}\mu^{-\left(\frac{i}{2}+j\right)}c_{ij}\left(v+\frac{1}{2}\right)^i N^j(N+1)^j \qquad (4.37)$$

where $\frac{\mu_I}{\mu_N}$ is the magnetic momentum of the nucleus in units of the nuclear magneton $\mu_N = \frac{e\hbar}{2m_p}$, m_e is the electron mass, and m_p the proton mass.

It is common to use the Fermi contact parameter b_F:

$$b_F = b + \frac{c}{3} = \frac{g\mu_B\mu_I}{I}\left(\frac{8\pi}{3}\Psi^2(0)\right) \qquad (4.38)$$

which can be written in an isotopically invariant way:

$$b_F = \frac{\mu_I}{\mu_N}\frac{ge^2\hbar}{3m_e m_p c^2 I}\sum_{i,j=0}^{\infty}\mu^{-\left(\frac{i}{2}+j\right)}b_{F,ij}\left(v+\frac{1}{2}\right)^i N^j(N+1)^j \qquad (4.39)$$

The operator $\hat{H}_{IN}$ is assigned to the interaction between the rotation of the molecule and the nuclear spin. This weak effect arises from a non spherical distribution of valence electrons rotating with the molecule which generate a magnetic field at the nucleus' location. The associated constant is C_I and the Hamiltonian can be written as:

$$\hat{H}_{IN} = C_I\hat{I} \cdot \hat{N} \qquad (4.40)$$

The constant C_I can be expressed in an isotopically invariant way:

$$C_I = \frac{\mu_I}{\mu_N I}\sum_{i,j=0}^{\infty}\mu^{-\left(\frac{i}{2}+j+1\right)}C_{I,ij}\left(v+\frac{1}{2}\right)^i J^j(J+1)^j \qquad (4.41)$$

$\hat{H}_d$ is the Hamiltonian considering the hyperfine Λ-doubling term. For a $^2\Pi_{1/2}$ state in Hund's case a) the splitting due to this effect is:

$$\Delta E_d = \pm \frac{d\left(J + \frac{1}{2}\right)}{2J(J+1)} \hat{I} \cdot \hat{J} \quad with \quad d = \frac{3g\mu_B\mu_I}{I}\left(\frac{\sin^2(\Theta)}{r^3}\right) \tag{4.42}$$

For the $^2\Pi_{3/2}$ state ΔE is equal to zero. The Hamiltonian for the hyperfine Λ-doubling can be deduced to:

$$\hat{H}_d = \frac{1}{2}d\left(I_+S_+e^{-2i\phi} + I_-S_-e^{+2i\phi}\right) \tag{4.43}$$

The definition of the constants a, b, c and d follows the notation of Frosch and Foley [78] and Steimle et al. [79].

The electric quadrupole hyperfine interaction (last term of Eq. 4.33) appears with nuclei having nuclear spin $I \geq 1$ and consequently a nuclear quadrupole momentum Q. This interacts with the electric field of the electrons. The corresponding Hamiltonian can be written as:

$$\hat{H}_Q = \frac{eQq_J}{2J(2J-1)I(2I-1)}\left[3\left(\hat{I}\cdot\hat{J}\right)^2 + \frac{3}{2}\hat{I}\cdot\hat{J} - \hat{I}^2\cdot\hat{J}^2\right] \tag{4.44}$$

where eQ is the electric quadrupole moment of the nucleus and q_J is the expectation value of the component of the electric field gradient along the space-fixed z-axis. q_J depends on the molecular structure and is for linear molecules deduced to:

$$q_J = -q\frac{J}{2J+3} \tag{4.45}$$

The energy can be expressed by:

$$E_Q = -eQq \cdot \frac{\frac{3}{4}C(C+1) - I(I+1)J(J+1)}{2(2J-1)(2J+3)I(2I-1)} \tag{4.46}$$

where $C = F(F+1) - J(J+1) - I(I+1)$ is the Casimir function. The parameter eQq is the electric nuclear quadrupole coupling constant. It can be expressed in an isotopically invariant form:

$$eQq = Q\sum_{i,j=0}^{\infty}\mu^{-\left(\frac{i}{2}+j\right)}eQq_{ij}\left(v+\frac{1}{2}\right)^i J^j(J+1)^j \tag{4.47}$$

4.3.4   Vibronic Angular Momentum: l- and Λ-type Doubling

Linear molecules with more than two atoms have doubly degenerated vibrational bending modes in addition to their symmetric and antisymmetric stretching vibrations. If a bending mode is excited an additional vibrational angular momentum $(p_z = l\hbar)$ about the internuclear axis appears, where

$l = v_i,\ v_i - 2,\ v_i - 4, ...,\ -v_i$ is the quantum number of vibrational angular momentum and v_i is the vibrational quantum number of the ith bending mode. This effect is called l-type doubling. The rotational energy can be written as:

$$E_{rot} = B\left[J(J+1) - l^2\right] \tag{4.48}$$

where J is the total angular momentum including l ($J = |l|,\ |l|+1,\ |l|+2,...$). The rotational levels of equation 4.48 are doubly degenerated due to $l = \pm|l|$ which is lifted by Coriolis force interaction. For $|l| = 1$ (vibrational Π-state) the energy of the l-type splitting is calculated by:

$$\Delta\nu_{|l|=1} = \frac{1}{2}q\left(v_i + 1\right)J(J+1) \tag{4.49}$$

where q is the l-type doubling (vibrational-rotational coupling) constant. The expression 4.49 simplifies in the first excited state to:

$$\Delta\nu_{|l|=1} = qJ(J+1) \tag{4.50}$$

For radicals with a non vanishing orbital angular momentum $\Lambda \neq 0$ ($|\Lambda| = 0,\ 1,\ 2,...$ corresponding to Σ, Π, Δ,... electronic states) the energy levels of a rotating molecule are split in doublets which are labeled with e and f related to the parity of the wave function Ψ. The effect, called Λ-type doubling, is completely analogous to the above-mentioned l-type doubling. The splitting arises from the two possible values for $\Lambda = \pm|\Lambda|$. In the non rotating system these levels are degenerated, but as the molecule begins to rotate, the electronic orbital angular momentum decouples cumulative from the internuclear axis towards a stronger coupling of L to the rotation R. A shift from Hund's case a) to case d) with strong L-R coupling is to be ascertained. The Λ-type doubling is significantly smaller than the fine structure effects and is described by the parameter p.

The vibrational angular momentum is coupled with the electronic angular momentum to a resultant vibronic angular momentum:

$$p_{ev} = K\hbar \quad with \quad K = \Lambda + l \tag{4.51}$$

Here $|K| = 0,\ 1,\ 2,...$ corresponds to Σ, Π, Δ,... vibronic states. K as well as Λ and l can be either negative or positive.

In case the electron spin is strongly coupled to the orbital angular momentum the total electronic angular momentum $p_{tot} = \Omega\hbar$ appears where $\Omega = \Lambda + \Sigma$ and $\Sigma\hbar$ is the component of the spin along the internuclear axis. The quantum number of the resultant vibronic angular momentum including spin is called P:

$$P = \Omega + l \tag{4.52}$$

It is common to define an effective Λ-type doubling constant which includes the l-type doubling constant as:

$$p_{eff} = p + 2q \tag{4.53}$$

4.3.5   Vibronic interaction: Renner-Teller Effect

Renner was the first to study the effect of the electronic motion on the bending vibrational wave function. In a first approximation the vibronic wave function, describing the electronic and vibrational motions of a molecule, can be written as a product of the electronic and the vibrational wave functions.

$$\Psi_{ev}(q,Q) = \Psi_e(q)\Psi_v(Q) \tag{4.54}$$

where q and Q stand for all electronic and nuclear coordinates, respectively. In this approximation, there is a doubly degenerated electronic state $\pm\Lambda$ with energy $E^{el}_{|\Lambda|}$ as well as $v+1$ degenerated bending vibrational states with $l = -v,\ -v+2,...,\ v-2,\ v$ and energy $\hbar v(v+1)$. The eigenvalues of the product in Eq. 4.54 are the resultant vibronic angular momenta $p_{ev} = K\hbar$. In zeroth-order these levels are degenerate with a total energy $E^{el}_{|\Lambda|} + \hbar v(v+1)$. The bending of the molecule generates a coupling between the electronic and vibrational motion which acts as a perturbation, the so called vibronic coupling. Most vibronic angular momenta occur as pairs except those with $K = (v+\Lambda),\ (v+\Lambda-2),...,\ (v-\Lambda+2)$. For a Π state, for instance, the only unique level is the one with $|K| = v+1$. The repulsion of those pairs dominates the splitting in an energy level diagram (see Fig. 4.3). To get a quantitative relation for the splittings, one has to consider the variation of the potential energy with the bending coordinate. The potential function of a degenerated electronic state V^0 is split into an upper component V^+ and a lower one V^-, in case the molecule is bent. This was first mentioned by Teller and Pöschl [80] (1933) and later worked out by Renner [81] in 1934. In Fig. 4.4 the potential energies of a Σ, Π, and Δ state, respectively, are shown schematically as functions of the bending coordinate r. Barring the Σ state, the potential curves are split into two components. The diagrams at the top correspond to a small vibronic interaction, while for those at the bottom a large interaction is assumed.

Due to symmetry reasons, the potential functions have to depend on even powers of r, and V^0 can be written as:

$$V^0 = ar^2 + br^4 + ... \tag{4.55}$$

The splittings of the potential functions in Π, Δ,... states have to be of the same form:

$$V^+ - V^- = \alpha r^2 + \beta r^4 + ... \tag{4.56}$$

For a strong vibronic interaction where $\frac{1}{2}\alpha > a$ the potential function has a maximum at $r = 0$, while the minimum is shifted to a non-zero value of $|r|$. This is shown in the lower diagrams of Fig. 4.4.

The first experimental evidence for Renner-Teller splitting occurred for molecules in $^2\Pi$ electronic state. Even though there are examples of $^1\Pi$ molecules revealing Renner-Teller splitting, it is obvious that the effect depends on a non-vanishing electronic spin interacting with vibronic motion. This approach was first used by Pople [83], whose results are illustrated in
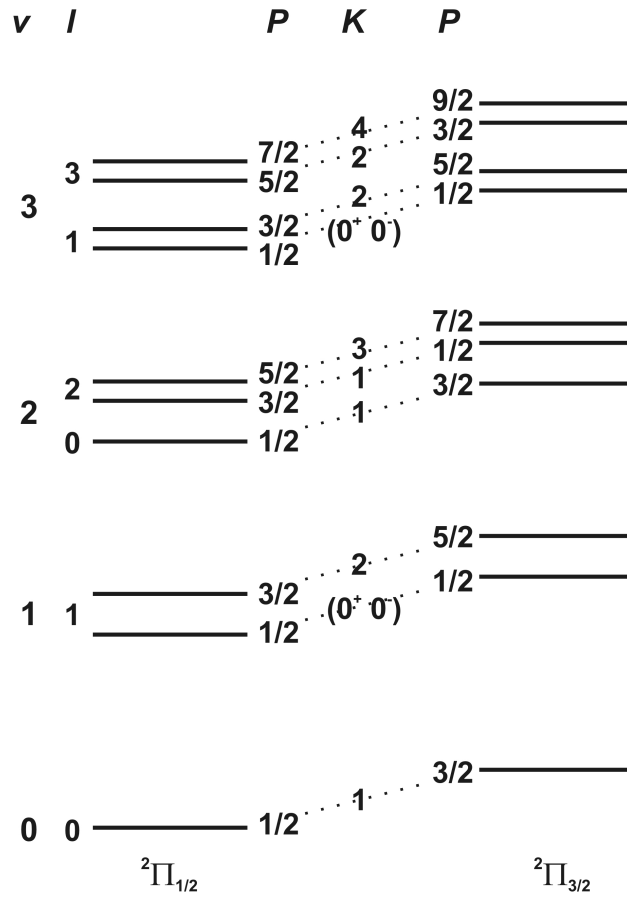
Figure 4.3: Vibrational levels of the bending vibration in a $^2\Pi$ electronic state of a linear molecule. Shown are the quantum numbers P for the resultant vibronic angular momentum including spin and K for the vibronic angular momentum ignoring spin as well as for the rotational angular momentum (l) and for the degenerated bending vibration (v).

Fig. 4.5. In the diagram the actual energy levels of a $^2\Pi$ electronic state are shown compared to those with vanishing Renner-Teller interaction (left) and those with vanishing spin-orbit interaction (right) for the bending vibrational ground state and the first two excited states ($v = 0,\ 1,\ 2$). The levels are designated by K (indicated by the symbols Σ, Π, Δ,...) which is not a good quantum number. The good quantum number P is written as subscript of K. In a first approximation the levels with $K = v + 1$ split into two levels upon introduction of the spin-orbit coupling with energies of:

$$E(v, K, \Sigma) = \omega(v+1) + A_{SO}\Sigma - \frac{1}{8}\varepsilon^2 \omega K(K+1) \qquad (4.57)$$

In Eq. 4.57, Σ is the spin quantum number, representing the component of S along the internuclear axis which takes values of $\pm\frac{1}{2}$. ε is the Renner parameter with:

$$\varepsilon = \frac{\alpha}{2a} \qquad (4.58)$$
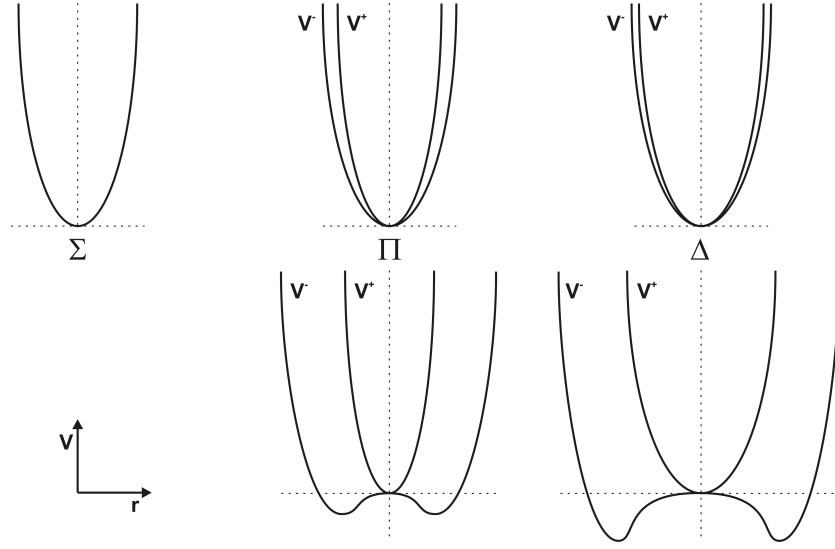
Figure 4.4: Potential functions for bending vibration Σ, Π, and Δ electronic states of linear molecules (taken from [82]). r is the bending coordinate. The diagrams at the top correspond to small vibronic interaction, those at the bottom to large vibronic interaction.

According to Eq. 4.57 the spin splitting for the component with $K = v+1$ is:

$$\Delta \nu_{K=v+1} = A_{SO} \tag{4.59}$$

In this approximation the splitting is independent of the vibronic interaction. In a higher approximation the splitting slightly depends on K, as mentioned by Hougen [84]:

$$\Delta \nu_{K=v+1} = A_{SO} \left[1 - \frac{1}{8} \varepsilon^2 K(K+1) \right] \tag{4.60}$$

Herzberg [82] determined the following energy levels for vibronic states where $K < v+1$:

$$
\begin{aligned}
E^+ \left(v, K, \pm \frac{1}{2}\right) &= \omega \left(1 - \frac{1}{8}\varepsilon^2\right)(v+1) + \frac{1}{2}A^*_{SO}(v,K) \mp \frac{\varepsilon^2 A_{SO}\omega K(v+1)}{8A^*_{SO}(v,K)} \\
E^- \left(v, K, \pm \frac{1}{2}\right) &= \omega \left(1 - \frac{1}{8}\varepsilon^2\right)(v+1) - \frac{1}{2}A^*_{SO}(v,K) \pm \frac{\varepsilon^2 A_{SO}\omega K(v+1)}{8A^*_{SO}(v,K)}
\end{aligned}
\tag{4.61}
$$

where $A^*_{SO}(v,K)$ is an effective spin splitting constant with inclusion of vibronic interaction terms:

$$A^*_{SO}(v,K) = \sqrt{A_{SO}^2 + \varepsilon^2 \omega^2 \left[(v+1)^2 - K^2\right]} \tag{4.62}$$

Introducing a non-vanishing Rener-Teller interaction the doublet splitting of states with $0 < K < v+1$ (see Fig. 4.5) is increased from A_{SO} to:

$$\Delta \nu_{0<K<v+1} = A^*_{SO}(v,K) \tag{4.63}$$

This effect is caused by the mutual repulsion of levels with the same P and decreases with increasing P. Therefore, the two center levels are not repulsed, since their P quantum numbers are different. The doublet levels are shifted up and down, respectively, by the last terms of Eqs. 4.61:

$$\Delta \nu_{RT} = \pm \frac{\varepsilon^2 A_{SO} \omega K (v+1)}{8 A_{SO}^*(v,K)} \tag{4.64}$$

where one doublet is normal and the other one is inverted.

Figure 4.5: Correlation of the vibronic levels of a $^2\Pi$ electronic state with vanishing vibronic (left; $\varepsilon = 0$) and vanishing spin-orbit interaction (right; $A_{SO} = 0$) with those levels where both interactions are non-zero (taken from [82]). Here K (indicated by the symbols Σ, Π, Δ,...) is not a good quantum number. Therefore, the good quantum number P is given as subscript to K. The C_3H radical, which has been investigated in this work, is a prime example for the intermediate case where both effects occur. It has a large Renner-Teller coupling constant of about 0.9.

4.3.6 Coriolis-Type Interaction

The Coriolis force is a type of fictitious force which can appear in an accelerated coordinate system. A particle forced to move at a constant angular velocity $\boldsymbol{\omega}$ will proceed to move in a straight line with constant velocity v, if released. The motion of the unaffected particle in the laboratory frame is linear. In the frame rotating with an angular velocity $\boldsymbol{\omega}$ the particle moves both radially at a constant velocity and laterally, contrariwise to the rotation, due to Coriolis force. It has a value of:

$$F_C = 2\,\vec{v} \times \vec{\omega} \qquad\qquad (4.65)$$

Coriolis forces are also important in the case of a rotating and vibrating molecule. As the rotating molecule stretches, its rotation is slowed down by Coriolis forces whereas its contraction leads to an acceleration. These changes in the rotational velocity may be ascribed to the conservation of angular momentum, but part of this effect must be attributed to Coriolis forces. The impact of Coriolis forces on a triatomic linear molecule in different vibrational modes is shown in Fig. 4.6. It is obvious that the vibration v_2 excites a vibration v_3 and vice versa due to Coriolis interactions. These perturbations only occur between levels of the same J and with similar symmetry.
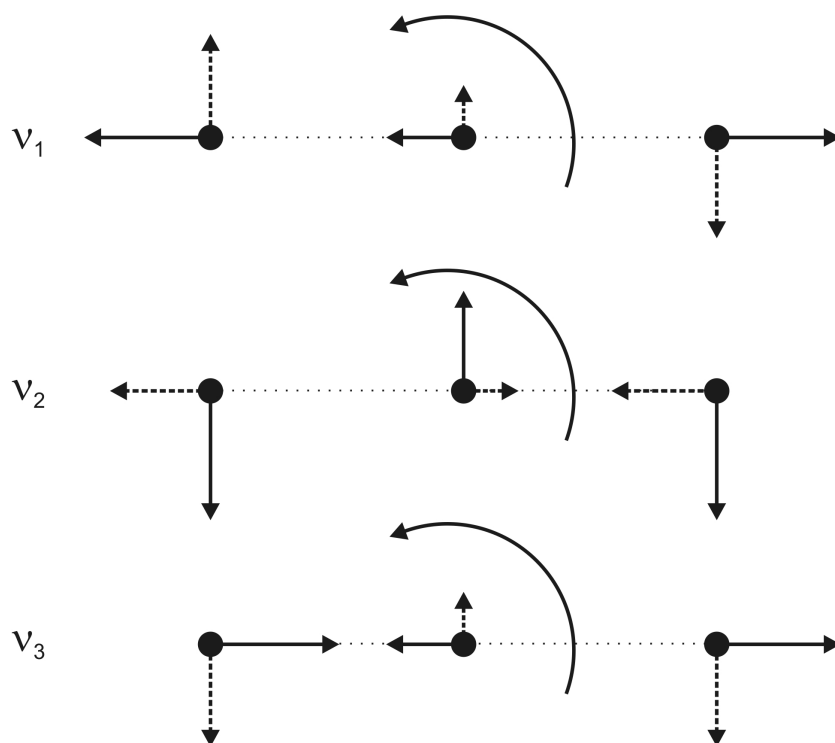
Figure 4.6: Coriolis forces in a linear triatomic molecule. The solid arrows indicate the normal motion of the vibrational modes. The dashed arrows give the direction of the Coriolis forces to a given rotation, indicated by the curved arrows.

For a triatomic molecule with four modes of vibration, two of which are degenerated, one derives from Eq. 4.13:

$$B_v = B_e - \alpha_1 \left(v_1 + \frac{1}{2} \right) - \alpha_2 \left(v_2 + 1 \right) - \alpha_3 \left(v_3 + \frac{1}{2} \right) \qquad (4.66)$$

The α-coefficients are evaluated from the molecular potential. Nielsen [85] obtained for the α-coefficients:

$$\alpha_1 = \frac{2B_e^2}{c\omega_1} \cdot \left(1 - 4\xi_{21}^2 \frac{\omega_1^2}{\omega_1^2 - \omega_2^2} - 4\xi_{23}^2 + 6\Theta_e^{1/2} \frac{\xi_{23} k_{111}}{4\pi^2 c^2 \omega_1^2} + 2\Theta_e^{1/2} \frac{\xi_{21} k_{113}}{4\pi^2 c^2 \omega_3^2} \right) \qquad (4.67)$$

$$\alpha_2 = \frac{B_e^2}{c\omega_2} \left[-4\Theta_e^{1/2} \frac{\xi_{21} k_{223}}{4\pi^2 c^2 \omega_3^2} + 4\Theta_e^{1/2} \frac{\xi_{23} k_{122}}{4\pi^2 c^2 \omega_1^2} - \left(3\omega_2^2 + \omega_1^2 \right) \frac{\xi_{21}^2}{\omega_2^2 - \omega_1^2} - \left(3\omega_2^2 + \omega_3^2 \right) \frac{\xi_{23}^2}{\omega_2^2 - \omega_3^2} \right] \qquad (4.68)$$

where k_{xyz} are the anharmonic potential coefficients of:

$$V_{anharm.} = k_{111} q_1^3 + k_{113} q_1^2 q_3 + k_{133} q_1 q_3^2 + k_{322} q_1 q_2^2 + k_{333} q_3^3 \qquad (4.69)$$

with q_i being the normal coordinates. α_3 is similar to α_1 with the indices 1 and 3 interchanged throughout. Coriolis forces are generally ascribed to resonant terms of expressions 4.67 and 4.68, for example:

$$-\frac{B_e^2 \left(3\omega_2^2 + \omega_3^2 \right)}{c\omega_2 \left(\omega_2^2 - \omega_3^2 \right)} \xi_{23}^2 \qquad (4.70)$$

The term 4.70 would become very large if ω_2 were very close to ω_3 which is called coupling of the vibrational modes ω_2 and ω_3.

Tab. 4.3 summarizes some important interactions, with their associated parameters and quantum numbers. Additionally, the molecules for which a certain parameter has been determined in this work are given.

Table 4.3: Important interactions, associated parameters, quantum numbers, and molecules for which a certain parameter has been determined in this work.

Type	Parameter (invariant)	Interaction	Quantum Number	Molecule this work
fine structure	$\gamma\,(G_{ij})$	electr. spin - rotation	N, S	C_3H, CO^+
	γ_D	distortion parameter of γ	N, S	C_3H
	A_{SO}	electr. spin - orbital	S, L	C_3H
	A_{eff}	effective electr. spin - orbital	S, L	
	λ	electr. spin - spin	S	
l- and Λ-type doubling	q	bending vibration doubling	v_i, l	C_3H
	q_D	distortion parameter of q	v_i, l	C_3H
	p, q_Λ	rotational - electr. orbital	R, L	C_3H
	p_D	distortion parameter of p	R, L	C_3H
	p_{eff}	effective Λ-type doubling	R, L, v_i, l	
hyperfine structure	a	nuclear spin - electr. orbital	I, L	C_3H
	$b, b_F\,(b_{F,ij})$	Fermi-contact	I, S	C_3H, CO^+
	$c, t\,(c_{ij})$	electr. dipole - nuclear dipole	I, S	C_3H, CO^+
	d	hyperfine Λ-doubling	I, S	C_3H
	C_I	nuclear spin - rotational	I, N	
	eQq	electr. quadrupole	I	
	G_C	Coriolis-type		C_3H
	ε	Renner-Teller		C_3H

5

KCl: An Alkali Halide of Astrophysical Relevance

Cernicharo and Guélin [14] reported the detection of the four metal halides *KCl*, *NaCl*, *AlCl*, and *AlF* in the warm, inner and dense circumstellar envelope of the late type star IRC+10216 in 1987. The rotational lines were observed in the frequency-region between 90 and 170 *GHz* with the IRAM 30 *m* telescope. Among the large number of rotational transitions found in this survey work, six lines were assigned to the ground vibrational states of both $K^{35}Cl$, $Na^{35}Cl$ and one transition to $Na^{37}Cl$. Seven lines were ascribed to aluminum bearing molecules, i.e. $Al^{35}Cl$, $Al^{37}Cl$, and *AlF*. The relative high interstellar abundances of aluminum, sodium, potassium, and chlorine, i.e. 12th, 13th, 20th, and 19th most abundant, lend encouraging motivation to continue searching towards hotter and even denser core regions as well as in other sources with the aim to find these alkali halides. Very recently, rotational lines of *NaCl* have been detected on Jupiter's moon Io, the smallest of the 4 Galilean satellites, at frequencies of 143 and 234 *GHz* [15]. This demonstrates how special conditions, such as continuous volcanic output, can produce spectroscopic measurable amounts of metal halides.

Experimental studies on diatomic gas phase alkali halides in the laboratory are complicated due to the low vapor pressure of these molecules. Therefore special vaporization conditions are necessary. On the other hand, these species possess a very large dipole moment because of their highly ionic character. Reliable work on the alkali halides has been performed by Clouser and Gordy [3] in 1964. They investigated the pure rotational spectra of four alkali chlorides, i.e. *KCl*, *NaCl*, *RbCl*, and *CsCl*, in the 0.96 *mm* to 3 *mm* wavelength range. Concerning potassium chloride, Clouser and Gordy investigated the frequency from 99 to 268 *GHz* with $J \le 36$. The predictions of line positions for high *J* transitions, which are based on these medium *J* measurements, are reliable only to the millimeter wavelength range.
Another extensive research of infrared emission spectra of *KCl* and *NaCl*, was performed by R. S. Ram et al. [16]. Using a Fourier transform spectrometer at a resolution of 0.01 cm^{-1} they recorded 355 lines belonging to

Table 5.1: Physical parameters of potassium chloride, *KCl*.

Melting point (1 *atm*)	1045 *K*
Boiling point (1 *atm*)	1680 *K*
Isotope abundance ^{35}Cl	75.78
Isotope abundance ^{37}Cl	24.22
Isotope abundance ^{39}K	93.26
Isotope abundance ^{40}K	0.01
Isotope abundance ^{41}K	6.73
Dipole moment, $\mu_0\left(^{39}K^{35}Cl\right)$	10.2690(10) *D*
Dipole moment, $\mu_e\left(^{39}K^{35}Cl\right)$	10.2391(10) *D*
Dipole moment, $\mu_0\left(^{39}K^{37}Cl\right)$	10.2687(10) *D*
Mass ^{39}K	38.9637069 *amu*
Mass ^{40}K	39.96399867 *amu*
Mass ^{41}K	40.96182597 *amu*
Mass ^{35}Cl	34.968852721 *amu*
Mass ^{37}Cl	36.96590262 *amu*

the 1-0, 2-1, 3-2 and 4-3 bands of the main isotopomer of potassium chloride ($^{39}K^{35}Cl$). Their data analysis provided 13 Dunham-Parameters 10 of which are rotational ones.

KCl is a white solid with extremely low vapor pressure under normal temperature and pressure conditions. In Tab. 5.1 the most important physical parameters of potassium chloride necessary for this work are summarized. A high temperature (1407 °*C*) and low total pressures are required to obtain *KCl* in measurable amounts in the gas phase. The temperature range needed to evaporate *KCl* or any other alkali halide, requires special experimental arrangements. The special heater system, mentioned in Section 3.2.1, has been constructed and applied to the spectrometer for this purpose.

In the course of this thesis, the pure rotational transitions of *KCl* have been recorded with very high resolution and frequency accuracy. The spectral range of 170 to 930 *GHz* has been covered using the Cologne Terahertz Spectrometer. These measurements are the extension of the work on *NaCl* described in previous publications [2], [26] under similar experimental conditions. All data have been analyzed and fitted using Pickett's program [86]. Dunham fits have been performed for each isotopomer, and isotopically invariant mass-reduced Dunham constants U_{ij} have been obtained in an isotopically invariant fit. Due to this new parameter set predictions with high accuracy of the pure rotational spectrum of potassium chloride far into the terahertz region are available in the Cologne Database for Molecular Spectroscopy, CDMS [41], [13].

5.1   Experimental

Besides positioning of detector, radiation source, and absorption cell, successful spectroscopy on *KCl* depends on two further parameters:

- heating voltage and current

- partial pressure of buffer gas (*He*)

A voltage of 120 *V* ($\sim$2.5 *A*) heats the substance to a sufficient temperature, of estimated 1000 °*C*, for vaporization at 100 *μbar*. The *KCl*-exhalation becomes visible which leads to a white deposit on the glass cell. Higher voltages predominantly increase the evaporation rate which decreases the time for measurements. The line intensities are hardly influenced, whereas the line width increases significantly due to higher kinetic energies of the evaporated particles. The *KCl* content of the vessel usually allows 3–4 hours of continuous measurements.

The partial pressure of helium, added to reduce the decay of *KCl* on the cell walls, has a strong impact on line intensities. However, the influence on the line width is very small. A partial pressure of 100 *μbar* proved to be best and was, therefore, applied in all measurements.

5.2   Measurements

Five isotopomers of potassium chloride, i.e. $^{39}K^{35}Cl$, $^{39}K^{37}Cl$, $^{41}K^{35}Cl$, $^{41}K^{37}Cl$, and $^{40}K^{35}Cl$, have been investigated in natural abundance. A total of 295 new rotational lines were observed in the frequency region of 170 to 930 *GHz*. For the isotopomers $^{39}K^{35}Cl$ and $^{39}K^{37}Cl$ 107 and 82, respectively, rotational transitions were assigned from the vibrational ground state up to the 7th excited vibrational ($v \leq 7$) state while the highest J quantum number was 127 (129). 104 lines were measured for the less abundant isotopomers of $^{41}K^{35}Cl$ and $^{41}K^{37}Cl$ with $J \leq 128$, $v \leq 6$ and $J \leq 131$, $v \leq 5$, respectively. Two lines were assigned to $^{40}K^{35}Cl$, which has an abundance of 0.01 % relative to $^{39}K^{35}Cl$ and a half-life time of $1.2 \cdot 10^9$ years. The complete list of the experimental data is available in Appendix A.

As a demonstration of transition lines in high excited states, four spectra, each belonging to an isotopomer of potassium chloride, are shown in Figs. 5.1-5.4. The line indicates the second derivative of the Gaussian function which has been fitted to the measured spectrum represented by dots. Four the less abundant $^{40}K^{35}Cl$ only transitions of the vibrational ground state have been recorded. Fig. 5.5 shows the spectrum of a transition at 333236 *MHz*. The spectrum of this weak transition is very asymmetric due to baseline effects. For the fitted spectrum (line) the baseline was subtracted.
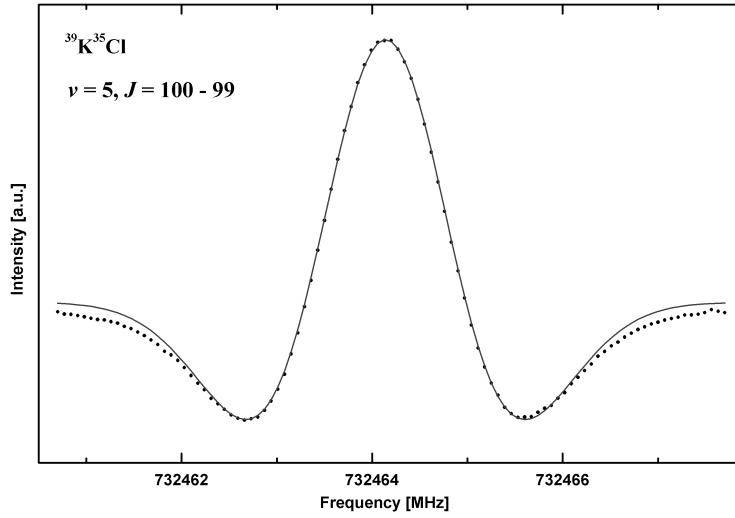
Figure 5.1: Spectrum of a pure rotational transition of $^{39}K^{35}Cl$ ($J = 100 \leftarrow 99$) in vibrationally excited state ($v = 5$). The total excitation energy of this level is 2608.54 cm^{-1}. The the measured spectrum is represented by dots; the line indicates the fitted function.

The signal-to-noise ratio decreases with the abundance of the particular isotopomer, but is still sufficient for the determination of the center frequency with reasonable uncertainties even for transitions of $^{40}K^{35}Cl$.

The positional accuracy of the center frequency of the lines ranges between 10 and 70 *kHz* and in some few cases exceeds 100 *kHz*. The accuracy essentially depends on four factors:

(i) the line width

(ii) signal-to-noise ratio

(iii) baseline variations

(iv) instabilities in the line intensity

The line width is basically caused by Doppler-broadening due to the high temperature of the gas which was estimated to be around 1000 °*C*. A typical value is 1.5 *MHz* at a center frequency of approximately 700 *GHz* which is partially caused by the 2*f*-modulation. The narrower an absorption line appears in the spectrum, the more precise the center frequency can be fitted. A good signal-to-noise ratio is also essential for an accurate determination of the line position. Thus, the experimental error is directly correlated to this ratio.
Baseline variations due to standing-wave-effects can shift line positions by
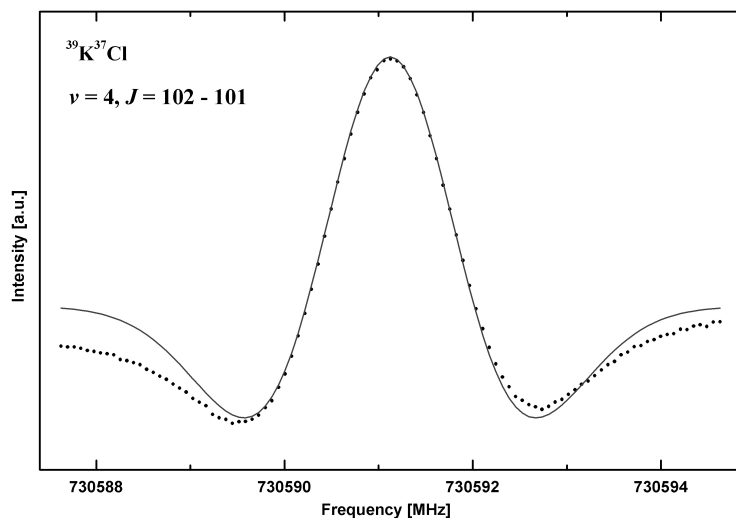
Figure 5.2: Spectrum of a pure rotational transition of $^{39}K^{37}Cl$ ($J = 102 \leftarrow 101$) in vibrationally excited state ($v = 4$). The total excitation energy of this level is 2344.35 cm^{-1}.

several kHz. For very weak lines, for instance in case of $^{40}K^{35}Cl$, the baseline effects can outreach the absorption line (see Fig. 5.5), as a result the errors of those transition frequencies are larger. These effects are minimized by installing beveled microwave windows and careful adjustment of the radiation beam.

According to (iv) the line position accuracy is affected by non stationary salt vapor generation. Experimental line shifts are possible if the concentration of evaporated KCl varies during the scanning of a particular spectrum.

All spectra were recorded twice, once with ascending frequency and a subsequent scan descending in frequency. The total integration time was typically 30–40 seconds for each scan direction, finally both scans were added. The lines were recorded in second derivative to improve the signal-to-noise ratio. This is realized by $2f$-modulation of the BWO's frequency, as mentioned in Section 3.1.4.

5.3   Analysis

The lines recorded in the course of this thesis together with the previous microwave measurements of Clouser and Gordy [3] (14 lines, 9 of $^{39}K^{35}Cl$ and 5 of $^{39}K^{37}Cl$) were subjected to a least squares fit. The experimental frequencies of each isotopomer of KCl were fitted by means of the program of Herb Pickett [86] to the customary Dunham expression (Eq. 4.19) which was treated in Section 4.2.2. The infrared data of Ram et al. [16] was not
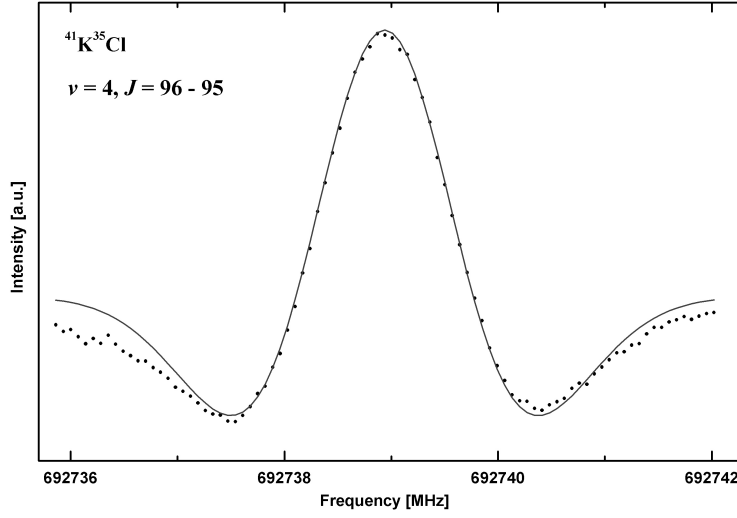
Figure 5.3: Spectrum of a pure rotational transition of $^{41}K^{35}Cl$ ($J = 96 \leftarrow 95$) in vibrationally excited state ($v = 4$). The total excitation energy of this level is 2211.10 cm^{-1}.

included in the fits, as will be explained in the next Section 5.4.

The rotational parameter Y_{01}, equivalent to the common rotational constant B_e, and the centrifugal distortion parameters Y_{02}, Y_{03}, and Y_{04} corresponding to D_e, H_e, and G_e, respectively, have been obtained. $Y_{11} \cong \alpha$, $Y_{21} \cong \gamma$, Y_{31}, $Y_{12} \cong \beta$, $Y_{22} \cong \delta$, Y_{32}, and Y_{13} are the vibrational distortion parameters. All obtained Dunham parameters Y_{ij} are listed in Tab. 5.2 for the four most abundant isotopomers of potassium chloride and are compared to the data of Clouser *et al.* and Ram *et al.* [16].

The mass invariant parameters U_{ij} and the first order Born-Oppenheimer breakdown corrections Δ_{01} have been determined for *KCl* from an additional fit. The results of these isotopically invariant studies are listed in Tab. 5.4, where the obtained RMS-error of the fit was 0.9. The 10 rotational parameters for *KCl* are completed by the isotopical corrections to U_{01}, which are of the order of magnitude of U_{02} and are very well defined especially for chloride.
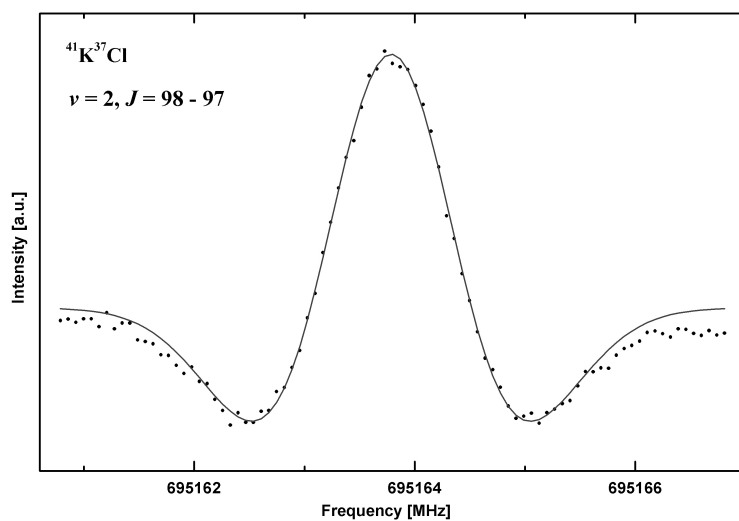
Figure 5.4: Spectrum of a pure rotational transition of $^{41}K^{37}Cl$ ($J = 98 \leftarrow 97$) in vibrationally excited state ($v = 2$). The total excitation energy of this level is 1691.40 cm^{-1}.
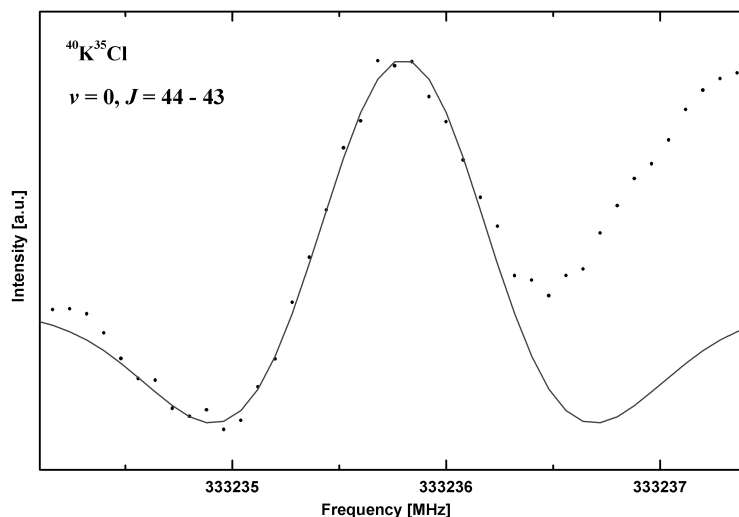
Figure 5.5: Spectrum of a pure rotational transition of $^{40}K^{35}Cl$ ($J = 44 \leftarrow 43$) in vibrational ground state ($v = 0$). The total excitation energy of this level is 249.67 cm^{-1}. The measured spectrum (dots) of this weak transition is very asymmetric due to baseline effects. For the fitted spectrum (line) the baseline was subtracted.

Table 5.2: Equilibrium Rotational Parameters for $^{39}K^{35}Cl$, $^{39}K^{37}Cl$, $^{41}K^{35}Cl$, and $^{41}K^{37}Cl$.

Dunham	This work				Clouser et al. [3]		Ram et al. [16]
Parameters	$^{39}K^{35}Cl$ [MHz]	$^{39}K^{37}Cl$ [MHz]	$^{41}K^{35}Cl$ [MHz]	$^{41}K^{37}Cl$ [MHz]	$^{39}K^{35}Cl$ [MHz]	$^{39}K^{37}Cl$ [MHz]	$^{39}K^{35}Cl$ [MHz]
Y_{01}	3856.367796(114)	3746.575017(134)	3767.392188(293)	3657.59967(43)	3856.373(9)	3746.578(9)	3856.29421(974)
Y_{11}	-23.674222(72)	-22.670090(120)	-22.85937(210)	-21.867632(404)	23.681(13)	22.678(13)	-23.4112(223)
Y_{21}	0.0478580(176)	0.0450656(416)	0.0456132(724)	0.042972(160)	0.049(4)	0.047(4)	-0.1662(141)
$Y_{31} \cdot 10^{3}$	0.12882(150)	0.13024(464)	0.12912(720)	0.1250(203)	-	-	47.85(271)
$Y_{02} \cdot 10^{3}$	-3.2582271(217)	-3.0753687(260)	-3.109656(54)	-2.931084(67)	-3.2600(30)	-3.0780(40)	-3.26111(690)
$Y_{12} \cdot 10^{6}$	-0.35492(384)	-0.3400(64)	-0.3438(114)	-0.2782(262)	2.5(3)	4.1(40)	-29.10(198)
$Y_{22} \cdot 10^{6}$	0.115448(436)	0.107036(792)	0.10716(148)	0.09664(404)	-	-	22.526(648)
$Y_{32} \cdot 10^{6}$	-	-	-	-	-	-	-3.717(117)
$Y_{03} \cdot 10^{9}$	-0.62882(191)	-0.57416(219)	-0.5815(43)	-0.5318(50)	-0.623(8)	-0.571(8)	4.40(321)
$Y_{13} \cdot 10^{11}$	1.1622(112)	1.0646(170)	1.1078(298)	0.85(72)	-	-	-38.19(902)
$Y_{04} \cdot 10^{15}$	-1.210(56)	-1.148(61)	-1.258(120)	-1.077(133)	-	-	-

Table 5.3: Comparison of infrared vibrational parameters of KCl and values derived from microwave measurements; molecular structural constants for KCl.

Parameters	This work (derived)				Clouser et al. [3] (derived)		Ram et al. [16]
	$^{39}K^{35}Cl$	$^{39}K^{37}Cl$	$^{41}K^{35}Cl$	$^{41}K^{37}Cl$	$^{39}K^{35}Cl$	$^{39}K^{37}Cl$	$^{39}K^{35}Cl$
Y_{10} $[cm^{-1}]$	279.889346(936)	275.87497(119)	276.639613(242)	272.577130(312)	279.80(10)	275.80(10)	280.07639(490)
Y_{20} $[cm^{-1}]$	-1.1972502(793)	-1.1632457(733)	-1.169702(236)	-1.135141(307)	-1.167(5)	-1.113(5)	-1.31330(338)
Y_{30} $[cm^{-1}]$	-	-	-	-	-	-	0.014490(607)
I_e $[amu \cdot \text{Å}^2]$	131.05040551(391)	134.89081621(486)	134.14546612(104)	138.17219164(162)	131.1040(53)	134.9459(54)	-
r_e $[\text{Å}]$	2.6666513009(795)	2.6666497859(961)	2.666651648(207)	2.6666500153(314)	2.666772(54)	2.666771(54)	-
I_e^{inv} $[amu \cdot \text{Å}^2]$	131.050401(117)	134.890818(124)	134.145455(123)	138.172204(130)	-	-	-
r_e^{inv} $[\text{Å}]$	2.66665125(238)	2.66664980(245)	2.66665158(244)	2.66665014(251)	-	-	-
I_e^{BO} $[amu \cdot \text{Å}^2]$	131.0484382(156)	134.8889446(161)	134.1434126(160)	138.1702507(165)	-	-	-
r_e^{BO} $[\text{Å}]$	2.666631286(318)	2.666631286(318)	2.666631286(318)	2.666631286(318)	-	-	-

Table 5.4: Isotopically independent parameters for potassium chloride and the first order corrections to the Born-Oppenheimer approximation for U_{01}.

Parameter	Value	Unit
U_{01}	71070.74627(848)	$MHz \cdot amu$
Δ_{01}^{K}	0.3628(626)	
Δ_{01}^{Cl}	$-1.28012(448)$	
U_{11}	$-1872.9837(399)$	$MHz \cdot amu^{3/2}$
U_{21}	16.25029(435)	$MHz \cdot amu^{2}$
U_{31}	0.1894(166)	$MHz \cdot amu^{5/2}$
U_{02}	$-1.10661287(526)$	$MHz \cdot amu^{2}$
$U_{12} \cdot 10^{2}$	$-0.051859(432)$	$MHz \cdot amu^{5/2}$
$U_{22} \cdot 10^{4}$	7.2279(215)	$MHz \cdot amu^{3}$
$U_{03} \cdot 10^{6}$	$-3.92795(833)$	$MHz \cdot amu^{3}$
$U_{13} \cdot 10^{7}$	3.1363(226)	$MHz \cdot amu^{7/2}$
$U_{04} \cdot 10^{10}$	$-1.4407(438)$	$MHz \cdot amu^{4}$

In Tab. 5.3 the derived values are presented: The Dunham parameters Y_{10} and Y_{20}, the equilibrium moment of inertia I_e and the equilibrium nuclear distance r_e, calculated from the measured Y_{01} (see Eq. 4.5) for each isotopomer separately as well as from the U_{01} including the Born-Oppenheimer corrections (I_e^{inv}, r_e^{inv}). The parameters I_e^{BO} and r_e^{BO} have been derived in terms of the Born-Oppenheimer approximation. In this model, the nuclear distance is not affected by the isotopic configuration of the molecule. For the vibrational parameters the following expressions have been used:

$$Y_{10} = \omega_e = 2 \left(\frac{B_e^3}{Y_{02}} \right)^{1/2} \qquad with \qquad B_e \cong Y_{01} \qquad (5.1)$$

$$Y_{20} = -\omega_e x_e = -1.5 B_e^3 \left(a_2 - 1.25 a_1^2 \right) \qquad (5.2)$$

a_k are coefficients of the Dunham potential (see Eq. 4.18). These calculations have been discussed in detail, e.g. in [3].

5.4   Discussion and Conclusion

The observed rotational constants of Clouser's analysis agree with those of this work within the experimental errors (see Tab. 5.2). The values measured by Ram show large deviations, which do not agree within the errors. In particular, their higher order constants (Y_{21}, Y_{31}, Y_{12}, Y_{22}, Y_{03}, and Y_{13}) and the vibrational parameters Y_{10} and Y_{20} (Tab. 5.3) deviate significantly from the derived parameters of this thesis. These inconsistencies are the reason, why the infrared data was not used in the least squares fits of this work.

An explanation might be the overlap of lines of vibrationally excited $^{39}K^{35}Cl$ with those of $^{39}K^{37}Cl$ in lower excited states ($v = 2$), which have similar intensities and rotational spacings. Hence, the $^{39}K^{37}Cl$ lines may interfere significantly with those of $^{39}K^{35}Cl$. Therefore, our analysis is based on pure rotational transitions, mostly recorded in the high resolution mode and with an estimated line accuracy of 5 - 10 kHz. Thus, the rotational parameters of this work are well determined and they reproduce the spectrum with high accuracy.

The invariant analysis of the data of potassium chloride results in non-vanishing Born-Oppenheimer breakdown corrections Δ_{01} (see Tab. 5.4). That means the bond length of *KCl* varies for each isotopomer which is underlined in Tab. 5.3. The deviation of r_e^{inv} from r_e^{BO} ($\sim 2 \cdot 10^{-6}$ Å) results in an increase of approximately $2 \cdot 10^{-3}$ $amu \cdot$Å^2 of the angular momentum I_e^{inv} compared to I_e^{BO}.
The Born-Oppenheimer breakdown corrections are of the order of magnitude of U_{02}. The sign of the correction for chlorine, Δ_{01}^{Cl}, is negative and its absolute value about four times larger in magnitude than the similar constant for potassium, Δ_{01}^{K}. In a previous work on *NaCl* [87], Δ_{01}^{Cl} has been found to be of the same order of magnitude and with the same sign (see Tab. 5.5). For comparison's purpose, 69 transitions of four isotopomers of *LiCl* (see [88] and [89]) were subjected to an isotopically independent fit. Among the U_{ij}'s the Born-Oppenheimer breakdown corrections Δ_{01}^{Cl} and Δ_{01}^{Li} were determined. The values confirm the trend that the absolute value of the Born-Oppenheimer correction for chlorine becomes smaller with increasing mass of the alkali atom. In contrast, the correction for the metal part increases with decreasing mass as one would expect. The ratio between the two parameters is about -2. Due to the inadequate amount of rotational data for *RbCl* [3], the corrections Δ_{01}^{Cl} and Δ_{01}^{Rb} could not be well determined.

The Y_{10} and Y_{20} values for *KCl* from Ram *et al.* (see Tab. 5.3) are rather different from those derived in this work or those by Clouser and Gordy. Correlation between less well-determined higher order spectroscopic parameters with those of lower order or the above mentioned overlap of lines may explain the differences partially.

On the basis of the data presented for potassium chloride in this work, the rotational spectrum of all isotopomers of potassium chloride can be predicted far into the terahertz regime with a high level of confidence for astrophysical investigations. It might be pointed out that it will be not an easy requirement, to find in circumstellar sources or in star forming regions, excitation conditions based on collisional pumping excite transitions as high as $J \geq 60$ for a molecule with a permanent electric dipole moment of ~ 10 *Debye*. It seems more likely that very specific excitation conditions, for instance line pumping, can selectively pump certain energy levels to produce an increase in higher level populations. These "unusual" excitation conditions will certainly be confined to the hot-inner cores in star formation regions. They can also be found in the central ring-regions, where the molecules are in "status

Table 5.5: Comparison of first order corrections $\Delta_{01}^{M/X}$ to the Born-Oppenheimer approximation.

Parameter	Value
Δ_{01}^{K}	$0.3628(626)$
Δ_{01}^{Cl}	$-1.28012(448)$
Δ_{01}^{Na}	-
Δ_{01}^{Cl}	$-0.84547(926)$
Δ_{01}^{Li}	$0.7355(144)$
Δ_{01}^{Cl}	$-0.389(38)$

nascendi" and presumably very hot, i.e. around 1500 K.

6

C_3H: A case of Coriolis and strong Renner-Teller Coupling

In space, carbon atoms have a strong bias to build highly unsaturated chain molecules like C_n, C_nH, C_nN, C_nS, and HC_nN which is unsaturated for even values of n. Many examples of these molecules have been found towards IRC+10216, the circumstellar envelope of a red supergiant, for instance CN, CS (Wilson *et al.* [90]), CCH (Kahane *et al.* [29]), and HC_5N, HC_7N (Winnewisser *et al.* [31]). Turner *et al.* [5] reported the detection of C_nH (with $n = 2,3,4,5,6$) and $l - C_3H_2$ in the cold molecular clouds TMC-1 and L183.

Carbon chain molecules show low-energy bending vibrational modes and, thus, are likely to be found in vibrationally excited states in some regions of space. In 1987, Cernicharo and Guélin [35] detected a number of unidentified lines towards IRC+10216 which may be assigned to vibrationally excited carbon chain molecules. Since the spectrum of a free radical in vibrationally excited states can become very complicated due to vibronic interactions between the motion of unpaired electrons and the vibrational motion of the nuclei (see Section 4.3), the assignment of interstellar lines of molecules in vibrationally excited states sometimes is difficult. The accurate knowledge of the transition frequencies from laboratory investigations is essential.
However, vibrationally excited carbon bearing species have been clearly identified by their emission spectra towards IRC+10216. In 1987 Yamamoto *et al.* [34] reported the detection of vibrationally excited C_4H. In particular, the spectral lines of the ν_7 ($^2\Pi$) bending mode of C_4H were very intense. Other examples for vibrational excitation in IRC+10216 are HCN (Ziurys *et al.* [28]) and CS (Turner *et al.* [91], [92]). Very recently, vibrationally excited cyanopolyynes have been found in the proto-planetary nebula CRL618, for instance HNC (Schilke *et al.* [93]), HC_3N (Wyrowski *et al.* [94]), and HC_5N (Pardo *et al.* [95]).
Astronomical observations of vibrationally excited molecules lead to an understanding of the excitation mechanisms which are supposed to be rather complex [96]. Thus, it is an important task for astronomers to search for

vibrationally excited states of molecules which have already been found in the ground vibrational state - especially towards sources where vibrational excitation is likely. Vibrational excitation of molecules is an indicator of high density regions and/or intense radiation field due to high excitation energies.

The formation mechanism plays a significant role for the interstellar observability of molecules. Chemical reactions with a potential energy barrier cannot take place in the interstellar medium due to the low-temperature and low-pressure conditions. Ion-neutral reactions are considered to be the most effective processes to build complex molecules from simpler ones, because there are usually no energy barriers. However, recent *abinitio* quantum chemical calculations reveal, that for many neutral-neutral reactions of radicals there are no potential barriers, either. A calculation on the neutral-neutral reaction

$$C(^3P) \; + \; C_2H_2 \; \rightarrow \; C_3H \; + \; H \tag{6.1}$$

by Takahashi and Yamashita [19] confirmed that this reaction can proceed in the interstellar medium due to the absence of a potential energy barrier. This is shown in Fig. 6.1 where the energy paths towards $l-C_3H$ (exit 1) and $c-C_3H$ (exit 2) are illustrated. The abundance of C, C_2H_2, and C_3H in dense molecular clouds cannot completely be ascribed to ion-neutral reaction paths, since neutral-neutral reactions contribute to their formation as well [97].
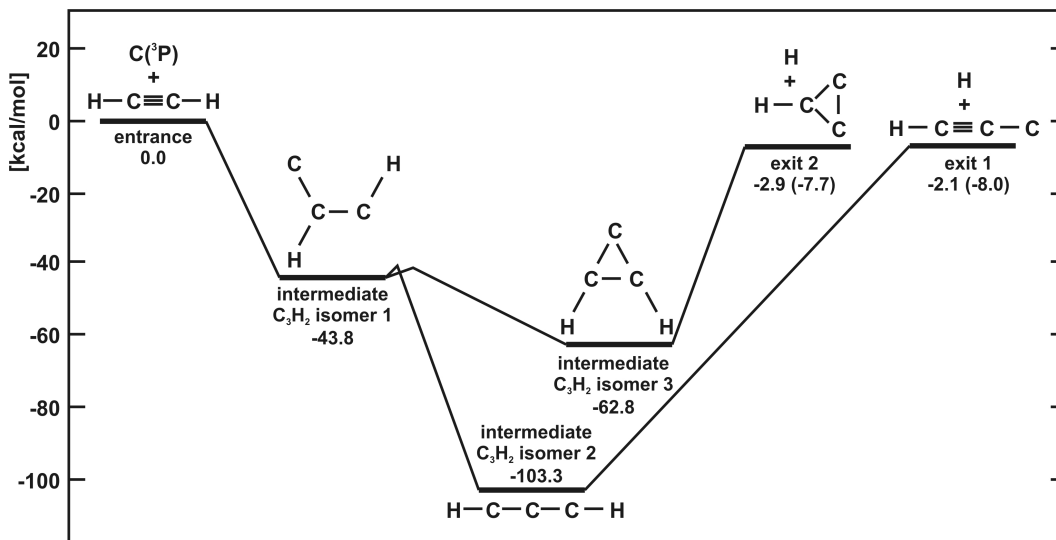
Figure 6.1: Potential energy paths of the neutral-neutral reaction $C(^3P) \; + \; C_2H_2 \; \rightarrow \; C_3H \; + \; H$ calculated by Takahashi and Yamashita [19]. The entrance energy level is set to zero. The energies of the intermediate and exit levels are given relative to the entrance level. The numbers in parentheses indicate the relative energies with zero-point energy corrections.

The propynylidyne radical, C_3H, is supposed to play a major role in the carbon chain growth in the interstellar medium and has been subject of

many astronomical investigations. Thaddeus *et al.* [4] reported the detection of linear $l-C_3H$ towards IRC+10216 and the cold dark cloud TMC-1 in its vibrational ground state in 1985. Fifteen years later, Turner *et al.* [5] detected cyclic and linear C_3H in three small translucent molecular clouds (CB 17, CB 24, and CB 228), in TMC-1, and L183. In 2004, an extensive spectral line survey towards TMC-1 was performed by Kaifu *et al.* [6]. They reported 414 lines of 27 already detected species, among them $l-C_3H$. Eleven first detections, including cyclic $c-C_3H$, have been reported by the authors.

The linear $X^2\Pi$ $l-C_3H$ radical is not only of astrophysical interest, but also a challenging molecule for spectroscopists. C_3H reveals a strong Renner-Teller coupling which shifts the $\nu_4(^2\Sigma^\mu)$ bending mode towards low energies close to the $^2\Pi$ vibrational ground state. This effect is displayed in the schematic energy level diagram in Fig. 6.2. Another interesting feature of C_3H is a Coriolis-type interaction which causes perturbations of the rotational levels in the ground and the vibrationally excited states. The $\nu_4(^2\Sigma^\mu)$ band origin has been determined due to this effect.
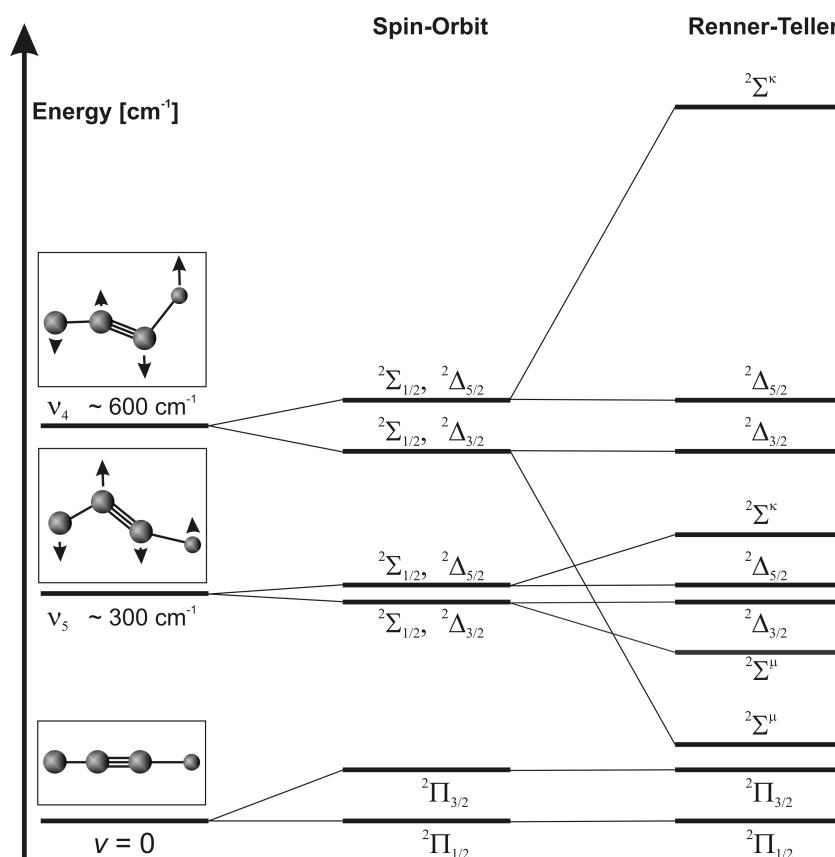
Figure 6.2: Schematic energy level diagram of C_3H. Each energy level is split into two substates due to the spin-orbit interaction. The degeneracy of the ν_4 and the ν_5 vibrational state ($^2\Sigma$- and $^2\Delta$-component) is lifted by a strong Renner-Teller effect which takes into account the interaction between the vibrational motion and the electronic orbital angular momentum. The $^2\Sigma^\mu$-component is shifted towards lower energies and close to the $^2\Pi_{3/2}$ vibrational state (< 13 cm^{-1}).

After its discovery in the interstellar medium, the first laboratory analysis of the linear C_3H radical was published by Gottlieb et al. [7], [8] in 1985 and 1986 for the ground vibrational $^2\Pi_{1/2}$-state ($< 362\ GHz$) and $^2\Pi_{3/2}$-state ($< 377\ GHz$). Yamamoto *et al.* [9] observed the vibrationally excited rotational spectral lines of C_3H and C_3D in the $\nu_4(^2\Sigma^\mu)$ state up to 359 GHz and considered the Coriolis-type interaction between the $^2\Pi$ and the $^2\Sigma$ state. They also carried out a search for vibrationally excited rotational transitions towards IRC+10216 which was unfortunately negative.

Theoretical studies on C_3H by Kanada *et al.* [17], Ding *et al.* [18], and Takahashi *et al.* [19], [98] revealed its equilibrium geometric structure and provided vibrational frequencies. The spin-orbit coupling constant (Cooper [36]) and the hyperfine parameters (Green [37] and Pauzat *et al.* [20]) have also been determined from *ab initio* calculations. The recent publication by Perić *et al.* [21] tries "to solve the controversies concerning the vibronic spectrum of $CCCH$". Inter alia the handling of the Renner-Teller effect with a variational method and its application for the $X^2\Pi$ state of C_3H is presented in their work.
The dipole moment for the linear C_3H in both the $^2\Pi$ and $^2\Sigma$ state was obtained by Takahashi [98] in an *ab initio* quantum chemical calculation. He determined a value of 3.29 D. The vibrational transition dipole moment is assumed to be 0.5 D [13]. Thus, rotational and vibrational transitions are observable with adequate intensities in laboratory investigations.

In the course of this thesis, the $\nu_4(^2\Sigma^\mu)$ CCH bending vibration of the C_3H radical has been observed for the first time. Due to a strong Renner-Teller effect the bending transitions occur in the submillimeter wavelength region. The $\nu_4 = 1$ state, originally located at about $600cm^{-1}$, is split into four substates $^2\Delta_{5/2}$, $^2\Delta_{3/2}$, $^2\Sigma^\kappa$, and $^2\Sigma^\mu$ of which the latter is only 610 GHz (20.35 cm^{-1}) above the average $^2\Pi$-ground state (see Fig. 6.2). In particular, the ν_4-bending transitions with $J = 25.5 \leftarrow 24.5$, which are strongly perturbed by Coriolis interaction, have been accurately measured. The frequency range of pure rotational transitions, which have been investigated in the two vibrational ground states ($^2\Pi_{1/2}$, $^2\Pi_{3/2}$) and in the vibrationally excited state ($\nu_4 = 1$, $^2\Sigma^\mu$), has been extended up to 600 GHz.
From a least squares fit to a standard Hamiltonian the set molecular parameters for C_3H has been refined and extended by three constants. These parameters allow most reliable frequency predictions in the terahertz region. All data is accessible in the Cologne Database for Molecular Spectroscopy, CDMS (via http://www.cdms.de) [41], [13].

6.1   Experimental

The linear C_3H radical is produced in the 50 Hz pulsed electrical discharge of a gas mixture of 1.5–2.3 % C_2H_2, 63–44 % CO diluted in He at a backing pressure of 1–6 bar. The discharge takes place in the throat of the slit nozzle.

C_3H detection takes place in the zone of silence of the adiabatically expanding gas. The pressure within the vacuum chamber is kept below $3 \cdot 10^{-2}$ *mbar*. A 200–250 μs gas pulse, followed by a 250–350 μs discharge pulse of 800–1100 *V* is found to deliver highest yields of C_3H. The discharge current is typically between 600 and 900 *mA*. The data acquisition is taken within a 100 μs time frame at the end of the discharge pulse. The integration time for background subtraction is 400 to 500 μs long and starts about 100 μs after the trigger. The on-off modulation in combination with a $2f$-modulation has substantial impact on the signal-to-noise ratio and at the same time suppresses standing wave etalon effects.

The microwave beam probes the molecular jet approximately 5 *cm* downstream and perpendicular to the direction of jet propagation to avoid line shifts caused by the Doppler effect. A multipath optics, consisting of a concave mirror (focal length 7.5 *cm*) and of a plain mirror at a distance of 7.5 *cm*, enables 6 passes with an overall absorption path length of approximately 30 *cm*.

6.2   Measurements
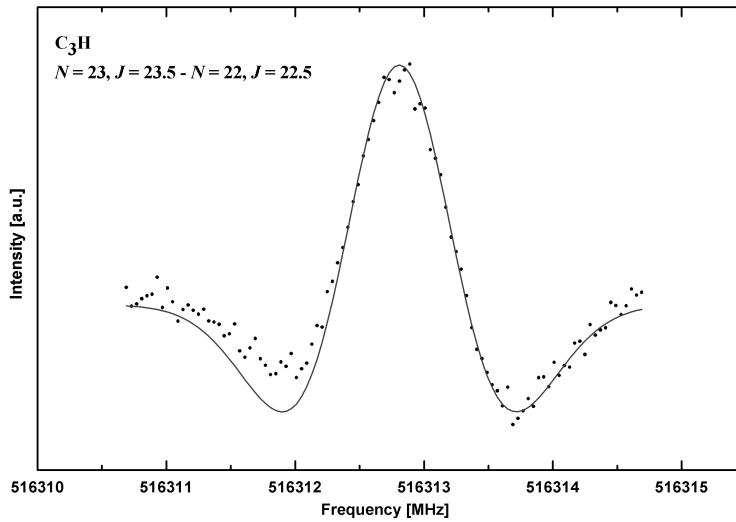
Figure 6.3: The $N = 23$, $J = 23.5 \leftarrow N = 22$, $J = 22.5$ pure rotational transition of C_3H in the $^2\Pi_{1/2}$-band. The the measured spectrum is represented by dots; the line indicates the fitted function.

In this work, eight transitions of the $^2\Sigma^\mu$-$^2\Pi_{3/2}$ band system have been measured with high accuracy. Furthermore, 14 pure rotational transitions of the $^2\Pi_{1/2}$-band, 16 transitions of the $^2\Pi_{3/2}$-band in the vibrational ground state, and 13 lines in the vibrational excited $^2\Sigma^\mu$ state have been recorded,
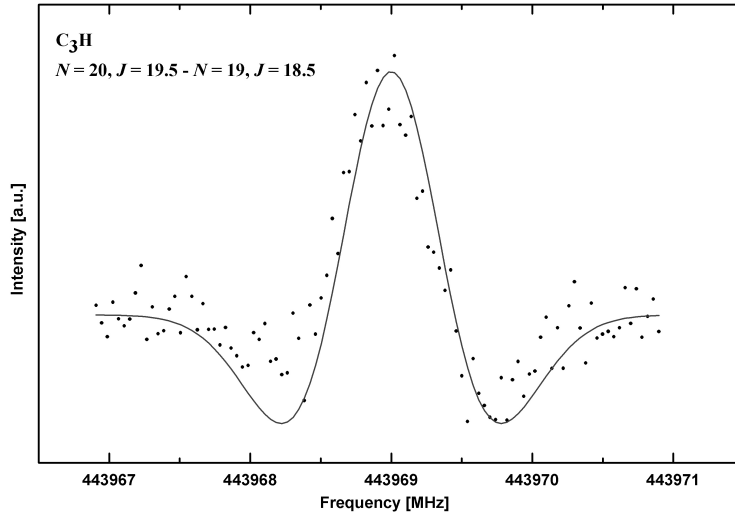
Figure 6.4: The $N = 20$, $J = 19.5 \leftarrow N = 19$, $J = 18.5$ pure rotational transition of C_3H in the $^2\Pi_{3/2}$-band.

in continuation to earlier works (e.g. Yamamoto *etal.* [9]). The hyperfine splitting has been resolved for ten lines, in particular for the transitions near the $\nu_4 = 1$ / $\nu = 0$ crossing, due to Coriolis interaction (see Fig. 6.7). A frequency range from 370 to 600 *GHz* has been covered. Typical line profiles are shown in Figs. 6.3-6.6. The line indicates the second derivative of the Gaussian function which has been fitted to the measured spectrum represented by dots. The spectra of transitions of the $^2\Sigma^\mu$-$^2\Pi_{3/2}$ band system show smaller signal to noise ratios than the pure rotational spectra, since their intensities are weaker. The $\nu_4 = 0$, $J = 25.5$, $F = 26 \leftarrow \nu_4 = 1$, $J = 24.5$, $F = 25$ transition of Fig. 6.6 was located on the rising edge of a strong absorption line and, thus, shows a large asymmetry. The complete list of the experimental data and the associated uncertainty is given in Appendix B.

The accuracy of the center frequency of the lines ranges between 20 and 80 *kHz* and in some cases exceeds 100 *kHz*. The accuracy essentially depends on three factors:

  (i) line width

 (ii) signal to noise ratio

(iii) baseline variations

(iv) Doppler-shifts

The line width is basically caused by Doppler-broadening and partially by the $2f$-modulation of the probing radiation. A typical value is 900 *kHz* at a
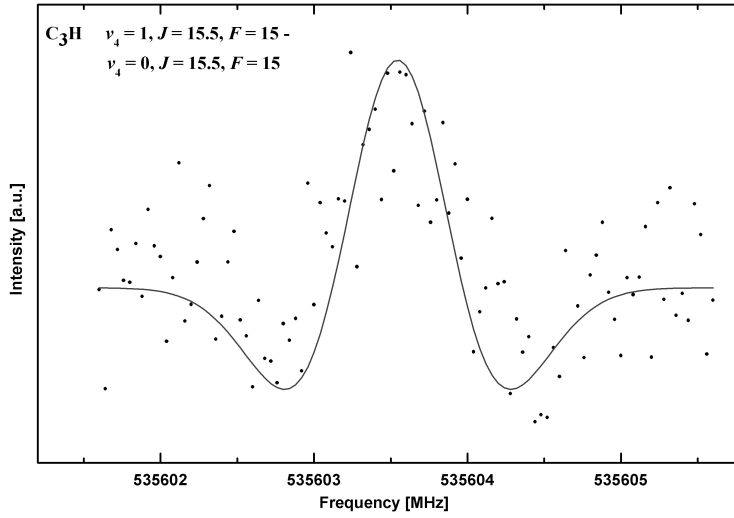
Figure 6.5: $\Delta F = 0$ component of the $v_4 = 1$, $J = 15.5$, $F = 15$ $\leftarrow$ $v_4 = 0$, $J = 15.5$, $F = 15$ bending vibrational transition of C_3H of the $^2\Pi_{3/2}$-$^2\Sigma^\mu$ band system.

center frequency of 500 GHz.

A high signal-to-noise ratio is also of crucial importance for accurate determination of the line position and the experimental error is directly correlated to this ratio.

Baseline effects are basically suppressed by the on-off modulation due to the pulsed molecular source.

Doppler-shifts may occur if the probing microwave beam intersects the jet not perpendicular to the direction of propagation. Small deviations from a 90° angle in the used setup result in a slight blue shift of the center frequency. Thus, frequency calibrations are necessary, for instance with well known transitions of CO.

All spectra were recorded twice or four times, first with ascending frequency and subsequently with descending frequency. The signal was averaged 100–150 times at each frequency step of 20–40 kHz. The total integration time was typically 0.5 to 1 minute for each scan direction, finally the spectra were added. The lines were recorded in the $2f$-modulation mode (see Section 3.1.4).

6.3   Analysis

A least squares fit has been applied to the set of measured lines including the data from Gottlieb *et al*. [8] and Yamamoto et al. [9]. The astronomically detected transition frequencies in the 32 GHz region reported by Kaifu et
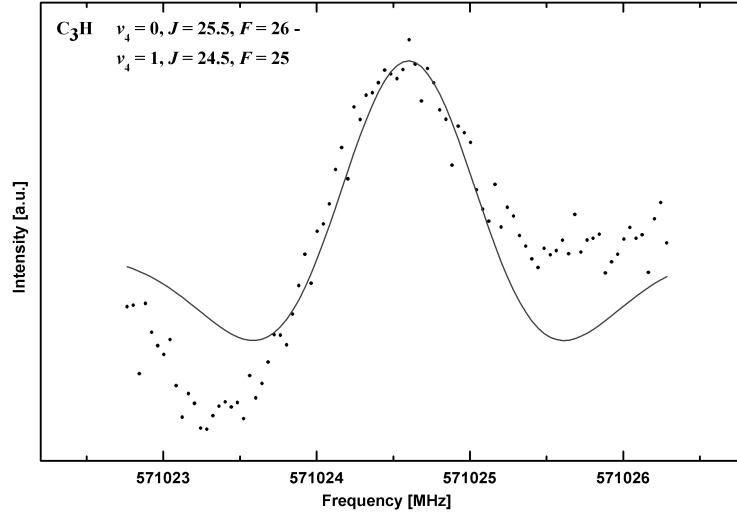
Figure 6.6: $\Delta F = 1$ component of the $v_4 = 0$, $J = 25.5$, $F = 26 \leftarrow v_4 = 1$, $J = 24.5$, $F = 25$ bending vibrational transition of C_3H of the ${}^2\Sigma^{\mu}$-${}^2\Pi_{3/2}$ band system.

al. [6] have been used to extend the pure rotational data. The rotational constant B, the centrifugal distortion term D, the electronic spin rotation interaction constant γ, the Fermi-contact interaction parameter b_F, and the dipole-dipole coupling constant c have been determined for both the vibrational ground and excited state from a fit using the Pickett program [86]. The Λ-type and l-type doubling constants p, p_D, and q, the nuclear spin-orbit interaction parameter a, the hyperfine Λ-type doubling constant d, and the electronic spin-orbit interaction term A_{SO} have also been derived from the fit for the ${}^2\Pi$ vibrational ground state. The distortion parameter of γ was only determinable in case of the vibrationally excited state. Compared to Yamamoto's parameter set, three further constants had to be included in the fit, i.e. the centrifugal distortion constant H for the ground vibrational state, the distortion parameter of the l-type doubling constant q for the vibrationally excited state, and the distortion constant of the Coriolis interaction term (G_{CD}). The centrifugal distortion constant H for the ${}^2\Sigma$ state and γ_D for the ${}^2\Pi$ state were insignificantly determined with the present data set and were omitted from the final fits.

All lines listed in Appendix B were included into the fit, if not indicated otherwise. The uncertainties of the lines of Gottlieb and Yamamoto were set to 50 kHz. Two lines observed by Yamamoto, belonging to the quantum number $J = 15.5 \leftarrow 14.5$ and frequencies 339263.251 MHz and 339688.210 MHz, were omitted from the final fit because their observed minus calculated value exceeded 3σ. The RMS-value of our fit was ~ 0.9. The molecular parameters are given in Table 6.1 and have been compared to the data of Yamamoto *et al.* [9].

Table 6.1: Spectroscopical parameters of C_3H.

Parameters [MHz]	This work	Yamamoto *et al.* [9]
	Ground state ($^2\Pi$)	
B	11189.0979(86)	11189.052(48)
$D \cdot 10^3$	5.2263(130)	5.1365(50)
$H \cdot 10^6$	0.02274(196)	–
A_{SO}	432795.6(85)	432834.0(310)
γ	−48.163(119)	−48.57(126)
p	−7.00685(252)	−7.0842(97)
$p_D \cdot 10^3$	0.596(142)	1.41(74)
q	−13.0046(106)	−13.057(67)
$q_D \cdot 10^3$	0.1284(228)	–
a	12.323(155)	12.33(23)
b_F	−13.682(98)	−13.38(70)
c	28.09(32)	27.49(97)
d	16.25776(284)	16.241(27)
	Vibrationally excited state v_4 ($^2\Sigma^\mu$)	
E_{v4}	609977.1(42)	610197.0(12300)
B	11212.6808(165)	11212.764(96)
$D \cdot 10^3$	4.8813(232)	5.0066(85)
γ	−35.5173(247)	−35.454(96)
$\gamma_D \cdot 10^3$	0.640(157)	1.45(79)
b_F	1.456(137)	1.4(28)
c	27.21(49)	28.5(26)
	Coriolis interaction	
$G_C = 2 \cdot \beta$	−2466.0(37)	−2448.0(2460)
G_{CD}	0.0345(59)	–

The representation for C_3H distinguishes between the folowing two cases:

$$1) \quad 2B\left(J - \frac{1}{2}\right)\left(J + \frac{1}{2}\right) < A_{SO} \qquad (6.2)$$

$$2) \quad 2B\left(J - \frac{1}{2}\right)\left(J + \frac{1}{2}\right) > A_{SO} \qquad (6.3)$$

States belonging to the first case where $J + \frac{1}{2} = N$ belong to a $^2\Pi_{1/2}$ state, while the states where Eq. 6.3 is valid belong to a $^2\Pi_{3/2}$ state. For the values presented here for the spin-orbit coupling constant and for the rotational constant, one derives a J of approximately 4.5 for this turning point. Therefore, all lines in this work with $J + \frac{1}{2} = N$ belong to a $^2\Pi_{3/2}$-state, and vice versa.

6.4   Discussion and Conclusion

The present work extends the previous investigations of pure rotational transitions ([8], [9]) by 44 lines up to 600 *GHz* within the $^2\Pi_{1/2}$-band, $^2\Pi_{3/2}$-band, and in the vibrational excited $^2\Sigma^\mu$ state. Due to these measurements the accuracy of the rotational constant B has been improved by a factor of five. The observed high J transitions required the inclusion of the well determined centrifugal distortion constant H in the fit.

Eight lines have been assigned to ro-vibrational transitions of the v_4 $\left(^2\Sigma^\mu\right)$ *CCH* bending mode which has been observed for the first time. From these measurements, the accuracy of the excitation energy E_{v4} has been strongly improved by a factor of almost 300. This is the first accurate value for E_{v4} compared to uncertainties of more than 1 *GHz* in the work published by Yamamoto *etal.* [9].
Furthermore, the accuracy of the spin-orbit interaction constant A_{SO} has been improved by a factor of four due to the observed ro-vibrational transitions.
Another great progress has been made concerning the Coriolis interaction. The uncertainty of the associated constant has been reduced by factor of 65 and a value of -2466.0(37) *MHz* for $G_C = 2 \cdot \beta$ has been determined. Yamamoto derived an interaction term of $\beta = -1224(123)$ *MHz* which is half of G_C. The sign of G_C is not relevant for the fit and therefore not well defined. However, in combination with the signs and magnitudes of the transition and permanent dipole moments, it is important for the intensities of some strongly perturbed lines. The negative sign of G_C in this work follows the notation of Yamamoto *et al.* [9]. The strongest Coriolis interaction occurs at energies around 261.5 cm^{-1} at $J = 24.5$ and 25.5, as can be seen in Fig. 6.7. The Coriolis interaction only effects levels with the same J quantum number, $J \pm \frac{1}{2} = N$. Fig. 6.8 displays the Fortrat diagram of the $v_4 = 1$ $\left(^2\Sigma^\mu\right)$ and the $v_4 = 0$ $\left(^2\Pi_{3/2}\right)$ states. Here the J quantum numbers are plotted against an effective rotational constant $B_{eff} = \frac{B}{2J}$. As can be seen easily, the strongest

perturbation of B occurs at $J = 25.5$.

The Renner-Teller coupling constant is estimated to be about 0.9. To obtain this value in a fit, infrared measurements of the $^2\Sigma^\kappa$-$^2\Pi_{3/2}$ or $^2\Sigma^\kappa$-$^2\Pi_{1/2}$ band system would be necessary which will be performed with the modified Cologne Carbon Cluster experiment [99].

All parameters obtained in this work, except the centrifugal distortion constant D, have lower uncertainties than those published in earlier works, for instance in the publication by Yamamoto *et al.* [9]. They are very reliable for frequency predictions up to $1\,THz$. In particular the uncertainties of transitions near the $v_4 = 1$ / $v = 0$ crossing (see Fig. 6.7) decreased from several $10\,MHz$ to a few $10\,kHz$ compared to the predictions based on the parameter set of Yamamoto *et al.* The precise knowledge of the excitation energy E_{v4} encourages further searching for ro-vibrational bending transitions of C_3H in the interstellar and circumstellar medium. C_3H is a prime example of how astrophysical observations can trigger laboratory investigations and new laboratory detections can facilitate a new field of astronomical investigation, in return.

J $v = 0$, $^2\Pi_{1/2}$ **J $v = 0$, $^2\Pi_{3/2}$**   **$v_4 = 1$, $^2\Sigma^\mu$ N**

27.5 $\dfrac{311.2 \text{ cm}^{-1}}{0.899}$ $\dfrac{309.8 \text{ cm}^{-1}}{0.932}$ 27

28.5 $\dfrac{307.2 \text{ cm}^{-1}}{0.912}$

26.5 $\dfrac{291.0 \text{ cm}^{-1}}{0.778}$ $\dfrac{289.6 \text{ cm}^{-1}}{0.868}$ 26

27.5 $\dfrac{286.6 \text{ cm}^{-1}}{0.905}$

25.5 $\dfrac{271.0 \text{ cm}^{-1}}{0.612}$ $\dfrac{270.4 \text{ cm}^{-1}}{0.695}$ 25

26.5 $\dfrac{266.1 \text{ cm}^{-1}}{0.903}$

24.5 $\dfrac{251.0 \text{ cm}^{-1}}{0.577}$ $\dfrac{252.0 \text{ cm}^{-1}}{0.625}$ 24

25.5 $\dfrac{246.9 \text{ cm}^{-1}}{0.894}$

23.5 $\dfrac{232.6 \text{ cm}^{-1}}{0.764}$ $\dfrac{233.9 \text{ cm}^{-1}}{0.845}$ 23

24.5 $\dfrac{227.9 \text{ cm}^{-1}}{0.891}$

22.5 $\dfrac{214.8 \text{ cm}^{-1}}{0.827}$ $\dfrac{216.6 \text{ cm}^{-1}}{0.927}$ 22

23.5 $\dfrac{210.2 \text{ cm}^{-1}}{0.882}$

   $\dfrac{27.2 \text{ cm}^{-1}}{1.000}$ 0

1.5 $\dfrac{14.8 \text{ cm}^{-1}}{0.708}$

0.5 $\dfrac{0.0 \text{ cm}^{-1}}{1.000}$
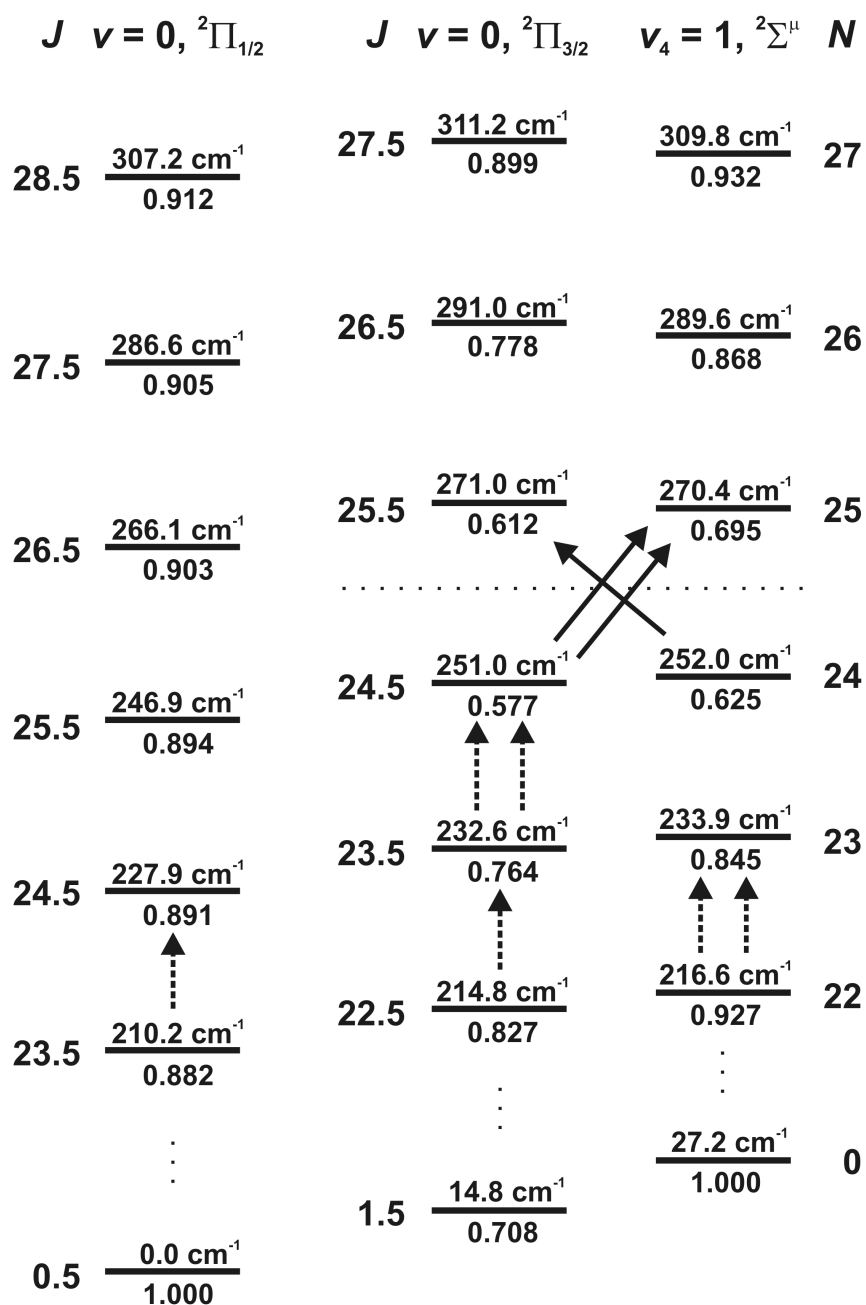
Figure 6.7: C_3H transitions near the $v_4 = 1 \, / \, v = 0$ crossing. The total energies E in wavenumbers are given above the line, indicating the level's position; the mixing coefficients c^2 are given beneath this line. The Coriolis interaction only affects levels with the same J quantum number, $J = N \pm \frac{1}{2}$. The pure rotational transitions observed within the states are indicated by dashed arrows while transitions between the states are indicated by solid arrows. Two arrows denote those transitions where hyperfine structure has been resolved. The dotted line marks the position of the crossing at approximately 261.5 cm^{-1}.
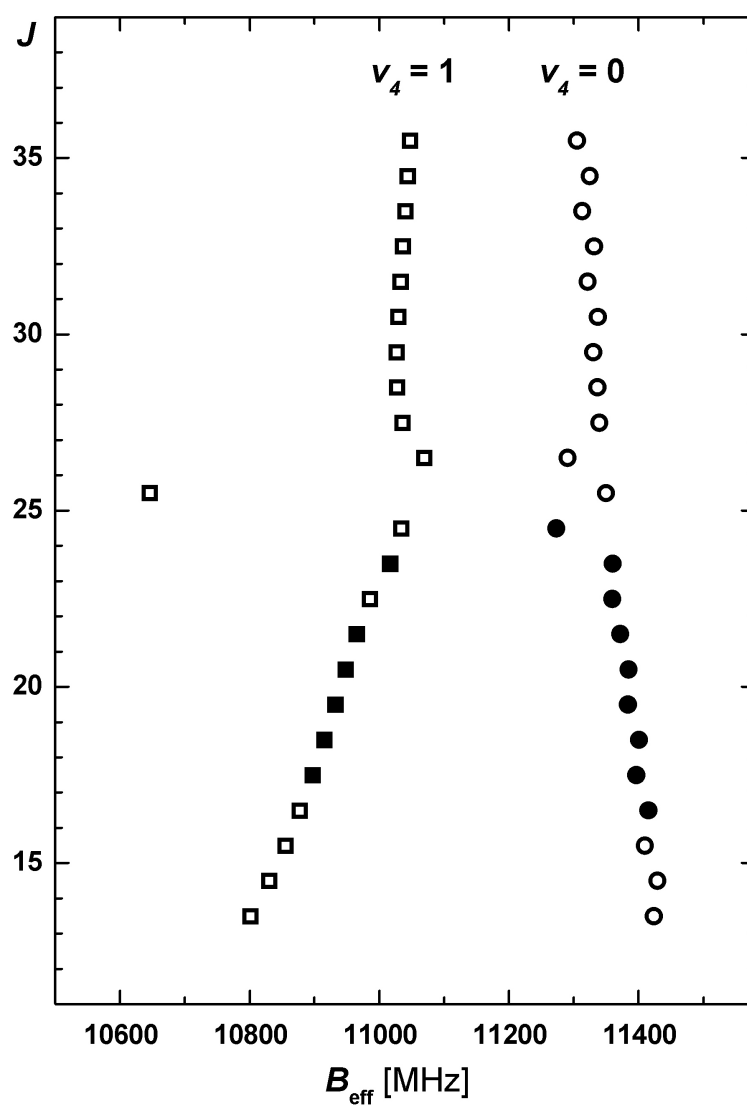
Figure 6.8: Fortrat diagram of $v_4 = 1$ ($^2\Sigma^\mu$) (squares) and $v_4 = 0$ ($^2\Pi_{3/2}$) (circles) states. Solid squares and circles indicate observed transitions. The strongest perturbation of the effective B values occurs at $J = 25.5$.

7

CO^+: Ion Production with SuJeSTA

Molecular ions are supposed to play a significant role in the interstellar chemistry through ion-neutral reactions. There is general agreement that these reactions produce a wide variety of molecules and many examples were investigated (e.g. Langer and Graedel [100]). Although CO is the most abundant heavy interstellar molecule, for a long time only the carbon bearing ions CH^+ (Hobbs [101] [102]), HCO^+ (Huggins *et al*. [103]), $HOCO^+$, and HCS^+ (Thaddeus *et al*. [104]) had been detected. The interstellar abundance of CO^+ compared to other ions is low due to its high reactivity (e.g. with H_2 to HCO^+). Therefore, it is usually optically thin. The first detection of CO^+ towards OMC-1, a molecular cloud in the Orion nebula, was reported by Erickson *et al*. [12] in 1981. They derived a column density for CO^+ of $2 \cdot 10^{12}$ cm^{-2}. Latter *et al*. [38] observed CO^+ in the planetary nebula NGC7027 and in the interstellar medium (M17SW) twelve years later.

Due to its low optical depth CO^+, together with C and C^+, are important tracers for PDRs (Photon Dominated Region). The knowledge of the CO^+ column density provides information about the structure of PDRs. Recent observations show that interstellar molecular clouds and star forming regions are inhomogeneous. The dense regions of molecular clouds, illuminated by far-ultraviolet radiation, can be investigated by the emission spectra of ions. This was done by Störzer *et al*. [11] in star forming regions of the Orion Bar. The CO^+ emission spectra origin at the exterior surfaces of photon dominated dense molecular clouds.

CO^+ has to be classified as a $^2\Sigma$ radical from the spectroscopist's point of view . The dipole moment of CO^+ is 2.77 D, about 30 times larger than that of CO. The $^{13}C^{16}O^+$ and $^{12}C^{17}O^+$ reveal a hyperfine splitting due to the nuclear spins of ^{13}C ($I = 1/2$) and ^{17}O ($I = 5/2$).
Many laboratory studies in the microwave region were dedicated to CO^+ in the 1970s and 1980s, for example Dixon and Woods [39], Sastry *et al*. [22], van den Heuvel *et al*. [105], Piltch *et al*. [40], and Bogey *et al*. [23]. The two latter observed the transitions of four isotopomers of CO^+, i.e. $^{12}C^{16}O^+$, $^{13}C^{16}O^+$, $^{12}C^{18}O^+$, and $^{13}C^{18}O^+$, which were fitted to a set of mass reduced

Dunham parameters. Bogey *et al*. were also able to resolve the hyperfine structure for $^{13}C^{16}O^+$ and $^{13}C^{18}O^+$. A very recent extensive research in the field of the isotopomers $^{12}C^{16}O^+$ and $^{13}C^{16}O^+$ in the terahertz domain was carried out by Klapper [10] employing the Cologne Terahertz Spectrometer. The vibrationally ground states of both isotopomers were investigated up to 1 *THz*.

One goal of the present work is to facilitate the analysis of adiabatically cooled ions in the terahertz region. The new Supersonic Jet Spectrometer for Terahertz Applications (SuJeSTA) has been developed for this purpose, besides the investigation of radicals. First test measurements on CO^+ have been performed to probe the ability of the new spectrometer to produce ions in a pulsed discharge with subsequent supersonic expansion.
In addition, a revised mass independent least squares fit has been performed. The isotopically invariant mass-reduced Dunham parameters and the first order Born-Oppenheimer breakdown corrections for *C* and *O* have been determined, resulting in a consistent set of constants for CO^+.

7.1   Experimental

CO^+ ions are produced in the pulsed electrical discharge of a gas mixture of 30–50 % *CO*, diluted in *Ar* at a backing pressure of 1–6 *bar*. The discharge is placed in the throat of the nozzle. Either the slit nozzle or the pinhole nozzle are used for ion production. The detection of the CO^+ takes place in the zone of silence of the adiabatically expanding gas. Argon seems to act as a catalyst for the ionization of carbon monoxide, since both ionization energies are very similar ($E_{ion}^{Ar} = 15.76\ eV$ and $E_{ion}^{CO} = 14.09\ eV$). Dilution with *He* does not yield in a measurable amount of CO^+. A 200–250 μs gas pulse, followed by a 250–350 μs discharge pulse of 800–1100 *V* is found to produce CO^+ in sufficient amounts. The discharge current is typically between 600 and 900 *mA*. The data acquisition is taken within a 100 μs time window at the end of the discharge pulse. The integration time for background subtraction is 400 to 500 μs long and starts about 100 μs after the trigger. These values are very similar to the production conditions for C_3H (see Section 6.1). The microwave radiation is provided by BWOs. The measurements have been carried out with the 6 pathes and the 16 pathes setup described in Section 3.1.2.

7.2   Measurements

Two transitions of CO^+ have been measured with the SuJeSTA within the scope of this work. The spectral line at 471679 *MHz* has been recorded with a BWO and the 6 pathes optics. A synthesizer at its fundamental frequency and the 16 pathes setup have been used to detect the transition at
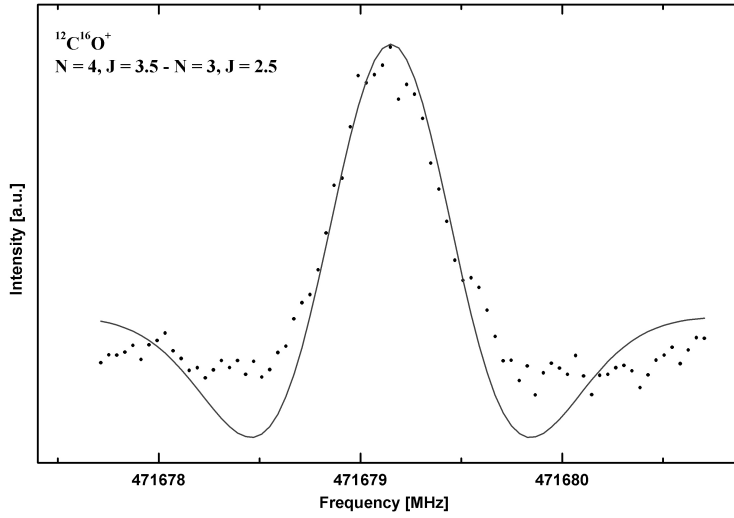
Figure 7.1: Spectrum of a pure rotational transition of CO^+ in the ground vibrational state with quantum numbers: $N = 4$, $J = 3.5 \leftarrow N = 3$, $J = 2.5$. The the measured spectrum is represented by dots; the line indicates the fitted function.

117692 *MHz*. These two lines have basically been used for test purposes to verify the ion production and detection of SuJeSTA. The spectra are shown in Figs. 7.1 and 7.2. The line shape is the second derivative of the Gaussian function which has been fitted to the measured spectrum represented by dots. The complete list of the experimental data including former submillimeter and millimeter data is given in Appendix C.

7.3   Analysis

The newly recorded lines together with the previously measured microwave spectra of Klapper [10], Bogey *et al*. [23], Sastry *et al*. [22], and Heuvel *et al*. [105] were subjected to a least squares fit with an RMS-error of approximately 0.74. The mass invariant Dunham parameters U_{ij} and the Born-Oppenheimer breakdown corrections Δ_{01} have been determined, according to the formalism described in Section 4.2.2. In this fit the parameter U_{03} has been constrained with respect to U_{02}. Therefore, no error is given for the value of U_{03}. Additionally, the isotopically invariant electronic spin rotation interaction constants G_{00}, G_{10}, and G_{20}, the mass independent Fermi-contact interaction parameter b_{F00}, and the invariant dipole-dipole coupling constant c_{00} have been determined for CO^+ from the fit. The results of this isotopically invariant study for CO^+ are listed in Tab. 7.1.

In Tab. 7.2 the derived values of the Dunham parameters Y_{10}, Y_{01}, Y_{11}, Y_{21}, Y_{02}, and Y_{03} are presented. Furthermore the equilibrium moment of
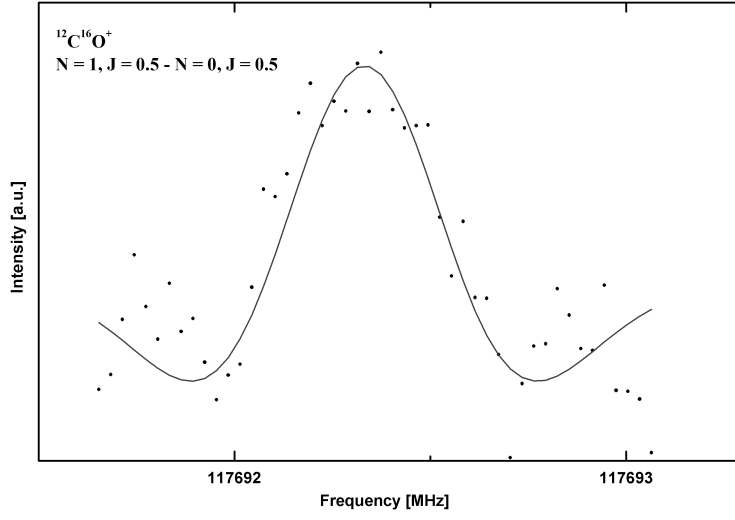
Figure 7.2: Spectrum of a pure rotational transition of CO^+ in the ground vibrational state with quantum numbers: $N = 1$, $J = 0.5 \leftarrow N = 0$, $J = 0.5$.

inertia I_e^{inv} and the equilibrium nuclear distance r_e^{inv} have been calculated from the U_{01} including the Born-Oppenheimer corrections. The parameters I_e^{BO} and r_e^{BO} have been derived under the assumption of the correctness of the Born-Oppenheimer approximation.

Table 7.1: Isotopically independent parameters for the carbon monoxide ion and the first order corrections to the Born-Oppenheimer approximation for U_{01}.

Parameter	Value	Unit
U_{01}	406377.160(638)	$MHz \cdot amu$
Δ_{01}^{C}	$-2.794(126)$	
Δ_{01}^{O}	$-7.413(212)$	
U_{11}	$-2551.470(107)$	$MHz \cdot amu^{3/2}$
U_{21}	$-2.7182(270)$	$MHz \cdot amu^{2}$
U_{02}	$-8.90235(197)$	$MHz \cdot amu^{2}$
$U_{03} \cdot 10^{4}$	8.821147	$MHz \cdot amu^{3}$
G_{00}	1875.098(391)	$MHz \cdot amu$
G_{10}	$-3.815(557)$	$MHz \cdot amu^{3/2}$
G_{20}	$-1.131(125)$	$MHz \cdot amu^{2}$
c_{00}	150.26(239)	MHz
b_{F00}	1526.47(99)	MHz

Table 7.2: Derived parameters and structural constants of four isotopomers of CO^+.

Parameters	$^{12}C^{16}O^+$	$^{13}C^{16}O^+$	$^{12}C^{18}O^+$	$^{13}C^{18}O^+$	Unit
Y_{10}	2211.90335(140)	2162.61392(120)	2158.47422(123)	2107.93474(105)	cm^{-1}
Y_{01}	59267.513(132)	56654.939(121)	56438.692(125)	53826.100(114)	MHz
Y_{11}	-142.12300(595)	-132.82888(556)	-132.06989(553)	-123.00544(515)	MHz
Y_{21}	-0.057825(575)	-0.052839(525)	-0.052437(521)	-0.047694(474)	MHz
Y_{02}	-0.1893810(420)	-0.1730509(384)	-0.1717338(381)	-0.1562007(346)	MHz
$Y_{03} \cdot 10^6$	2.73698851	2.39072307	2.36347966	2.05018407	MHz
I_e^{inv}	852.70663(190)	892.02816(191)	895.44601(198)	938.90885(199)	$amu \cdot \text{Å}^2$
r_e^{inv}	11.1521300(854)	11.1520000(857)	11.1521219(888)	11.1520922(893)	Å
I_e^{BO}	852.65055(134)	891.97424(140)	895.38836(141)	938.85340(147)	$amu \cdot \text{Å}^2$
r_e^{BO}	11.1517629(600)	11.1517629(628)	11.1517629(630)	11.1517629(661)	Å

7.4   Discussion and Conclusion

Primarily, the measurements of CO^+ proved the successful ion production with SuJeSTA and further investigations on CO^+ and other ions are now conceivable.

An updated isotopically invariant analysis of CO^+ including the Born-Oppenheimer breakdown corrections has been performed. This analysis of CO^+ reveals that the strict validity of the Born-Oppenheimer approximation is not an appropriate description for carbon monoxide ions. The differences in the nuclear distances r_e^{inv} for different isotopomers are larger than the uncertainties and therefore are not negligible. The deviation of r_e^{inv} from r_e^{BO} ($\sim 2 \cdot 10^{-6}$ Å) results in an increase of approximately $2 \cdot 10^{-3}$ amu·Å of the angular momentum I_e^{inv} compared to I_e^{BO}.

The Δ_{01}^C and Δ_{01}^O are of the same order of magnitude as U_{02} and are very well defined. The absolute value of the Δ_{01}^C is about three times larger in magnitude than Δ_{01}^O.

The isotopically invariant parameters G_{00}, G_{10}, G_{20}, b_{F00}, and c_{00} are well determined.

On the basis of the new parameter set presented in this work, the rotational spectra of four isotopomers of CO^+ are predictable with high accuracy. The transition frequency predictions for the isotopomers $^{12}C^{16}O^+$, $^{13}C^{16}O^+$, $^{12}C^{18}O^+$, and $^{13}C^{18}O^+$ in the vibrational ground state are presented in Tabs. 7.3–7.6. The transition intensities are given for a temperature of 300 K. The reliable data, which is also available via the Cologne database CDMS [13], encourages further observations of the rotational transitions of less abundant isotopomers of CO^+ in the interstellar and circumstellar medium.

Table 7.3: Transition frequency predictions for $^{12}C^{16}O^+$ up to 1 THz in the vibrational ground state.

N'	J'	N''	J''	Frequency [MHz]	$\Delta\nu$ [MHz]	$log(I)$ [nm^2MHz]	E_{lower} [cm^{-1}]
1	0.5	0	0.5	117692.349	0.018	−3.543	0.000
1	1.5	0	0.5	118101.800	0.010	−3.239	0.000
2	1.5	1	1.5	235380.152	0.036	−3.351	3.940
2	1.5	1	0.5	235789.604	0.015	−2.651	3.926
2	2.5	1	1.5	236062.572	0.014	−2.395	3.940
3	2.5	2	2.5	353058.869	0.053	−3.212	11.814
3	2.5	2	1.5	353741.289	0.019	−2.064	11.791
3	3.5	2	2.5	354014.257	0.018	−1.908	11.814
4	3.5	3	3.5	470723.960	0.070	−3.121	23.622
4	3.5	3	2.5	471679.347	0.022	−1.688	23.590
4	4.5	3	3.5	471952.315	0.021	−1.574	23.622
5	4.5	4	4.5	588370.891	0.087	−3.063	39.365
5	4.5	4	3.5	589599.247	0.025	−1.418	39.324
5	5.5	4	4.5	589872.215	0.025	−1.329	39.365
6	5.5	5	5.5	705995.140	0.104	−3.030	59.041

Table 7.3: Transition frequency predictions for $^{12}C^{16}O^+$ - continued.

N'	J'	N''	J''	Frequency [MHz]	$\Delta\nu$ [MHz]	$log(I)$ [nm^2MHz]	E_{lower} [cm^{-1}]
6	5.5	5	4.5	707496.463	0.031	-1.216	58.991
6	6.5	5	5.5	707769.431	0.031	-1.142	59.041
7	6.5	6	6.5	823592.189	0.124	-3.017	82.650
7	6.5	6	5.5	825366.480	0.044	-1.061	82.590
7	7.5	6	6.5	825639.448	0.043	-0.998	82.650
8	7.5	7	7.5	941157.536	0.147	-3.021	110.190
8	7.5	7	6.5	943204.796	0.064	-0.944	110.122
8	8.5	7	7.5	943477.764	0.064	-0.889	110.190

Table 7.4: Transition frequency predictions for $^{13}C^{16}O^+$ up to 1 THz in the vibrational ground state.

N'	J'	F'	N''	J''	F''	Frequency [MHz]	$\Delta\nu$ [MHz]	$log(I)$ [nm^2MHz]	E_{lower} [cm^{-1}]
1	1.5	1	0	0.5	1	111226.972	0.974	-5.211	0.013
1	0.5	0	0	0.5	1	112465.976	0.083	-3.883	0.013
1	0.5	1	0	0.5	1	112695.147	0.042	-3.412	0.013
1	1.5	1	0	0.5	0	112753.437	0.016	-3.411	-0.038
1	1.5	2	0	0.5	1	112902.472	0.013	-3.181	0.013
1	0.5	1	0	0.5	0	114221.612	0.977	-5.187	-0.038
2	1.5	2	1	1.5	2	223829.359	0.949	-4.478	3.779
2	1.5	2	1	0.5	1	224036.683	0.938	-5.017	3.772
2	1.5	1	1	1.5	2	225007.936	0.049	-4.293	3.779
2	1.5	1	1	0.5	1	225215.260	0.082	-3.123	3.772
2	2.5	2	1	1.5	2	225387.534	0.063	-3.135	3.779
2	1.5	1	1	0.5	0	225444.432	0.043	-2.990	3.764
2	1.5	2	1	1.5	1	225504.858	0.029	-2.519	3.723
2	2.5	2	1	0.5	1	225594.859	0.033	-2.637	3.772
2	2.5	3	1	1.5	2	225678.186	0.017	-2.366	3.779
2	1.5	1	1	1.5	1	226683.435	0.962	-4.905	3.723
2	2.5	2	1	1.5	1	227063.033	0.934	-4.500	3.723
3	2.5	3	2	2.5	3	336402.577	0.919	-4.070	11.307
3	2.5	3	2	2.5	2	336693.228	0.880	-4.508	11.297
3	2.5	2	2	2.5	3	337518.691	0.058	-4.505	11.307
3	2.5	2	2	2.5	2	337809.343	0.083	-2.979	11.297
3	3.5	3	2	2.5	3	338086.759	0.091	-2.994	11.307
3	2.5	2	2	1.5	1	338188.941	0.023	-2.226	11.284
3	2.5	3	2	1.5	2	338251.404	0.037	-2.009	11.245
3	3.5	3	2	2.5	2	338377.411	0.041	-2.054	11.297
3	3.5	4	2	2.5	3	338443.689	0.022	-1.895	11.307
3	2.5	2	2	1.5	2	339367.518	0.934	-4.312	11.245
3	3.5	3	2	1.5	2	339935.586	0.874	-4.158	11.245
4	3.5	4	3	3.5	4	448948.080	0.888	-3.809	22.596
4	3.5	4	3	3.5	3	449305.009	0.815	-4.259	22.584

Table 7.4: Transition frequency predictions for $^{13}C^{16}O^+$ - continued.

N'	J'	F'	N''	J''	F''	Frequency [MHz]	$\Delta\nu$ [MHz]	$log(I)$ [nm^2MHz]	E_{lower} [cm^{-1}]
4	3.5	3	3	3.5	4	450013.180	0.072	−4.662	22.596
4	3.5	3	3	3.5	3	450370.109	0.101	−2.897	22.584
4	4.5	4	3	3.5	4	450786.888	0.123	−2.914	22.596
4	3.5	3	3	2.5	2	450938.177	0.026	−1.803	22.565
4	3.5	4	3	2.5	3	450989.192	0.040	−1.661	22.528
4	4.5	4	3	3.5	3	451143.818	0.045	−1.683	22.584
4	4.5	5	3	3.5	4	451196.220	0.026	−1.569	22.596
4	3.5	3	3	2.5	3	452054.292	0.900	−3.966	22.528
4	4.5	4	3	2.5	3	452828.000	0.809	−3.978	22.528
5	4.5	5	4	4.5	5	561465.534	0.858	−3.634	37.646
5	4.5	5	4	4.5	4	561874.865	0.750	−4.136	37.633
5	4.5	4	4	4.5	5	562489.687	0.087	−4.797	37.646
5	4.5	4	4	4.5	4	562899.019	0.128	−2.853	37.633
5	5.5	5	4	4.5	5	563481.012	0.153	−2.869	37.646
5	4.5	4	4	3.5	3	563672.727	0.029	−1.510	37.607
5	4.5	5	4	3.5	4	563713.674	0.041	−1.405	37.571
5	5.5	5	4	4.5	4	563890.343	0.045	−1.418	37.633
5	5.5	6	4	4.5	5	563931.957	0.028	−1.328	37.646
5	4.5	4	4	3.5	4	564737.827	0.866	−3.742	37.571
5	5.5	5	4	3.5	4	565729.152	0.744	−3.892	37.571
6	5.5	6	5	5.5	6	673953.645	0.831	−3.515	56.457
6	5.5	6	5	5.5	5	674404.591	0.689	−4.088	56.442
6	5.5	5	5	5.5	6	674944.799	0.102	−4.921	56.457
6	5.5	5	5	5.5	5	675395.744	0.159	−2.834	56.442
6	6.5	6	5	5.5	6	676162.552	0.181	−2.849	56.457
6	5.5	5	5	4.5	4	676387.068	0.031	−1.294	56.409
6	5.5	6	5	4.5	5	676420.068	0.042	−1.209	56.375
6	6.5	6	5	5.5	5	676613.497	0.044	−1.218	56.442
6	6.5	7	5	5.5	6	676646.871	0.031	−1.144	56.457
6	5.5	5	5	4.5	5	677411.221	0.833	−3.593	56.375
6	6.5	6	5	4.5	5	678628.975	0.686	−3.865	56.375
7	6.5	7	6	6.5	7	786410.392	0.808	−3.437	79.027
7	6.5	7	6	6.5	6	786894.711	0.636	−4.086	79.011
7	6.5	6	6	6.5	7	787374.680	0.119	−5.039	79.027
7	6.5	6	6	6.5	6	787858.999	0.190	−2.834	79.011
7	7.5	7	6	6.5	7	788825.465	0.206	−2.848	79.027
7	6.5	6	6	5.5	5	789076.752	0.038	−1.129	78.971
7	6.5	7	6	5.5	6	789103.618	0.046	−1.059	78.938
7	7.5	7	6	6.5	6	789309.783	0.045	−1.064	79.011
7	7.5	8	6	6.5	7	789336.880	0.037	−1.002	79.027
7	6.5	6	6	5.5	6	790067.905	0.805	−3.495	78.938
7	7.5	7	6	5.5	6	791518.690	0.637	−3.878	78.938
8	7.5	8	7	7.5	8	898833.203	0.787	−3.389	105.357
8	7.5	8	7	7.5	7	899344.618	0.589	−4.117	105.340
8	7.5	7	7	7.5	8	899775.358	0.138	−5.157	105.357

Table 7.4: Transition frequency predictions for $^{13}C^{16}O^+$ - continued.

N'	J'	F'	N''	J''	F''	Frequency [MHz]	$\Delta\nu$ [MHz]	$log(I)$ [nm^2MHz]	E_{lower} [cm^{-1}]
8	7.5	7	7	7.5	7	900286.772	0.223	-2.849	105.340
8	8.5	8	7	7.5	8	901464.186	0.228	-2.862	105.357
8	7.5	7	7	6.5	6	901737.557	0.051	-1.004	105.291
8	7.5	8	7	6.5	7	901759.691	0.057	-0.943	105.259
8	8.5	8	7	7.5	7	901975.600	0.054	-0.947	105.340
8	8.5	9	7	7.5	8	901997.886	0.051	-0.893	105.357
8	7.5	7	7	6.5	7	902701.845	0.782	-3.433	105.259
8	8.5	8	7	6.5	7	904390.673	0.596	-3.919	105.259

Table 7.5: Transition frequency predictions for $^{12}C^{18}O^+$ up to 1 THz in the vibrational ground state.

N'	J'	N''	J''	Frequency [MHz]	$\Delta\nu$ [MHz]	$log(I)$ [nm^2MHz]	E_{lower} [cm^{-1}]
1	0.5	0	0.5	112088.491	0.020	-3.585	0.000
1	1.5	0	0.5	112478.420	0.019	-3.281	0.000
2	1.5	1	1.5	224172.860	0.041	-3.393	3.752
2	1.5	1	0.5	224562.789	0.032	-2.693	3.739
2	2.5	1	1.5	224822.743	0.035	-2.436	3.752
3	2.5	2	2.5	336248.989	0.061	-3.252	11.251
3	2.5	2	1.5	336898.871	0.048	-2.104	11.230
3	3.5	2	2.5	337158.824	0.051	-1.949	11.251
4	3.5	3	3.5	448312.761	0.082	-3.160	22.498
4	3.5	3	2.5	449222.596	0.064	-1.727	22.467
4	4.5	3	3.5	449482.549	0.067	-1.614	22.498
5	4.5	4	4.5	560360.065	0.103	-3.101	37.491
5	4.5	4	3.5	561529.854	0.081	-1.455	37.452
5	5.5	4	4.5	561789.807	0.084	-1.366	37.491
6	5.5	5	5.5	672386.798	0.125	-3.066	56.230
6	5.5	5	4.5	673816.540	0.100	-1.251	56.182
6	6.5	5	5.5	674076.493	0.103	-1.177	56.230
7	6.5	6	6.5	784388.863	0.150	-3.050	78.715
7	6.5	6	5.5	786078.558	0.122	-1.094	78.658
7	7.5	6	6.5	786338.511	0.125	-1.031	78.715
8	7.5	7	7.5	896362.176	0.178	-3.051	104.944
8	7.5	7	6.5	898311.823	0.147	-0.974	104.879
8	8.5	7	7.5	898571.776	0.150	-0.919	104.944

Table 7.6: Transition frequency predictions for $^{13}C^{18}O^+$ up to 1 THz in the vibrational ground state.

N'	J'	F'	N''	J''	F''	Frequency [MHz]	$\Delta\nu$ [MHz]	$log(I)$ [$nm^2 MHz$]	E_{lower} [cm^{-1}]
1	1.5	1	0	0.5	1	105611.494	0.975	−5.302	0.013
1	0.5	0	0	0.5	1	106861.160	0.084	−3.928	0.013
1	0.5	1	0	0.5	1	107081.470	0.042	−3.455	0.013
1	1.5	1	0	0.5	0	107137.959	0.021	−3.455	−0.038
1	1.5	2	0	0.5	1	107278.131	0.021	−3.225	0.013
1	0.5	1	0	0.5	0	108607.934	0.980	−5.277	−0.038
2	1.5	2	1	1.5	2	212607.270	0.952	−4.564	3.591
2	1.5	2	1	0.5	1	212803.932	0.943	−5.097	3.585
2	1.5	1	1	1.5	2	213798.708	0.054	−4.337	3.591
2	1.5	1	1	0.5	1	213995.370	0.088	−3.166	3.585
2	2.5	2	1	1.5	2	214158.627	0.064	−3.177	3.591
2	1.5	1	1	0.5	0	214215.680	0.049	−3.034	3.577
2	1.5	2	1	1.5	1	214273.908	0.040	−2.562	3.536
2	2.5	2	1	0.5	1	214355.289	0.042	−2.681	3.585
2	2.5	3	1	1.5	2	214436.418	0.035	−2.410	3.591
2	1.5	1	1	1.5	1	215465.346	0.965	−4.994	3.536
2	2.5	2	1	1.5	1	215825.264	0.942	−4.582	3.536
3	2.5	3	2	2.5	3	319576.063	0.924	−4.151	10.744
3	2.5	3	2	2.5	2	319853.854	0.889	−4.576	10.735
3	2.5	2	2	2.5	3	320705.860	0.066	−4.547	10.744
3	2.5	2	2	2.5	2	320983.651	0.093	−3.020	10.735
3	3.5	3	2	2.5	3	321242.054	0.093	−3.034	10.744
3	2.5	2	2	1.5	1	321343.569	0.048	−2.269	10.723
3	2.5	3	2	1.5	2	321405.210	0.056	−2.051	10.683
3	3.5	3	2	2.5	2	321519.845	0.059	−2.097	10.735
3	3.5	4	2	2.5	3	321585.301	0.051	−1.937	10.744
3	2.5	2	2	1.5	2	322535.007	0.941	−4.397	10.683
3	3.5	3	2	1.5	2	323071.201	0.888	−4.229	10.683
4	3.5	4	3	3.5	4	426519.193	0.894	−3.885	21.471
4	3.5	4	3	3.5	3	426862.440	0.828	−4.314	21.460
4	3.5	3	3	3.5	4	427597.957	0.083	−4.704	21.471
4	3.5	3	3	3.5	3	427941.204	0.112	−2.936	21.460
4	4.5	4	3	3.5	4	428326.756	0.125	−2.951	21.471
4	3.5	3	3	2.5	2	428477.398	0.064	−1.844	21.442
4	3.5	4	3	2.5	3	428528.431	0.071	−1.702	21.404
4	4.5	4	3	3.5	3	428670.003	0.074	−1.725	21.460
4	4.5	5	3	3.5	4	428722.424	0.067	−1.611	21.471
4	3.5	3	3	2.5	3	429607.195	0.911	−4.045	21.404
4	4.5	4	3	2.5	3	430335.995	0.828	−4.037	21.404
5	4.5	5	4	4.5	5	533436.342	0.865	−3.703	35.772
5	4.5	5	4	4.5	4	533832.010	0.766	−4.179	35.758
5	4.5	4	4	4.5	5	534473.688	0.102	−4.837	35.772
5	4.5	4	4	4.5	4	534869.356	0.141	−2.888	35.758
5	5.5	5	4	4.5	5	535406.616	0.158	−2.904	35.772

Table 7.6: Transition frequency predictions for $^{13}C^{18}O^+$ - continued.

N'	J'	F'	N''	J''	F''	Frequency [MHz]	$\Delta\nu$ [MHz]	$log(I)$ [nm^2MHz]	E_{lower} [cm^{-1}]
5	4.5	4	4	3.5	3	535598.155	0.080	−1.550	35.734
5	4.5	5	4	3.5	4	535639.573	0.086	−1.444	35.698
5	5.5	5	4	4.5	4	535802.284	0.088	−1.457	35.758
5	5.5	6	4	4.5	5	535844.369	0.083	−1.368	35.772
5	4.5	4	4	3.5	4	536676.919	0.881	−3.815	35.698
5	5.5	5	4	3.5	4	537609.847	0.770	−3.940	35.698
6	5.5	6	5	5.5	6	640326.372	0.840	−3.579	53.645
6	5.5	6	5	5.5	5	640764.125	0.709	−4.119	53.631
6	5.5	5	5	5.5	6	641330.039	0.123	−4.958	53.645
6	5.5	5	5	5.5	5	641767.791	0.174	−2.866	53.631
6	6.5	6	5	5.5	6	642475.702	0.190	−2.881	53.645
6	5.5	5	5	4.5	4	642700.720	0.097	−1.331	53.600
6	5.5	6	5	4.5	5	642734.399	0.102	−1.247	53.565
6	6.5	6	5	5.5	5	642913.455	0.103	−1.255	53.631
6	6.5	7	5	5.5	6	642947.507	0.100	−1.182	53.645
6	5.5	5	5	4.5	5	643738.066	0.852	−3.660	53.565
6	6.5	6	5	4.5	5	644883.729	0.717	−3.902	53.565
7	6.5	7	6	6.5	7	747187.526	0.817	−3.495	75.092
7	6.5	7	6	6.5	6	747659.331	0.657	−4.107	75.076
7	6.5	6	6	6.5	7	748163.578	0.144	−5.074	75.092
7	6.5	6	6	6.5	6	748635.383	0.208	−2.863	75.076
7	7.5	7	6	6.5	7	749528.507	0.219	−2.877	75.092
7	6.5	6	6	5.5	5	749781.046	0.116	−1.164	75.038
7	6.5	7	6	5.5	6	749808.661	0.120	−1.094	75.004
7	7.5	7	6	6.5	6	750000.312	0.121	−1.099	75.076
7	7.5	8	6	6.5	7	750028.157	0.119	−1.037	75.092
7	6.5	6	6	5.5	6	750784.713	0.828	−3.556	75.004
7	7.5	7	6	5.5	6	752149.642	0.672	−3.906	75.004
8	7.5	8	7	7.5	8	854017.557	0.797	−3.442	100.110
8	7.5	8	7	7.5	7	854517.207	0.613	−4.129	100.093
8	7.5	7	7	7.5	8	854970.730	0.169	−5.188	100.110
8	7.5	7	7	7.5	7	855470.380	0.244	−2.875	100.093
8	8.5	8	7	7.5	8	856559.940	0.248	−2.888	100.110
8	7.5	7	7	6.5	6	856835.309	0.138	−1.036	100.048
8	7.5	8	7	6.5	7	856858.189	0.141	−0.975	100.015
8	8.5	8	7	7.5	7	857059.590	0.141	−0.979	100.093
8	8.5	9	7	7.5	8	857082.623	0.141	−0.925	100.110
8	7.5	7	7	6.5	7	857811.362	0.808	−3.488	100.015
8	8.5	8	7	6.5	7	859400.572	0.637	−3.937	100.015
9	8.5	9	8	8.5	9	960813.859	0.782	−3.413	128.699
9	8.5	9	8	8.5	8	961336.541	0.577	−4.175	128.682
9	8.5	8	8	8.5	9	961747.866	0.197	−5.303	128.699
9	8.5	8	8	8.5	8	962270.548	0.281	−2.901	128.682
9	9.5	9	8	8.5	9	963565.252	0.276	−2.912	128.699
9	8.5	8	8	7.5	7	963859.759	0.164	−0.938	128.629

Table 7.6: Transition frequency predictions for $^{13}C^{18}O^+$ - continued.

N'	J'	F'	N''	J''	F''	Frequency [MHz]	$\Delta\nu$ [MHz]	$log(I)$ [nm^2MHz]	E_{lower} [cm^{-1}]
9	8.5	9	8	7.5	8	963878.924	0.167	-0.885	128.597
9	9.5	9	8	8.5	8	964087.935	0.167	-0.888	128.682
9	8.5	8	8	7.5	8	964812.931	0.794	-3.450	128.597
9	9.5	9	8	7.5	8	966630.318	0.612	-3.990	128.597

8

Conclusion

As often in the past, astronomical observations have triggered a more elaborate and refined molecular analysis. The molecules investigated in the course of this thesis are examples of the synergy between molecular spectroscopy and radio astronomy. On the basis of the data presented in this work, their rotational and ro-vibrational spectra can be predicted in the terahertz domain. The reliable data are available for astronomers around the world via the Cologne Database for Molecular Spectroscopy (CDMS) [13].

The detection of radicals and ions in the terahertz domain has been facilitated by the new Cologne Supersonic Jet Spectrometer for Terahertz Applications (SuJeSTA), which has been designed and assembled for the performed investigations in this work. SuJeSTA is a tool for major research projects in the Cologne spectroscopy group embedded in the international network of the Laboratoire Europeén Associé (LEA *HiRes*). The spectrometer is of comparable sensitivity as common "cell-experiments" with the advantage of detecting cold radicals and ions. The spectroscopical results, obtained with this instrument, will be key to future interstellar observations, since prevalent species are a main target of astronomers' activities.

Besides the astrophysical relevance of the presented results, this work has also yielded useful information for spectroscopists. The Renner-Teller coupling and the Coriolis interaction of C_3H have been investigated for the first time with SuJeSTA. Further measurements on other carbon chain molecules with similar effects are now possible and of high priority.

In continuation to the work started, the measurements on CO^+ will proceed to optimize the process of ion production and to improve the mass invariant parameter set. Other important ions, for instance HCO^+, can now be analyzed by means of laboratory terahertz spectroscopy.

The evaporation cell of the Cologne terahertz spectrometer facilitates the gas phase analysis of solid species. The investigations of KCl and $NaCl$ are the beginning of a series of measurements of interstellar abundant metal halides, such as KF, NaF, AlF, and $AlCl$.

A

Experimental Data: Potassium Chloride

The experimental data on all isotopomers of potassium chloride investigated in this thesis are summarized in the following tables. All transitions have been recorded with the Cologne Terahertz Spectrometer in the frequency region between 170 and 930 *GHz*, if not indicated otherwise. Lines taken from the work of Clouser and Gordy [3], which were included in the fit, are marked with a. IR measurements are not included in these tables.

All transition frequencies and the values for observed minus calculated are given in *MHz*. For each measured transition the estimated experimental error, written in brackets, is in units of the least significant digits.

A.1 $^{39}K^{35}Cl$

Table A.1: Rotational spectrum of the main isotopomer of potassium chloride, $^{39}K^{35}Cl$, in the vibrational states $v \leq 7$.

v	J'	J''	Frequency [MHz]	o.-c. [MHz]
0	13	12	99929.540(100)a	0.063
0	20	19	153677.480(100)a	0.048
0	23	22	176690.335(20)	−0.031
0	25	24	192023.490(100)a	0.036
0	26	25	199687.101(10)	−0.003
0	29	28	222665.524(20)	−0.006
0	30	29	230320.560(100)a	−0.011
0	31	30	237973.267(20)	0.003
0	35	34	268558.980(150)a	−0.006
0	40	39	306728.915(20)	0.023
0	41	40	314353.776(20)	−0.013
0	46	45	352428.521(10)	−0.009
0	57	56	435861.881(20)	−0.007
0	59	58	450976.530(10)	−0.006
0	60	59	458526.955(50)	0.000
0	65	64	496206.835(30)	−0.006
0	87	86	660348.816(20)	−0.011
0	91	90	689861.260(10)	−0.008
0	92	91	697221.636(10)	−0.005
0	93	92	704574.744(10)	−0.014
0	94	93	711920.535(10)	−0.005
0	97	96	733913.075(20)	0.009
0	98	97	741228.710(10)	0.008
0	116	115	871508.702(20)	0.009
0	117	116	878663.515(20)	0.035
0	121	120	907189.061(20)	0.035
0	124	123	928482.637(20)	0.022
1	13	12	99316.440(100)a	−0.006
1	23	22	175605.726(20)	−0.043
1	25	24	190844.490(100)a	−0.054
1	29	28	221297.978(20)	−0.014
1	30	29	228905.950(100)a	0.075
1	40	39	304842.629(10)	0.008
1	41	40	312420.326(10)	−0.034
1	46	45	350259.321(10)	0.008
1	59	58	448194.266(10)	−0.005
1	60	59	455697.527(20)	−0.006
1	65	64	493141.637(10)	0.002
1	88	87	663587.704(20)	−0.004

Rotational transitions of $^{39}K^{35}Cl$ - continued.

v	J'	J''	Frequency [MHz]	o.-c. [MHz]
1	92	91	692883.351(10)	0.004
1	93	92	700189.335(20)	0.013
1	94	93	707487.962(20)	0.001
1	98	97	736607.573(20)	0.011
2	23	22	174525.616(20)	−0.023
2	25	24	189670.520(100)a	0.030
2	29	28	219936.081(10)	−0.011
2	44	43	333067.691(20)	−0.005
2	45	44	340585.168(20)	0.009
2	46	45	348099.143(30)	0.047
2	58	57	437962.695(20)	0.008
2	60	59	452879.939(20)	0.005
2	89	88	666743.254(20)	0.001
2	92	91	688563.594(10)	−0.002
2	93	92	695822.645(10)	0.000
2	118	117	874706.086(10)	0.007
2	122	121	902817.797(20)	0.009
2	125	124	923800.200(20)	0.008
3	23	22	173450.015(30)	0.004
3	29	28	218579.864(10)	−0.015
3	41	40	308577.564(10)	−0.023
3	44	43	331010.083(30)	0.015
3	57	56	427831.754(20)	−0.010
3	58	57	435250.483(20)	−0.019
3	60	59	450074.244(20)	−0.006
3	66	65	494429.990(20)	−0.004
3	89	88	662582.322(20)	0.002
3	90	89	669816.172(30)	−0.003
3	94	93	698679.866(20)	−0.016
3	99	98	734592.154(20)	0.006
3	123	122	904073.859(30)	0.022
3	126	125	924886.826(20)	−0.014
4	24	23	179858.951(10)	−0.005
4	29	28	217229.378(40)	−0.020
4	32	31	239625.029(40)	−0.034
4	41	40	306668.331(30)	−0.037
4	42	41	314102.609(10)	−0.012
4	43	42	321533.548(20)	−0.036
4	58	57	432549.907(30)	−0.007
4	59	58	439917.551(30)	−0.008
4	60	59	447280.577(20)	−0.001

Rotational transitions of $^{39}K^{35}Cl$ - continued.

v	J'	J''	Frequency [MHz]	o.-c. [MHz]
4	66	65	491357.106(30)	0.010
4	90	89	665626.919(30)	0.001
4	94	93	694304.665(20)	−0.010
4	95	94	701455.765(20)	−0.027
4	100	99	737097.444(20)	0.020
4	120	119	877590.229(30)	0.009
4	127	126	925897.165(40)	0.021
5	24	23	178746.054(50)	−0.021
5	41	40	304767.367(20)	0.018
5	42	41	312155.248(20)	0.001
5	45	44	334298.854(30)	−0.044
5	59	58	437182.327(40)	0.003
5	60	59	444499.017(30)	0.008
5	67	66	495579.669(40)	0.018
5	90	89	661456.192(20)	0.002
5	94	93	689948.881(40)	−0.004
5	95	94	697053.841(20)	0.098
5	96	95	704151.084(40)	−0.030
5	100	99	732464.136(10)	0.006
5	120	119	872032.888(20)	0.030
6	24	23	177637.991(50)	−0.015
6	42	41	310216.388(70)	0.048
6	45	44	332221.583(20)	0.034
6	46	45	339549.682(40)	0.002
6	60	59	441729.643(50)	0.006
6	67	66	492487.524(80)	0.060
6	91	90	664392.093(40)	0.004
6	95	94	692671.411(40)	−0.072
6	96	95	699722.876(40)	0.052
6	101	100	734864.469(50)	−0.012
7	59	58	431747.969(100)	0.062
7	95	94	688309.128(30)	−0.032
7	96	95	695314.670(20)	−0.027
7	101	100	730227.407(40)	0.007
7	102	101	737186.342(40)	−0.041
7	122	121	874570.357(40)	−0.006

A.2 $^{39}K^{37}Cl$

Table A.2: Rotational spectrum of potassium chloride, $^{39}K^{37}Cl$, in the vibrational states $v \leq 7$.

v	J'	J''	Frequency [MHz]	o.-c. [MHz]
0	22	21	164220.000(100)a	−0.039
0	23	22	171671.828(30)	−0.022
0	24	23	179121.980(100)a	0.017
0	27	26	201461.384(10)	0.013
0	36	35	268363.840(150)a	−0.071
0	41	40	305442.324(20)	−0.004
0	42	41	312849.217(10)	0.002
0	43	42	320252.992(20)	−0.004
0	47	46	349835.604(10)	0.017
0	59	58	438230.604(10)	0.009
0	60	59	445570.230(10)	0.009
0	90	89	663356.435(10)	−0.001
0	94	93	691983.702(10)	−0.001
0	95	94	699123.218(10)	0.002
0	96	95	706255.644(20)	−0.009
0	97	96	713380.951(30)	0.009
0	100	99	734713.156(10)	0.006
0	101	100	741809.092(20)	0.011
0	120	119	875114.143(10)	−0.003
0	124	123	902782.733(20)	−0.006
0	125	124	909676.847(30)	0.002
0	127	126	923436.882(30)	0.016
1	19	18	140997.100(100)a	−0.024
1	24	23	178038.180(100)a	0.046
1	27	26	200242.068(20)	0.007
1	41	40	303590.774(20)	0.003
1	42	41	310952.497(10)	−0.001
1	45	44	333018.759(20)	0.012
1	46	45	340367.639(10)	0.032
1	47	46	347713.112(30)	0.047
1	48	47	355055.065(40)	0.018
1	59	58	435566.160(20)	0.016
1	60	59	442860.629(20)	0.019
1	67	66	493793.289(10)	0.022
1	91	90	666414.030(20)	0.005
1	95	94	694833.172(10)	0.008
1	96	95	701920.451(20)	−0.005
1	100	99	730197.395(20)	0.017
1	101	100	737248.188(30)	0.021

Rotational transitions of $^{39}K^{37}Cl$ - continued.

v	J'	J''	Frequency [MHz]	o.-c. [MHz]
1	121	120	876581.475(10)	−0.014
1	125	124	904032.927(40)	−0.008
1	128	127	924523.385(20)	−0.027
2	27	26	199027.709(20)	0.005
2	42	41	309063.520(30)	−0.002
2	45	44	330994.895(20)	0.044
2	59	58	432912.654(20)	0.000
2	60	59	440162.154(20)	0.002
2	91	90	662321.839(20)	−0.002
2	92	91	669392.023(20)	−0.001
2	95	94	690561.191(20)	−0.017
2	96	95	697603.551(10)	−0.008
2	101	100	732706.597(20)	0.005
2	122	121	877973.386(40)	−0.002
2	129	128	925535.493(40)	−0.070
3	27	26	197818.327(40)	−0.013
3	42	41	307182.344(30)	−0.004
3	43	42	314451.203(20)	−0.007
3	59	58	430270.210(20)	0.000
3	60	59	437474.933(30)	0.001
3	68	67	494946.506(30)	−0.001
3	92	91	665272.473(40)	−0.035
3	96	95	693305.084(10)	−0.017
3	97	96	700295.563(30)	−0.012
3	98	97	707278.780(50)	−0.048
3	102	101	735138.139(40)	0.031
3	122	121	872512.619(20)	−0.042
4	27	26	196614.010(50)	0.004
4	42	41	305309.053(30)	0.017
4	43	42	312533.311(20)	0.006
4	46	45	334186.722(30)	−0.022
4	48	47	348605.506(120)	0.014
4	59	58	427638.909(50)	0.012
4	96	95	689025.199(20)	−0.023
4	97	96	695971.152(20)	−0.022
4	102	101	730591.125(20)	−0.011
4	103	102	737492.702(40)	0.064
5	42	41	303443.681(30)	0.032
5	46	45	332143.775(20)	0.023
5	47	46	339310.479(40)	0.014

Rotational transitions of $^{39}K^{37}Cl$ - continued.

v	J'	J''	Frequency $[MHz]$	o.-c. $[MHz]$
5	60	59	432134.565(30)	0.008
5	68	67	488894.534(50)	0.032
5	93	92	664016.561(40)	−0.033
5	97	96	691665.640(50)	−0.062
5	98	97	698560.108(50)	−0.020
5	103	102	732921.322(40)	−0.042
5	124	123	875033.403(50)	0.042
7	44	43	313917.113(150)	0.114

A.3 $^{41}K^{35}Cl$

Table A.3:   Rotational spectrum of potassium chloride, $^{41}K^{35}Cl$, in the vibrational states $v \leq 6$.

v	J'	J''	Frequency $[MHz]$	o.-c. $[MHz]$
0	41	40	307132.108(40)	−0.041
0	42	41	314579.757(20)	−0.014
0	47	46	351769.280(30)	−0.009
0	57	56	425875.283(20)	−0.009
0	58	57	433263.649(20)	−0.015
0	59	58	440647.671(20)	−0.023
0	60	59	448027.290(10)	−0.015
0	66	65	492207.960(20)	−0.013
0	77	76	572731.595(20)	0.017
0	80	79	594575.441(20)	0.005
0	90	89	666986.231(20)	−0.016
0	93	92	688580.933(10)	−0.014
0	94	93	695765.266(20)	−0.017
0	95	94	702942.549(30)	0.006
0	96	95	710112.600(30)	−0.050
0	99	98	731579.283(20)	−0.003
0	100	99	738720.019(20)	0.005
0	101	100	745853.210(20)	0.004
0	119	118	872873.885(10)	0.001
0	124	123	907658.805(40)	−0.002
1	41	40	305265.147(20)	−0.009
1	42	41	312667.242(30)	0.001
1	43	42	320066.170(20)	−0.018
1	47	46	349629.093(70)	0.020
1	57	56	423279.704(30)	0.001
1	58	57	430622.540(20)	0.002
1	66	65	489202.556(30)	0.002
1	90	89	662888.069(20)	0.011
1	94	93	691485.029(30)	0.034
1	95	94	698616.732(30)	0.000
1	96	95	705741.345(40)	0.028
1	100	99	734166.609(10)	0.007
1	101	100	741254.294(20)	0.018
1	124	123	902013.323(40)	−0.024
2	42	41	310762.545(20)	0.006
2	45	44	332813.615(20)	−0.001
2	46	45	340157.353(200)	0.009
2	58	57	427992.315(30)	0.014

Rotational transitions of $^{41}K^{35}Cl$ - continued.

v	J'	J''	Frequency $[MHz]$	o.-c. $[MHz]$
2	59	58	435285.453(20)	0.002
2	60	59	442574.189(30)	0.006
2	67	66	493465.282(30)	0.000
2	91	90	665921.387(40)	−0.008
2	95	94	694309.229(40)	0.008
2	96	95	701388.497(50)	0.005
2	101	100	736674.948(30)	0.045
2	128	127	923688.742(40)	−0.027
3	58	57	425373.037(70)	−0.004
3	59	58	432621.038(50)	−0.004
3	67	66	490439.700(30)	−0.015
3	91	90	661812.751(40)	−0.005
3	92	91	668875.124(40)	0.064
3	95	94	690020.181(30)	0.032
3	101	100	732115.246(20)	0.007
4	43	42	314240.342(40)	−0.002
4	59	58	429967.895(50)	0.005
4	60	59	437166.579(50)	0.055
4	96	95	692738.938(20)	0.004
4	122	121	871699.993(40)	0.059
5	43	42	312314.759(50)	0.031
5	46	45	333951.281(150)	0.010
5	60	59	434480.004(150)	0.040
5	96	95	688442.479(30)	−0.004
6	46	45	331900.295(30)	0.089

A.4 $^{41}K^{37}Cl$

Table A.4: Rotational spectrum of potassium chloride, $^{41}K^{37}Cl$, in the vibrational states $v \leq 5$.

v	J'	J''	Frequency $[MHz]$	o.-c. $[MHz]$
0	43	42	312681.506(20)	0.001
0	44	43	319908.199(50)	−0.040
0	48	47	348783.558(50)	0.095
0	59	58	427897.528(20)	0.006
0	60	59	435066.167(30)	0.021
0	68	67	492256.708(20)	0.002
0	92	91	661837.198(10)	−0.006
0	93	92	668828.386(40)	−0.011
0	96	95	689762.098(20)	−0.014
0	97	96	696726.456(40)	−0.032
0	98	97	703683.989(30)	0.009
0	102	101	731443.650(20)	−0.002
0	103	102	738365.626(20)	−0.009
0	104	103	745280.236(40)	−0.062
0	123	122	875171.395(30)	0.010
0	127	126	902129.791(50)	−0.037
1	42	41	303622.111(30)	0.013
1	43	42	310808.300(20)	0.002
1	46	45	332348.455(10)	0.017
1	47	46	339522.069(50)	−0.025
1	59	58	425327.227(30)	−0.068
1	60	59	432452.374(30)	0.019
1	68	67	489294.441(30)	0.030
1	93	92	664777.156(30)	0.016
1	97	96	692500.999(40)	−0.029
1	98	97	699415.033(40)	0.063
1	99	98	706322.074(50)	0.117
1	103	102	733878.897(20)	0.005
1	131	130	923237.543(70)	−0.070
2	60	59	429849.212(40)	0.026
2	69	68	493385.212(30)	−0.008
2	97	96	688293.192(30)	0.007
2	98	97	695163.787(10)	0.011
2	99	98	702027.281(100)	−0.130
2	104	103	736238.621(50)	−0.110
2	125	124	877802.884(70)	−0.084
3	44	43	314181.183(40)	−0.003

Rotational transitions of $^{41}K^{37}Cl$ - continued.

v	J'	J''	Frequency [MHz]	o.-c. [MHz]
3	104	103	731746.563(30)	−0.033
4	44	43	312287.815(70)	0.022
4	99	98	693492.887(20)	−0.008
5	47	46	331415.512(150)	−0.074

A.5 $^{40}K^{35}Cl$

Table A.5: Rotational spectrum of potassium chloride, $^{40}K^{35}Cl$, in the vibrational ground state.

v	J'	J''	Frequency $[MHz]$	o.-c. $[MHz]$
0	44	43	333235.809(70)	-0.037
0	76	75	571866.904(70)	0.142

B

Experimental Data: Propynylidyne

The experimental data on propynylidyne, C_3H, investigated in this thesis are summarized in the following tables. All transitions have been recorded with the Supersonic Jet Spectrometer for Terahertz Applications (SuJeSTA) in the frequency region between 370 and 580 GHz, if not indicated otherwise. Lines taken from the work of Gottlieb et al. [8], of Yamamoto et al. [9], and of Kaifu et al. [6] are marked with a, b, and c, respectively. Lines indicated with * have been omitted from the final fit because their observed minus calculated value exceeded 3σ.

All transition frequencies and the values for observed minus calculated are given in MHz. For each measured transition the estimated experimental error, written in brackets, is in units of the least significant digits.

B.1 C_3H in the $^2\Pi$-ground state

Table B.1: Observed transition frequencies for propynyli-
dyne, C_3H, in the $^2\Pi$-ground state.

N'	K'	J'	F'	N''	K''	J''	F''	Frequency $[MHz]$	o.-c. $[MHz]$
2	-1	1.5	1	1	1	0.5	1	32617.016(2)c	0.000
2	-1	1.5	2	1	1	0.5	1	32627.297(2)c	−0.001
2	-1	1.5	1	1	1	0.5	0	32634.389(2)c	0.000
2	1	1.5	2	1	-1	0.5	1	32660.645(2)c	0.000
2	1	1.5	1	1	-1	0.5	0	32663.361(2)c	−0.001
2	1	1.5	1	1	-1	0.5	1	32667.668(2)c	0.000
3	-1	3.5	4	2	1	2.5	3	80388.107(50)a	0.017
3	-1	3.5	3	2	1	2.5	2	80389.442(50)a	0.035
3	1	3.5	4	2	-1	2.5	3	80420.646(50)a	−0.065
3	1	3.5	3	2	-1	2.5	2	80422.052(50)a	−0.049
4	-1	4.5	5	4	1	3.5	4	97995.166(50)a	−0.025
4	-1	4.5	4	4	1	3.5	3	97995.913(50)a	−0.029
4	1	4.5	5	4	-1	3.5	4	98011.611(50)a	−0.036
4	1	4.5	4	4	-1	3.5	3	98012.524(50)a	−0.061
5	1	4.5	5	3	-1	3.5	4	103319.276(50)a	−0.042
5	1	4.5	4	3	-1	3.5	3	103319.786(50)a	−0.054
5	-1	4.5	5	3	1	3.5	4	103372.483(50)a	−0.063
5	-1	4.5	4	3	1	3.5	3	103373.094(50)a	−0.066
5	1	5.5	6	4	-1	4.5	5	119804.682(50)a	0.018
5	1	5.5	5	4	-1	4.5	4	119805.322(50)a	0.012
5	-1	5.5	6	4	1	4.5	5	119847.476(50)a	0.017
5	-1	5.5	5	4	1	4.5	4	119848.259(50)a	−0.006
6	-1	6.5	7	5	1	5.5	6	141635.793(50)a	−0.011
6	-1	6.5	6	5	1	5.5	5	141636.431(50)a	0.057
6	1	6.5	7	5	-1	5.5	6	141708.728(50)a	−0.001
6	1	6.5	6	5	-1	5.5	5	141709.494(50)a	0.041
7	1	6.5		6	-1	5.5		149106.972(50)a	−0.015
7	-1	6.5		6	1	5.5		149212.667(50)a	−0.022
7	1	7.5	8	6	-1	6.5	7	163491.035(50)a	0.022
7	1	7.5	7	6	-1	6.5	6	163491.557(50)a	0.036
7	-1	7.5	8	6	1	6.5	7	163597.232(50)a	0.007
7	-1	7.5	7	6	1	6.5	6	163597.900(50)a	0.011
8	-1	7.5		7	1	6.5		171958.650(50)a	−0.007
8	1	7.5		7	-1	6.5		172094.778(50)a	−0.021
8	-1	8.5	9	7	1	7.5	8	185371.952(50)a	0.047
8	-1	8.5	8	7	1	7.5	7	185372.417(50)a	0.056
8	1	8.5	9	7	-1	7.5	8	185513.968(50)a	0.020
8	1	8.5	8	7	-1	7.5	7	185514.589(50)a	0.025
9	1	8.5		8	-1	7.5		194780.373(50)a	0.009
9	-1	8.5		8	1	7.5		194948.795(50)a	−0.019

Observed transition frequencies for C_3H in the $^2\Pi$-ground state - continued.

N'	K'	J'	F'	N''	K''	J''	F''	Frequency $[MHz]$	o.-c. $[MHz]$
11	1	11.5		10	-1	10.5		251174.624(50)b	0.071
11	-1	11.5	12	10	1	10.5	11	251433.892(50)b	0.025
11	-1	11.5	11	10	1	10.5	10	251434.415(50)b	0.049
12	-1	11.5		11	1	10.5		263062.936(50)b	0.070
12	1	11.5		11	-1	10.5		263332.405(50)b	0.013
12	-1	12.5		11	1	11.5		273161.117(50)b	0.067
12	1	12.5		11	-1	11.5		273461.665(50)b	0.056
13	1	12.5		12	-1	11.5		285764.383(50)b	0.006
13	-1	12.5		12	1	11.5		286066.633(50)b	0.040
13	1	13.5		12	-1	12.5		295172.315(50)b	0.101
13	-1	13.5		12	1	12.5		295514.212(50)b	0.052
14	-1	13.5		13	1	12.5		308437.925(50)b	0.044
14	1	13.5		13	-1	12.5		308771.023(50)b	0.078
15	1	14.5		14	-1	13.5		331084.761(50)b	0.065
15	-1	14.5		14	1	13.5		331445.807(50)b	0.089
15	-1	15.5		14	1	14.5		339688.210(50)$b*$	0.157
15	1	15.5		14	-1	14.5		339263.251(50)$b*$	0.170
16	-1	15.5		15	1	14.5		353706.329(50)b	0.086
16	1	15.5		15	-1	14.5		354091.056(50)b	0.139
17	1	16.5		16	-1	15.5		376303.928(30)	-0.062
17	-1	16.5		16	1	15.5		376705.892(20)	-0.027
17	1	17.5		16	-1	16.5		383435.036(20)	-0.006
17	-1	17.5		16	1	16.5		383942.379(20)	-0.009
18	-1	17.5		17	1	16.5		398879.391(20)	-0.022
18	1	17.5		17	-1	16.5		399288.848(20)	-0.020
18	-1	18.5		17	1	17.5		405547.395(20)	-0.028
18	1	18.5		17	-1	17.5		406095.489(20)	0.011
19	1	18.5		18	-1	17.5		421433.903(30)	-0.036
19	1	19.5		18	-1	18.5		427675.333(30)	0.031
19	-1	19.5		18	1	18.5		428263.655(20)	-0.025
20	-1	19.5		19	1	18.5		443968.986(30)	0.043
20	1	19.5		19	-1	18.5		444336.703(30)	0.054
20	-1	20.5		19	1	19.5		449817.164(30)	-0.008
20	1	20.5		19	-1	19.5		450445.449(100)	-0.010
21	1	20.5		20	-1	19.5		466485.740(30)	0.022
21	-1	20.5		20	1	19.5		466772.248(40)	-0.042
21	1	21.5		20	-1	20.5		471971.592(20)	-0.006
21	-1	21.5		20	1	20.5		472639.376(30)	0.010
22	-1	21.5		21	1	20.5		488985.510(80)	0.034
22	1	21.5		21	-1	20.5		489095.552(80)	0.066
22	-1	22.5		21	1	21.5		494137.204(30)	-0.021
22	1	22.5		21	-1	21.5		494844.056(30)	0.012
23	-1	22.5		22	1	21.5		511182.614(30)	0.009

Observed transition frequencies for C_3H in the $^2\Pi$-ground state - continued.

N'	K'	J'	F'	N''	K''	J''	F''	Frequency $[MHz]$	o.-c. $[MHz]$
23	1	22.5		22	-1	21.5		511469.331(50)	-0.003
23	1	23.5		22	-1	22.5		516312.799(20)	0.014
24	1	23.5	24	23	-1	22.5	23	532658.301(100)	0.130
24	1	23.5	23	23	-1	22.5	22	532658.854(100)	-0.239
24	1	24.5		23	-1	23.5		539280.745(20)	0.000
25	-1	24.5	25	24	1	23.5	24	552384.896(200)	0.175
25	-1	24.5	24	24	1	23.5	23	552387.014(200)	-0.302

B.2 C_3H in the excited ν_4 ($^2\Sigma^\mu$) bending state

Table B.2: Observed transition frequencies for propynyli-
dyne, C_3H, in the excited ν_4 ($^2\Sigma^\mu$) bending state.

N'	J'	F'	N''	J''	F''	Frequency [MHz]	o.-c. [MHz]
3	3.5	4	2	2.5	3	67293.837(50)b	−0.021
3	3.5	3	2	2.5	2	67294.256(50)b	−0.017
3	2.5	3	2	1.5	2	67323.949(50)b	−0.046
3	2.5	2	2	1.5	1	67325.109(50)b	0.009
4	4.5		3	3.5		89730.570(50)b	−0.022
4	3.5	4	3	2.5	3	89759.353(50)b	−0.003
4	3.5	3	3	2.5	2	89759.894(50)b	0.039
5	5.5		4	4.5		112166.938(50)b	−0.027
5	4.5	5	4	3.5	4	112194.054(50)b	−0.007
7	7.5		6	6.5		157038.932(50)b	−0.021
7	6.5		6	5.5		157061.150(50)b	−0.042
8	8.5		7	7.5		179474.490(50)b	−0.027
8	7.5		7	6.5		179493.278(50)b	−0.043
9	9.5		8	8.5		201909.790(50)b	−0.025
9	8.5		8	7.5		201924.343(50)b	−0.029
11	11.5		10	10.5		246780.010(50)b	0.018
11	10.5		10	9.5		246782.751(50)b	−0.003
12	11.5		11	10.5		269209.854(50)b	0.014
12	12.5		11	11.5		269215.264(50)b	−0.020
13	12.5		12	11.5		291635.396(50)b	0.035
13	13.5		12	12.5		291651.235(50)b	0.009
14	13.5		13	12.5		314059.268(50)b	0.072
14	14.5		13	13.5		314088.552(50)b	0.041
15	14.5		14	13.5		336481.314(50)b	0.092
15	15.5		14	14.5		336528.310(50)b	0.058
16	15.5		15	14.5		358901.425(50)b	0.097
16	16.5		15	15.5		358972.316(50)b	0.045
17	16.5	17	16	15.5	16	381318.554(100)	−0.134
17	16.5	16	16	15.5	15	381319.256(100)	−0.091
17	17.5	18	16	16.5	17	381423.638(50)	−0.084
17	17.5	17	16	16.5	16	381424.402(80)	0.037
18	17.5		17	16.5		403735.406(20)	−0.034
18	18.5		17	17.5		403887.716(80)	−0.091
19	18.5		18	17.5		426148.770(30)	0.004
19	19.5		18	18.5		426375.590(100)	−0.048
20	19.5		19	18.5		448560.028(80)	0.139
20	20.5		19	19.5		448907.703(30)	0.012
21	21.5		20	20.5		471532.167(30)	−0.021
23	23.5	23	22	22.5	22	517808.027(200)	0.167
23	23.5	24	22	22.5	23	517808.732(200)	−0.078

B.3 Transition frequencies of the $v_4 = 1$ ($^2\Sigma^\mu$) bending vibration of C_3H

Table B.3: Observed transition frequencies of the $v_4 = 1$ ($^2\Sigma^\mu$) bending vibration of C_3H.

N'	K'	v_4'	J'	F'	N''	K''	v_4''	J''	F''	Frequency [MHz]	o.-c. [MHz]
16	0	1	15.5	16	16	1	0	15.5	16	535599.921(80)	-0.027
16	0	1	15.5	15	16	1	0	15.5	15	535603.507(70)	-0.030
17	0	1	16.5	17	17	-1	0	16.5	17	540212.658(90)	-0.019
17	0	1	16.5	16	17	-1	0	16.5	16	540217.072(80)	0.067
18	0	1	17.5	18	18	1	0	17.5	18	544659.467(100)	0.013
25	0	1	25.5	26	25	-1	0	24.5	25	569212.491(60)	-0.049
25	0	1	25.5	25	25	-1	0	24.5	24	569216.541(60)	0.082
26	1	0	25.5	26	24	0	1	24.5	25	571024.568(30)	0.000

C

Experimental Data: Carbon Monoxide Ion

The experimental data on all isotopomers of the carbon monoxide ion ana-
lyzed in an isotopically invariant fit are summarized in the following tables.
Two transitions have been recorded with SuJeSTA. Lines taken from the
work of Bogey *et al.* [23], Sastry *et al.* [22], Klapper [10], and van de Heuvel
et al. [105] are marked with a, b, c, and d, respectively.

All transition frequencies and the values for observed minus calculated
are given in *MHz*. For each measured transition the estimated experimental
error, written in brackets, is in units of the least significant digits.

C.1 $^{12}C^{16}O^+$

Table C.1: Rotational spectrum of the main isotopomer of the carbon monoxide ion, $^{12}C^{16}O^+$, in the vibrational states $v \leq 4$.

v	N'	J'	N''	J''	Frequency $[MHz]$	o.-c. $[MHz]$
0	1	0.5	0	0.5	117692.337(30)	0.012
0	1	1.5	0	0.5	118101.812(50)a	0.012
0	2	1.5	1	1.5	235380.046(150)b	-0.106
0	2	1.5	1	0.5	235789.641(30)b	0.037
0	2	2.5	1	1.5	236062.553(20)b	-0.019
0	3	2.5	2	1.5	353741.262(100)b	-0.027
0	3	3.5	2	2.5	354014.247(60)b	-0.010
0	4	3.5	3	2.5	471679.252(30)	-0.095
0	4	4.5	3	3.5	471952.343(100)b	0.028
0	5	4.5	4	3.5	589599.239(100)c	-0.008
0	5	5.5	4	4.5	589872.224(100)c	0.009
0	6	5.5	5	4.5	707496.506(100)c	0.043
0	6	6.5	5	5.5	707769.401(100)c	-0.030
0	7	6.5	6	5.5	825366.363(200)c	-0.117
0	7	7.5	6	6.5	825639.665(200)c	0.217
0	8	7.5	7	6.5	943204.603(250)c	-0.193
0	8	8.5	7	7.5	943477.836(100)c	0.072
0	9	8.5	8	7.5	1061005.900(1000)d	-1.019
1	1	0.5	0	0.5	116553.376(80)a	0.094
1	1	1.5	0	0.5	116960.305(80)a	-0.001
1	2	1.5	1	0.5	233509.032(70)a	-0.012
1	2	2.5	1	1.5	233780.342(80)a	-0.051
1	6	6.5	5	5.5	700924.571(150)c	0.059
2	1	0.5	0	0.5	115411.284(80)a	-0.001
2	1	1.5	0	0.5	115814.790(80)a	0.064
2	2	1.5	1	0.5	231221.423(180)a	-0.044
2	2	2.5	1	1.5	231490.470(100)a	0.043
3	1	1.5	0	0.5	114665.212(120)a	0.151
4	1	1.5	0	0.5	113511.230(100)a	-0.080

C.2 $^{13}C^{16}O^+$

Table C.2: Rotational spectrum of the carbon monoxide ion, $^{13}C^{16}O^+$, in the vibrational states $v = 0,\ 1$.

v	N'	J'	F'	N''	J''	F''	Frequency [MHz]	o.-c. [MHz]
0	1	0.5	0	0	0.5	1	112465.938(120)a	-0.038
0	1	0.5	1	0	0.5	1	112695.175(80)a	0.028
0	1	1.5	1	0	0.5	0	112753.480(40)a	0.043
0	1	1.5	2	0	0.5	1	112902.557(40)a	0.086
0	2	1.5	1	1	0.5	0	225444.382(200)a	-0.050
0	2	1.5	2	1	1.5	1	225504.854(70)a	-0.004
0	2	2.5	3	1	1.5	2	225678.183(160)a	-0.003
0	3	2.5	3	2	1.5	2	338251.384(150)c	-0.020
0	3	3.5	3	2	2.5	2	338377.484(150)c	0.073
0	3	3.5	4	2	2.5	3	338443.693(150)c	0.005
0	4	3.5	3	3	2.5	2	450937.978(250)c	-0.199
0	4	4.5	4	3	3.5	3	451143.635(250)c	-0.183
0	4	4.5	5	3	3.5	4	451196.212(100)c	-0.008
0	5	4.5	4	4	3.5	3	563672.549(100)c	-0.178
0	5	4.5	5	4	3.5	4	563713.663(100)c	-0.010
0	5	5.5	5	4	4.5	4	563890.319(100)c	-0.024
0	5	5.5	6	4	4.5	5	563931.766(250)c	-0.191
0	6	5.5	5	5	4.5	4	676387.165(200)c	0.097
0	6	5.5	6	5	4.5	5	676420.085(100)c	0.017
0	6	6.5	6	5	5.5	5	676613.565(100)c	0.068
0	7	6.5	6	6	5.5	5	789076.889(200)c	0.136
0	7	6.5	7	6	5.5	6	789103.863(200)c	0.245
0	7	7.5	8	6	6.5	7	789336.965(200)c	0.086
0	8	7.5	7	7	6.5	6	901737.536(100)c	-0.021
0	8	8.5	8	7	7.5	7	901975.512(100)c	-0.088
1	1	1.5	1	0	0.5	0	111687.554(70)a	-0.148
1	1	1.5	2	0	0.5	1	111835.716(100)a	0.006
1	2	2.5	3	1	1.5	2	223545.426(80)a	0.014

C.3 $^{12}C^{18}O^+$

Table C.3: Rotational spectrum of the carbon monoxide ion,
$^{12}C^{18}O^+$, in the vibrational states $v = 0,\ 1$.

v	N'	J'	N''	J''	Frequency $[MHz]$	o.-c. $[MHz]$
0	1	1.5	0	0.5	112478.502(400)a	0.082
0	1	0.5	0	0.5	112088.491(40)a	0.001
0	2	1.5	1	1.5	224172.862(180)a	0.002
0	2	1.5	1	0.5	224562.753(60)a	−0.036
0	2	2.5	1	1.5	224822.772(90)a	0.030
1	1	1.5	0	0.5	111417.700(60)a	−0.061
1	2	1.5	1	0.5	222443.650(140)a	−0.053
1	2	2.5	1	1.5	222702.180(70)a	0.011

C.4 $^{13}C^{18}O^+$

Table C.4: Rotational spectrum of the carbon monoxide ion,
$^{13}C^{18}O^+$, in the ground vibrational state.

v	N'	J'	F'	N''	J''	F''	Frequency $[MHz]$	o.-c. $[MHz]$
0	1	0.5	1	0	0.5	1	107081.520(80)a	0.051
0	1	1.5	1	0	0.5	0	107137.965(60)a	0.006
0	1	1.5	2	0	0.5	1	107278.209(60)a	0.078

Bibliography

[1] G. Winnewisser, A. F. Krupnov, M. Y. Tretyakov, M. Liedtke, F. Lewen, A. H. Saleck, R. Schieder, A. P. Shkaev, and S. V. Volokhov. Precision broadband Spectroscopy in the Terahertz Region. Journal of Molecular Spectroscopy, 165:294–300, May 1994.

[2] M. Caris, F. Lewen, and G. Winnewisser. Pure Rotational Spectroscopy of Sodium Chloride, *NaCl*, up to 930 *GHz*. Zeitschrift Naturforschung, 57a:663–668, 2002.

[3] P. L. Clouser and W. Gordy. Millimeter-Wave Molecular-Beam Spectroscopy: Alkali Chlorides. Physical Review, 134:863–870, May 1964.

[4] P. Thaddeus, C. A. Gottlieb, A. Hjalmarson, L. E. B. Johansson, W. M. Irvine, P. Friberg, and R. A. Linke. Astronomical identification of the C_3H radical. The Astrophysical Journal Letters, 294:L49–L53, July 1985.

[5] B. E. Turner, E. Herbst, and R. Terzieva. The Physics and Chemistry of Small Translucent Molecular Clouds. XIII. The Basic Hydrocarbon Chemistry. The Astrophysical Journal Supplement Series, 126:427–460, February 2000.

[6] N. Kaifu, M. Ohishi, K. Kawaguchi, S. Saito, S. Yamamoto, T. Miyaji, K. Miyazawa, S. Ishikawa, C. Noumaru, S. Harasawa, M. Okuda, and H. Suzuki. A 8.8–50GHz Complete Spectral Line Survey toward TMC-1 I. Survey Data. Publications of the Astronomical Society of Japan, 56:69–173, February 2004.

[7] C. A. Gottlieb, J. M. Vrtilek, E. W. Gottlieb, P. Thaddeus, and A. Hjalmarson. Laboratory detection of the C_3H radical. The Astrophysical Journal Letters, 294:L55–L58, July 1985.

[8] C. A. Gottlieb, E. W. Gottlieb, P. Thaddeus, and J. M. Vrtilek. The rotational spectrum of the C_3H radical. The Astrophysical Journal, 303:446–450, April 1986.

[9] S. Yamamoto, S. Saito, H. Suzuki, S. Deguchi, N. Kaifu, S. Ishikawa, and M. Ohishi. Laboratory microwave spectroscopy of the linear C_3H and C_3D radicals and related astronomical observation. The Astrophysical Journal, 348:363–369, January 1990.

[10] G. Klapper. PhD thesis: Präzisionsmessungen des reinen Rotations-spektrums von CO, CO^+ und ihren Isotopomeren. GCA-Verlag, 2000.

[11] H. Störzer, J. Stutzki, and A. Sternberg. CO^+ in the Orion Bar, M17 and S140 star-forming regions. Astronomy and Astrophysics, 296:L9–L12, April 1995.

[12] N. R. Erickson, R. L. Snell, R. B. Loren, L. Mundy, and R. L. Plambeck. Detection of interstellar CO^+ toward OMC-1. The Astrophysical Journal Letters, 245:L83–L86, April 1981.

[13] H. S. P. Müller, F. Schlöder, J. Stutzki, and G. Winnewisser. The Cologne Database for Molecular Spectroscopy, CDMS: a useful tool for astronomers and spectroscopists. Journal of Molecular Structure, 742:215–227, 2005.

[14] J. Cernicharo and M. Guelin. Metals in IRC+10216 - Detection of $NaCl$, $AlCl$, and KCl, and tentative detection of AlF. Astronomy and Astrophysics, 183:L10–L12, September 1987.

[15] E. Lellouch, G. Paubert, J. I. Moses, N. M. Schneider, and D. F. Strobel. Volcanically emitted sodium chloride as a source for Io's neutral clouds and plasma torus. Nature, 421:45–47, January 2003.

[16] R. S. Ram, M. Dulick, B. Guo, K.-Q. Zhang, and P. F. Bernath. Fourier Transform Infrared Emission Spectroscopy of $NaCl$ and KCl. Journal of Molecular Spectroscopy, 183:360–373, June 1997.

[17] M. Kanada, S. Yamamoto, S. Saito, and Y. Osamura. Molecular structure of the linear C_3H radical: Microwave spectrum of the ^{13}C substituted species. The Journal of Chemical Physics, 104:2192–2201, February 1996.

[18] H. Ding, T. Pino, F. Güthe, and J. P. Maier. Gas phase electronic spectrum of C_3H in the visible. The Journal of Chemical Physics, 115:6913–6919, October 2001.

[19] J. Takahashi and K. Yamashita. Ab initio studies on the interstellar molecules C_3H_2 and C_3H and the mechanism for the neutral-neutral reaction $C(^3P) + C_2H_2$. Journal of Chemical Physics, 104:6613–6627, May 1996.

[20] F. Pauzat, Y. Ellinger, and A. D. McLean. Is interstellar detection of higher members of the linear radicals C_nCH and C_nN feasible? The Astrophysical Journal Letters, 369:L13–L16, March 1991.

[21] M. Perić, M. Mladenović, K. Tomić, and C. M. Marian. Ab initio study of the vibronic and spin-orbit structure in the $X^2\Pi$ electronic state of *CCCH*. Journal of Chemical Physics, 118:4444–4451, March 2003.

[22] K. V. L. N. Sastry, P. Helminger, E. Herbst, and F. C. de Lucia. Laboratory millimeter and submillimeter spectra of CO^+. The Astrophysical Journal Letters, 250:L91+, November 1981.

[23] M. Bogey, C. Demuynck, and J. L. Destombes. Equilibrium structure of CO^+ from its millimeter wave spectrum - Breakdown of the Born-Oppenheimer approximation. Journal of Chemical Physics, 79:4704–4707, November 1983.

[24] C. Endres. Diploma thesis: Aufbau eines Multiplier-Terahertzspektrometers und seine Anwendung in der hochauflösenden Laborspektroskopie. 2004.

[25] S. Brünken. PhD thesis: High Resolution Terahertz Spectroscopy on Small Molecules of Astrophysical Importance. Cuvillier Verlag Göttingen, 2005.

[26] M. Caris. Diploma thesis: Rotationsspektroskopie von Natriumchlorid im Bereich von 200 bis 930 GHz. 2001.

[27] A. G. W. Cameron. Abundances of the Elements in the Solar System. Space Science Reviews, 15:121–146, September 1973.

[28] L. M. Ziurys and B. E. Turner. Detection of interstellar vibrationally excited *HCN*. The Astrophysical Journal Letters, 300:L19–L23, January 1986.

[29] C. Kahane, J. Gomez-Gonzalez, J. Cernicharo, and M. Guelin. Carbon, nitrogen, sulfur and silicon isotopic ratios in the envelope of IRC+10216. Astronomy and Astrophysics, 190:167–177, January 1988.

[30] S. Thorwirth, H. S. P. Müller, and G. Winnewisser. Millimetre- and submillimetre-wave spectroscopy of ^{13}C and ^{15}N isotopomers of cyanoacetylene, *HCCCN*, in the ground and vibrationally excited states. Physical Chemistry Chemical Physics, 3:1236–1241, January 2001.

[31] G. Winnewisser and C. M. Walmsley. The detection of HC_5N and HC_7N in IRC+10216. Astronomy and Astrophysics, 70:L37–L39, December 1978.

[32] M. Guélin and P. Thaddeus. Tentative Detection of the C_3N Radical. The Astrophysical Journal Letters, 212:L81–L85, March 1977.

[33] M. Guélin, S. Green, and P. Thaddeus. Detection of the C_4H radical toward IRC+10216. The Astrophysical Journal Letters, 224:L27–L30, August 1978.

[34] S. Yamamoto, S. Saito, M. Guelin, J. Cernicharo, H. Suzuki, and M. Ohishi. Laboratory microwave spectroscopy of the vibrational satellites for the ν_7 and $2\nu_7$ states of C_4H and their astronomical identification. The Astrophysical Journal Letters, 323:L149–L153, December 1987.

[35] M. Guélin, J. Cernicharo, S. Navarro, D. R. Woodward, C. A. Gottlieb, and P. Thaddeus. New doublets in IRC+10216 - Vibrationally excited C_4H? Astronomy and Astrophysics, 182:L37–L39, August 1987.

[36] D. L. Cooper. Ab initio spin-orbit coupling constants for potential exotic interstellar molecules. The Astrophysical Journal, 265:808–812, February 1983.

[37] S. Green. Theoretical microwave spectral constants for C_2N, C_2N^+, and C_3H. The Astrophysical Journal, 240:962–967, September 1980.

[38] W. B. Latter, C. K. Walker, and P. R. Maloney. Detection of the Carbon Monoxide Ion (CO^+) in the Interstellar Medium and a Planetary Nebula. The Astrophysical Journal Letters, 419:L97–L100, December 1993.

[39] T. A. Dixon and R. C. Woods. Microwave absorption spectrum of the CO^+ ion. Physical Review Letters, 34:61–63, January 1975.

[40] N. D. Piltch, P. G. Szanto, T. G. Anderson, C. S. Gudeman, T. A. Dixon, and R. C. Woods. The microwave spectrum of isotopically substituted CO^+ ion. Journal of Chemical Physics, 76:3385–3388, April 1982.

[41] H. S. P. Müller, S. Thorwirth, D. A. Roth, and G. Winnewisser. The Cologne Database for Molecular Spectroscopy, CDMS. Astronomy and Astrophysics, 370:L49–L52, April 2001.

[42] J. R. Birch, J. D. Dromey, and J. Lesurf. The optical constants of some common low-loss polymers between 4 and 40 cm^{-1}. Infrared Physics, 21:225–228, February 1981.

[43] J. R. Birch and F. P. Kong. An interferometer for the determination of the temperature variation of the complex refraction spectra of reasonably transparent solids at near-millimetre wavelengths. Infrared Physics, 23:309–314, 1984.

[44] R. W. Haas and P. W. Zimmerman. 22-GHz measurements of dielectric constants and loss tangents of castable dielectrics at room and cryogenic temperatures. IEEE Trans. Microwave Theory Tech., 24:882–883, November 1976.

[45] J. W. Flemming and G. W. Chantry. Accurate radiometric measurements on low-loss polymers at submillimetric wavelength. IEEE Trans. Instrum. Meas., 23:473–478, December 1974.

[46] G. W. Fuchs. Diploma thesis: Charakterisierung einer Kohlenstoff-Cluster-Quelle. 1999.

[47] G. Scoles. Atomic and Molecular Beam Methods, Vol. 1. Oxford University Press, 1988.

[48] T. J. Balle and W. H. Flygare. Fabry-Perot cavity pulsed Fourier transform microwave spectrometer with a pulsed nozzle particle source. Review of Scientific Instruments, 52:33–45, January 1981.

[49] G. W. Fuchs. PhD thesis: Carbon Chain Molecules, Production and Spectroscopic Detection. Cuvillier Verlag Göttingen, 2003.

[50] R. Schlachta, G. Lask, S. H. Tsay, and V. E. Bondybey. Pulsed discharge source of supersonically cooled transient species. Journal of Chemical Physics, 155:267, 1991.

[51] T. Motylewski and H. Linnartz. Cavity ring down spectroscopy on radicals in a supersonic slit nozzle discharge. Review of Scientific Instruments, 70:1305–1312, February 1999.

[52] D. Herriott, H. Kogelnik, and R. Kompfner. Off-axis paths in spherical mirror interferometers. Applied Optics, 3:523–526, April 1964.

[53] T. F. Giesen. PhD thesis: Druckverschiebung und -verbreiterung an H_2O-Infrarot-Übergängen. 1992.

[54] J. Heseler. Virginia Diodes, private communication. July 2005.

[55] J. W. Gewartowski and H. A. Watson. Principles of Electron Tubes. Van Nostrand, Princeton, N.J., 1965.

[56] R. Kompfner and N. T. Williams. Backward-Wave Tubes. Proc. IRE, 41:1602–1611, November 1953.

[57] H. Heffner. Analysis of the Backward-Wave Traveling-Wave Tubes. Proc. IRE, 42:930–937, June 1954.

[58] H. R. Johnson. Backward-Wave Oscillator. Proc. IRE, 43:684–697, June 1955.

[59] R. Scheuerer, M. Haeussler, K. F. Renk, E. Schomburg, Y. I. Koschurinov, D. G. Pavelev, N. Maleev, V. Ustinov, and A. Zhukov. Frequency multiplication of microwave radiation by propagating space-charge domains in a semiconductor superlattice. Applied Physics Letters, 82:2826–2828, April 2003.

[60] A. Wacker and A.-P. Jauho. Quantum Transport: The Link between Standard Approaches in Superlattices. Physical Review Letters, 80:369–372, January 1998.

[61] R. Tsu and G. Döhler. Hopping conduction in a "superlattice". Physical Review B, 12:680–686, July 1975.

[62] R. F. Kazarino and R. A. Suris. Electric and electromagnetic properties of semiconductors with a superlattice. Soviet Physics Semiconductors, 6:120, 1972.

[63] J. L. Dunham. The Wentzel-Brillouin-Kramers Method of Solving the Wave Equation. Physical Review, 41:713–720, September 1932.

[64] J. L. Dunham. The Energy Levels of a Rotating Vibrator. Physical Review, 41:721–731, September 1932.

[65] G. Herzberg. Molecular Spectra and Molecular Structure I: Spectra of Diatomic Molecules. Van Nostrand, Princeton, N.J., 1950.

[66] G. Herzberg. Molecular Spectra and Molecular Structure II: Infrared and Raman Spectra of Polyatomic Molecules. Van Nostrand, Princeton, N.J., 1945.

[67] C.H. Townes and A.L. Schawlow. Microwave Spectroscopy. Dover Publications, New York, 1975.

[68] W. Gordy and R.L. Cook. Microwave Molecular Spectra. Wiley and Sons, New York, 1975.

[69] P. F. Bernath. Spectra of Atoms and Molecules. Oxford University Press, 1950.

[70] M. Born and R. Oppenheimer. Annalen der Physik, 84:457, 1927.

[71] A.H. Saleck. PhD thesis: Hyperfeinstruktur in Rotationsspektren linearer Radikale und asymmetrischer Kreisel. Hundt Druck GmbH, 1993.

[72] F. Hund. Zur Deutung einiger Erscheinungen in den Molekülspektren. Zeitschrift für Physik, 36:657–674, 1926.

[73] N. E. Holden. Handbook of Chemistry and Physics, 82nd Ed. CRC Press, Boca Raton FL, 2001.

[74] G. Audi and A. H. Wapstra. The 1995 update to the atomic mass evaluation. Nuclear Physics A, 595:409–480, February 1995.

[75] K. J. R. Rosman and P. D. P. Taylor. Isotopic Compositions of the Elements 1997. Journal of Physical and Chemical Reference Data, 27:1275–1287, November 1998.

[76] R. D. Vocke. (for IUPAC Commission on Atomic Weights and Isotopic Abundances). Pure Applied Chemistry, 71:1593–1607, 1999.

[77] J. S. Coursey and R. A. Dragoset. Atomic Weights and Isotopic Compositions (version 2.1). National Institute of Standards and Technology, http://physics.nist.gov/Compositions, 2001.

[78] R. A. Frosch and H. M. Foley. Magnetic Hyperfine Structure in Diatomic Molecules. Physical Review, 88:1337–1349, December 1952.

[79] T. C. Steimle, D. R. Woodward, and J. M. Brown. The lambda-doubling spectrum of ^{13}CH, studied by microwave optical double resonance. Journal of Chemical Physics, 85:1276–1282, August 1986.

[80] G. Pöschl and E. Teller. Bemerkungen zur Quantenmechanik des anharmonischen Oszillators. Zeitschrift für Physik, 83:143, June 1933.

[81] R. Renner. Zeitschrift für Physik, 92:172, 1934.

[82] G. Herzberg. Molecular Spectra and Molecular Structure III: Electronic Spectra and Electronic Structure of Polyatomic Molecules. Van Nostrand, Princeton, N.J., 1966.

[83] J. A. Pople. The Renner Effect anti Spin-Orbit Coupling. Molecular Physics, 3:16–22, 1960.

[84] J. T. Hougen. Rotational Energy Levels of a Linear Triatomic Molecule in a $^2\Pi$ Electronic State. Journal of Chemical Physics, 36:519–534, January 1962.

[85] A. H. Nielsen. The Vibration-Rotation Energies of the Linear X-Y-Z Type Molecule. Journal of Chemical Physics, 11:160–163, April 1943.

[86] H. M. Pickett. The fitting and prediction of vibration-rotation spectra with spin interactions. Journal of Molecular Spectroscopy, 148:371–377, August 1991.

[87] M. Caris, F. Lewen, H. S. P. Müller, and G. Winnewisser. Pure rotational spectroscopy of potassium chloride, *KCl*, up to 930 *GHz* and isotopically invariant analysis of *KCl* and *NaCl*. Journal of Molecular Structure, 695-696:863–870, 2004.

[88] E. F. Pearson and W. Gordy. Millimeter- and Submillimeter-Wave Spectra and Molecular Constants of *LiF* and *LiCl*. Physical Review, 177:52–58, January 1969.

[89] D. R. Lide, P. Cahill, and L. P. Gold. Journal of Chemical Physics, 40:156, 1964.

[90] R. W. Wilson, P. M. Solomon, A. A. Penzias, and K. B. Jefferts. Millimeter Observations of *CO*, *CN*, and *CS* Emission from IRC+10216. The Astrophysical Journal Letters, 169:L35–L37, October 1971.

[91] B. E. Turner. Vibrationally excited *CS* in IRC+10216. Astronomy and Astrophysics, 182:L15–L18, August 1987.

[92] B. E. Turner. Vibrationally Excited CS and SiS in IRC+10216. In Interstellar Matter, page 223, 1988.

[93] P. Schilke, C. Comito, and S. Thorwirth. First Detection of Vibrationally Excited *HNC* in Space. The Astrophysical Journal Letters, 582:L101–L104, January 2003.

[94] F. Wyrowski, P. Schilke, S. Thorwirth, K. M. Menten, and G. Winnewisser. Physical Conditions in the Proto-Planetary Nebula CRL 618 Derived from Observations of Vibrationally Excited HC_3N. The Astrophysical Journal, 586:344–355, March 2003.

[95] J. R. Pardo, J. R. Cernicharo, J. R. Goicoechea, M. Guélin, and T. G. Phillips. The millimeter and submillimeter spectrum of CRL618. In The Dusty and Molecular Universe: A Prelude to Herschel and ALMA, pages 455–456, January 2005.

[96] S. Chandra and Rashmi. Einstein A-coefficients for rotational transitions in the ground vibrational state of $^{28}SiC_2$, $^{29}SiC_2$ and $^{30}SiC_2$. Astronomy and Astrophysics Supplement, 131:137–139, July 1998.

[97] E. Herbst, H. H. Lee, D. A. Howe, and T. J. Millar. The Effect of Rapid Neutral-Neutral Reactions on Chemical Models of Dense Interstellar Clouds. Monthly Notices Radio Astronomers Society, 268:335–344, May 1994.

[98] J. Takahashi. Ab Initio Calculations for Detectable New Isomers of Interstellar Carbon-Chain Radicals C_nH ($n = 2 - 8$). Publication of the Astronomical Society of Japan, 52:401–407, June 2000.

[99] P. Neubauer-Guenther, T. F. Giesen, U. Berndt, G. Fuchs, and G. Winnewisser. The Cologne Carbon Cluster Experiment: Ro-Vibrational spectroscopy on small carbon clusters. Spectrochimica Acta Part A, 59:431–441, 2003.

[100] W. D. Langer and T. E. Graedel. Ion-molecule chemistry of dense interstellar clouds - Nitrogen-, oxygen-, and carbon-bearing molecule abundances and isotopic ratios. The Astrophysical Journal Supplement Series, 69:241–269, February 1989.

[101] L. M. Hobbs. Interferometric Studies of Interstellar CH^+ Molecules. Bulletin of the American Astronomical Society, 4:307, June 1972.

[102] L. M. Hobbs. Interstellar *Na I*, *K I*, *CA II*, and CH^+ Line Profiles Toward Zeta Ophiuchi. The Astrophysical Journal Letters, 180:L79–L82, March 1973.

[103] P. J. Huggins, T. G. Phillips, G. Neugebauer, M. W. Werner, P. G. Wannier, and D. Ennis. Detection of the $J = 3 - 2$ Lines of *HCN*, *HNC* and HCO^+ in the Orion Molecular Cloud. Bulletin of the American Astronomical Society, 9:576, September 1977.

[104] P. Thaddeus, M. Guélin, and R. A. Linke. Three new 'nonterrestrial' molecules. The Astrophysical Journal Letters, 246:L41–L45, May 1981.

[105] F. C. van den Heuvel and A. Dymanus. Observation of far-infrared transitions of HCO^+, CO^+ and HN_2^+. Chemical Physics Letters, 92:219–222, October 1982.

Danksagung

An dieser Stelle möchte ich allen Personen danken, die mich bei dieser Arbeit in vielfältiger Weise unterstützt und zu ihrem Gelingen beigetragen haben:

Ganz besonderer Dank gilt Herrn Priv. Doz. Dr. Thomas Giesen, der die Betreuung dieser Arbeit übernommen hat. Er schuf ein sehr angenehmes Arbeitsklima und stand mir stets mit seinem fachlichen Rat zur Seite.

Ich danke Herrn Prof. Dr. Jürgen Stutzki für seine Bereitschaft, diese Arbeit zu begutachten, und Herrn Prof. Dr. Axel Klein für die Übernahme des Vorsitzes in der Disputationsprüfung.

Ein großer Dank gebührt Dr. Frank Lewen, dessen Wissen über alle Einzelheiten, die zum Betrieb eines Spektrometers erforderlich sind, von unschätzbarem Wert für den Aufbau von SuJeSTA war. Außerdem kennt Frank jede Schraube, an der man drehen kann, um die beste Performance "heraus zu kitzeln".

Herrn Prof. Dr. Stephan Schlemmer danke ich für die fachlichen Diskussionen über eine Vielzahl von physikalischen Fragestellungen.

Herrn Prof. Dr. Gisbert Winnewisser möchte ich für sein Interesse an meiner Arbeit danken.

Ein herzlicher Dank geht an Dr. Holger S. P. Müller für seine Hilfe bei den Fits dieser Arbeit. Sein Wissen, jenseits der *dokumentierten* Funktionalität des SPFIT-Prgramms, war für mich von großem Wert. Außerdem bin ich Ihm für viele Anregungen im täglichen Messbetrieb dankbar.

Den Mitarbeitern der Mechanikwerkstatt gilt für die sorgfältige Anfertigung zahlreicher Bauelemente von SuJeSTA mein besonderer Dank.

Der Besatzung von Zimmer 316 danke ich ganz herzlich für die tatkräftige Unterstützung in allen Phasen dieser Arbeit und das Ertragen meiner Wortwitze. Für den regen Austausch von "Nervennahrung", das Teekochen (auch wenn ich immer noch lieber Kaffee trinke) und das Korrekturlesen meiner Arbeit möchte ich mich ganz besonders bei Petra Neubauer-Guenther bedanken. Das morgendliche Frühstück und den regen Gedankenaustausch mit Gundolf Schmidt werde ich ebenso wie das ausgeglichene Ying und Yang von

Holger Spahn sehr vermissen. Jörg Stodolka sei Dank für die Absenkung der durchschnittlichen Körpergröße in Raum 316.

Oliver Baum und Christian Endres danke ich für ihre Hilfe beim Schleppen und Befüllen der Detektoren. Sandra Brünken möchte ich für ihre vielen guten Ideen und für die heißen Badminton-Matches danken.

Ein ganz besonderer Dank geht an die gesamte Spektroskopiker Gruppe, die ein tolles Arbeiten ermöglicht hat, jedoch noch an ihrem Timing für die gemeinsamen Mittagspausen arbeiten sollte.

Ein herzlicher Dank gilt Gabriele Klapper deren Einführung in die Mysterien der Spektroskopie und ins I. Physikalische Institut für mich von großer Bedeutung war. In diesem Zusammenhang danke ich auch den Geschwistern Weber, die ein großes Stück zu dem eingeschlagenen Weg beigetragen haben.

Meiner gesamten Familie gilt ein riesiger Dank für ihre Unterstützung – insbesondere Marlene, Dieter und Rosemarie.

Dagmar, vielen Dank für Alles!

Erklärung

Ich versichere, dass ich die von mir vorgelegte Dissertation selbstständig angefertigt, die benutzten Quellen und Hilfsmittel vollständig angegeben und die Stellen der Arbeit - einschließlich Tabellen, Karten und Abbildungen-, die anderen Werken im Wortlaut oder dem Sinn nach entnommen sind, in jedem Einzelfall als Entlehnung kenntlich gemacht habe; dass diese Dissertation noch keiner anderen Fakultät oder Universität zur Prüfung vorgelegen hat; dass sie - abgesehen von unten angegebenen Teilpublikationen - noch nicht veröffentlicht worden ist sowie, dass ich eine solche Veröffentlichung vor Abschluß des Promotionsverfahrens nicht vornehmen werde.

Die Bestimmungen dieser Promotionsordnung sind mir bekannt. Die von mir vorgelegte Dissertation ist von Herrn Privatdozent Dr. T. F. Giesen betreut worden.

Teilpublikationen

- "Pure rotational spectroscopy of potassium chloride, *KCl*, up to 930 *GHz* and isotopically invariant analysis of *KCl* and *NaCl*.", M. Caris, F. Lewen, H. S. P. Müller, and G. Winnewisser, J. Mol. Struc., 695-696:863-870, 2004.

- "High Resolution *THz* spectroscopy of the *C$_3$H* radical up 600 *GHz*.", M. Caris, C. Duan, F. Lewen, H. S. P. Müller, and T. F. Giesen, in prep., 2005.

Lebenslauf

Michael Caris

Geburtsdatum	22. Oktober 1970
Geburtsort	Porz am Rhein (Köln)
Saatsangehörigkeit	deutsch
Wohnort	Idastr. 39
	51069 Köln

Schulausbildung

1977–1979	Städt. Gemeinschaftsgrundschule	Köln
1979–1981	Katholoische Grundschule	Lülsdorf
1981–1990	Heinrich-Heine-Gymnasium	Köln

Zivildienst

1990–1991	Johanniter Unfallhilfe	Köln

Hochschulstudium

10.1991–04.1994	Grundstudium der Physik	Universität zu Köln
04.1994	Vordiplom in Physik	
04.1994–06.1999	Hauptstudium der Physik	
07.1999–12.2000	Miniforschung am I. Physikal. Institut	
01.2001–01.2002	Diplomarbeit am I. Physikal. Institut	
01.2002	Diplom in Physik	
02.2002	Beginn des Promotionsstudiums	

Berufserfahrung

09.1999–04.2001	Systembetreuer bei der Döres AG	Köln